Mechanics and Control of Human Balance

by

Matthew Millard

A thesis
presented to the University of Waterloo
in fulfillment of the
thesis requirement for the degree of
Doctor of Philosophy
in
Systems Design Engineering

Waterloo, Ontario, Canada, 2011

I hereby declare that I am the sole author of this thesis. This is a true copy of the thesis, including any required final revisions, as accepted by my examiners.

I understand that my thesis may be made electronically available to the public.

Abstract

A predictive, forward-dynamic model and computer simulation of human gait has important medical and research applications. Most human simulation work has focused on inverse dynamics studies to quantify bone on bone forces and muscle loads. Inverse dynamics is not predictive - it works backwards from experimentally measured motions in an effort to find the forces that caused the motion. In contrast, forward dynamics determines how a mechanism will move without the need for experimentation. Most of the forward dynamic gait simulations reported consider only one step, foot contact is not modeled, and balance controllers are not used. This thesis addresses a few of the shortcomings of current human gait simulations by contributing an experimentally validated foot contact model, a model-based stance controller, and an experimentally validated model of the relationship between foot placement location and balance.

The goal of a predictive human gait simulation is to determine how a human would walk under a condition of interest, such as walking across a slippery floor, using a new lower limb prosthesis, or with reduced leg strength. To achieve this goal, often many different gaits are simulated and the one that is the most human-like is chosen as the prediction for how a person would move. Thus it is necessary to quantify how 'human-like' a candidate gait is. Human walking is very efficient, and so, the metabolic efficiency of the candidate gait is most often used to measure the performance of a candidate gait. Muscles consume metabolic energy as a function of the tension they develop and the rate at which they are contracting. Muscle tension is developed, and contractions are made in an effort generate torques about joints in order to make them move. To predict human gait, it is necessary for the simulation to be able to walk in such a way that the simulated leg joints use similar joint torques and kinematics as a human leg does, all while balancing the body. The joint torques that the legs must develop to propel the body forward, and balance it, are heavily influenced by the ground reaction forces developed between the simulated foot and the ground. A predictive gait simulation must be able to control the model so that it can walk, and remain balanced while generating ground reaction force profiles that are similar to experimentally observed human ground reaction force profiles.

Ground reaction forces are shaped by the way the foot interacts with the ground, making it very important to model the human foot accurately. Most continuous foot contact models present in the literature have been experimentally validated using pendulum impact

methods that have since been shown to produce inaccurate results. The planar foot contact model developed as part of this research was validated *in-vivo* using conventional force plates and optical tracking markers. The experimental data was also highly useful for developing a computationally efficient foot model by identifying the dominant contact properties of a real foot (during walking), without the complexity of modelling the 26 bones, 33 joints, over 90 ligaments, and the network of muscles that are in a real foot.

Both ground reaction forces and the balance of the model are heavily influenced by the way the stance limb is controlled. Anthropomorphic multibody models typically have a fragile sense of balance, and ground reaction force profiles that do not look similar to experimentally measured human ground reaction force profiles. In contrast, the simple point-mass spring-loaded-inverted-pendulum (SLIP) can be made to walk or run in a balanced manner with center-of-mass (COM) kinematics and ground reaction force profiles that could be mistaken for the equivalent human data. A stance limb controller is proposed that uses a planar SLIP to compute a reference trajectory for a planar anthropomorphic multibody gait model. The torso of the anthropomorphic model is made to track the computed trajectory of the SLIP using a control system. The aim of this partitioned approach to gait simulation is to endow the anthropomorphic model with the human-like gait of the simpler SLIP model.

Although the SLIP model-based stance-controller allows an anthropomorphic gait model to walk in more human-like manner, it also inherits the short comings of the SLIP model. The SLIP can walk or run like a human, but only at a fixed velocity. It cannot initiate or terminate gait. Fall preventing movements, such as gait termination and compensatory stepping, are of particular relevance to kinesiologists and health care professionals. Kinesiologists have known for nearly a decade that humans restore their balance primarily by systematically altering their foot placement location. This thesis presents a human experimental validation of a planar foot placement algorithm that was originally designed to restore the balance of bipedal robots. A three-dimensional (3D) theoretical extension to the planar foot placement algorithm is also presented along with preliminary human experimental results. These models of foot placement can be used in the future to improve the capabilities of gait simulations by giving simple models human-like compensatory stepping abilities. The theoretical extension also provides some insight into how instability and balance performance can be quantified. The instability and balance performance measures have important applications for diagnosing and rehabilitating balance problems.

Despite all of the progress that has been made, there is still much work to be done. Work needs to be continued to find methods that allow the anthropomorphic model to emulate the SLIP model more faithfully. Experimental work needs to be completed to realize the potential diagnostic and rehabilitation applications of the foot placement models. With continued effort, a predictive, balanced, multi-step gait simulation can be developed that will give researchers the time-saving capability of computerized hypothesis testing, and medical professionals improved diagnostic and rehabilitation methods.

Acknowledgements

This thesis represents the culmination of my unexpected degree. Originally I intended to complete a Master's degree, but quickly realized that I would not have enough time to accomplish what I wanted. My supervisors John McPhee and Eric Kubica invited me to transfer into the PhD program. Nearly 5 years later I can now confirm that a PhD is also too short a time to accomplish what I hoped to do. While the experiences of my PhD degree have been typical, filled with successes, failures, and long hours, the people around me have been exceptional. I owe a great debt of gratitude to my advisors Professor John McPhee and Dr. Eric Kubica. John's technical depth in multibody dynamics and contact modelling are very rare, as are his excellent editing skills, which have been very useful during the research that this thesis deals with. Eric's very unique biomechanics and control background, coupled with his excellent critical thinking skills and patience have shaped the path of my degree and the trajectory of the career that will follow.

During this multidisciplinary degree I have worked with many different students from engineering and the applied health sciences. There are too many good stories to write about in this short text. Much of the work in this thesis was inspired by Mike Peasgood's masters work, and conversations that we had when I began my degree. The work on foot contact modelling was greatly aided by Michael MacLellan and Heather Edgell's experimental assistance, and conversations with Sukhpreet Sandhu. Derek Wight developed the first planar foot placement theory, and after many animated discussions, we collaborated on the human foot placement experiments. Michael MacLellan, Jeremy Noble and Heather Lillico greatly aided the experimental portion of the planar foot placement work. The theoretical portion of the 3D foot placement research developed quickly after an insight from Willem Petersen who looked at one of my sketches and said 'that looks a lot like an Euler disc'. The experimental portion of the work would not have been possible without the help of Janice Moreside. Professor Paul Calamai provided very helpful advice on validating numerical partial derivatives used in the sensitivity analysis for both the planar and spatial foot placement studies. The nonlinear control work done in both the 3D foot placement, and final planar gait model was greatly aided by insightful advice from Professor David Wang. I owe a great debt of gratitude to Dr. Chad Schmitke, who wrote and supported the symbolic multibody dynamics package DynaFlexPro, which has given me insight and fast simulations in nearly every project presented in this thesis. Finally, I am grateful to the

University of Waterloo's Kinesiology Department for giving me access to their laboratories for the experimental work presented in this thesis.

There is a large community of people that have surrounded me during my degree that may not have directly contributed on specific research projects, but have been just as important to my development as a person. Throughout my entire degree, my fellow research group members Willem Petersen, Tom Uchida, Sukhpreet Sandhu and Chandrika Prakash have provided valuable technical advice, timely jokes and friendship. Across the campus in applied health sciences, my friends Janice Moreside, Jenny Jackson and Erika Nelson-Wong have given me insight, support and encouragement as I made my way into the unfamiliar territory of kinesiology. Looey Tremblay, Pat Gilles and Jen Kozak have been a close friends for many years and taught me how to dance, which has been a constant source of ideas, fun, and a reliable form of stress relief. Linda Carson and Parthipan Siva have given me unparalleled friendship, good conversation and much needed enthusiasm. Michelle Hur, my parents Brian and Jennifer, and my sister Sarah, have been an unwavering source of moral and emotional support during the intensely busy experience that has been my PhD. I must acknowledge my grandmother Elizabeth Beamish and my Great Aunt Kay, whose injuries and conversations inspired me to investigate human balance many years ago by enrolling in Professor Aftab Patla's course on human walking. Aftab's enthusiasm and exceptional teaching inspired me to pursue the topic further in graduate school.

Financially this research was made possible by funding from the Ontario Graduate Scholarship, the Natural Sciences and Engineering Research Council of Canada (NSERC) Alexander Graham Bell Scholarship, the University of Waterloo's President's Scholarship and Professor John McPhee's NSERC Discovery grant. I would also like to acknowledge Springer and the ASME Journal of Biomechanical Engineering for granting me permission to reproduce material in Ch. 3 and 4 [65], and Ch. 6 [66], that I previously published with them.

Dedication

To my grandmother Elizabeth Beamish, my Great Aunt Kay, and my parents Brian and Jennifer for their inspiration and support

Table of Contents

List of Tables

List of Figures

Nomenclature

Ch. 3 Motivating Work: Predicting Human Gait using Joint Trajectories

HAT Lumped head, arms and trunk segment

f_n Contact force normal to the surface (N)

f_f Friction force tangential to the surface (N)

k Contact material stiffness (N/m)

p Contact material nonlinearity coefficient

y Penetration depth (m)

c Contact material damping ($\frac{Ns}{m}$)

μ, μ_s, μ_d Coefficient of friction, static friction and dynamic friction

v_s, v_d Tangential stiction and dynamic friction velocities (m/s)

$\theta_j(t)$ Joint trajectory j, where j ($j = 1, 2, 3$) designates the hip, knee or ankle joint (rad)

A_k, B_k Fourier coefficient

λ Walking period

Δ Grid size in the pattern search

Ch. 4 Volumetric Foot Contact Model

IREDs Optotrak infrared diodes

$\vec{f_n}$ Volumetric contact force vector (N)

k Volumetric material stiffness ($\frac{N}{m^3}$)

V Volume of interpenetration (m^3)

a Normalized volumetric material damping ($\frac{s}{m}$)

v_N Normal contact velocity ($\frac{m}{s}$)

$\hat{\mathbf{n}}$ Volumetric normal direction unit vector

τ_T Rolling resistance vector (Nm)

$\vec{\omega}_T$ Tangential angular velocity vector ($\frac{rad}{s}$)

$[J_c]$ Second moment of the contact area (m^5)

Ch. 5 Predicting Human Gait using Simple Models and Torso Trajectories

SLIP Spring Loaded Inverted Pendulum

ASLIP Asymmetric Spring Loaded Inverted Pendulum

LASLIP Legged Asymmetric Spring Loaded Inverted Pendulum

x_S,x_A,x_L,x_M Horizontal position of the SLIP, ASLIP, LASLIP and multibody torso COM $(\frac{m}{s^2})$

y_S,y_A,y_L,y_M Vertical position of the SLIP, ASLIP, LASLIP, and multibody torso COM $(\frac{m}{s^2})$

θ_A,θ_L,θ_M Angular orientation of the ASLIP, LASLIP, and multibody torso (rad)

α_A,α_L,α_M Hip joint angle of the ASLIP, LASLIP, and multibody models (rad)

β_L,β_M Knee joint angle of the LASLIP, and multibody model (rad)

γ_M Ankle joint angle of the multibody model (rad)

ϕ_L Angle of the LASLIP ankle joint (rad)

ϕ_S,ϕ_A Angle the SLIP and ASLIP swing limb is held at relative to the stance limb during single stance (rad)

f_{Sx},f_{Ax},f_{Lx},f_{Mx} The net horizontal force applied to the SLIP, ASLIP,LASLIP and multibody torso (N)

f_{Sy},f_{Ay},f_{Ly},f_{My} The net vertical force applied to the SLIP, ASLIP,LASLIP and multibody torso (N)

τ_A,τ_L,τ_M Hip torque applied to the torso of the ASLIP, LASLIP, and multibody models (Nm)

p_S,p_A Ground reaction force component parallel with the leg of the SLIP and ASLIP (N)

q_A Ground reaction force component normal with the leg of the ASLIP (N)

m Mass of the torso SLIP, ASLIP, LASLIP and multibody torso (kg)

J Sagittal plane moment of inertia of the ASLIP, LASLIP and multibody torso taken about the COM of the torso($kg\,m^2$)

g Force of gravity ($9.81\frac{m}{s^2}$)

(cx_S, cy_S),$cx_A, cy_A)$,$cx_L, cy_L)$ Foot contact location of the SLIP, ASLIP and LASLIP models (m, m)

r Length of the legs of the SLIP (m)

k Stiffness of the spring legs of the SLIP model $(\frac{N}{m})$

l Length of the leg(s) of the ASLIP (m)

L Distance between the hip joint and torso COM (m)

L_1 Length of the LASLIP thigh (m)

L_2 Length of the LASLIP shank (m)

L_{12} Length of the knee-locked LASLIP leg (m)

Ay Height of the ankle joint of the LASLIP model(m)

Hx Length of the heel of the LASLIP model (m)

Tx Length of the forefoot of the LASLIP model (m)

ν_θ Desired angular acceleration of the torso of the ASLIP, LASLIP and multibody models $(\frac{rad}{s^2})$

K_θ Penalty term for torso orientation error $(\frac{1}{s^2})$

D_θ Penalty term for torso angular velocity error $(\frac{1}{s})$

UtS LASLIP leg posture with one toe in contact with the ground

UtUh LASLIP leg posture with one toe and one heel in contact with the ground

UtF LASLIP leg posture with one foot flat on the ground and the other with a toe touching the ground

FS LASLIP leg posture with one foot flat on the ground

FUh LASLIP leg posture with one foot flat on the ground and the other touching the ground at the heel

ν_x Desired horizontal acceleration of the torso of the multibody models $(\frac{m}{s^2})$

K_x Penalty term for the torso horizontal position error $(\frac{1}{s^2})$

D_x Penalty term for the torso horizontal velocity error $(\frac{1}{s})$

ν_y Desired vertical acceleration of the torso of the multibody models $(\frac{m}{s^2})$

K_y Penalty term for the torso vertical position error $(\frac{1}{s^2})$

D_y Penalty term for the torso vertical velocity error $(\frac{1}{s})$

γ^i_{SS} Joint angles of the single stance control model (rad)

τ^i_{SS} Joint torques of the single stance control model leg (Nm)

τ_{SW} The hip torque that the swing limb applies to the pelvis of the single stance control model (Nm)

$\vec{F}_{SW}$ The force that the swing limb applies to the pelvis of the single stance control model (N)

γ^i_{DS} Joint angles of the double stance control model (rad)

τ^i_{DS} Joint torques of the double stance control model (Nm)

F^i_{DS} The force vector that the each leg of the double stance model applies to the hip joint (N, N)

ψ^i_{SW} Joint angles of the swing control model (rad)

τ^i_{SW} Joint torques of the swing control model (Nm)

(Ax, Ay) The vector between the COM and the ankle of the rigid foot used in the single and double stance control models (m, m)

(Cx, Cy) The vector between the COM and the revolute joint (which represents the COP) used in the single and double stance control models (m, m)

x_{COP} The location of the revolute joint (which represents the COP) of the stance control models (m)

$\dot{x}_{COP}$ The translational velocity of the revolute joint (which represents the COP) of the stance control models (m)

$[M_{SS}]$,$[M_{DS}]$, $[M_{SW}]$ The mass matrix of the single stance, double stance, and swing control models

$\vec{C}_{SS}$,$\vec{C}_{DS}$, $\vec{C}_{SW}$ The vector of Coriolis, centripetal and gravitational forces applied to the single stance, double stance and swing models

$[P_{SS}]$,$[P_{DS}]$,$[P_{SW}]$ The matrix that transforms applied joint torques into generalized forces for the single stance, double stance and swing control models

$[Q_{SS}]$ The matrix that transforms the hip force and torque the swing limb applies to the pelvis into generalized forces

$[T_{SS}]$ The matrix that maps joint angular accelerations into $\ddot{x}$,$\ddot{y}$, and $\ddot{\theta}$ of the torso COM

$\vec{D_{DS}}$ The vector of position constraints, applied at the two hips, in the double stance control model

$[B_{SS}]$ The matrix that transforms the Lagrange multipliers (of the hip joint constraints) into reaction forces

$\vec{\lambda}$ The vector of Lagrange multipliers associated with the hip joint constraint equations used in the double stance control model

$\vec{F}^{i}_{DS}$ The force vector that is applied at hip i of the multibody model (N, N)

Ch. 6 Discrete Planar Balance Corrections using Foot Placement

FPE Foot placement estimator

HFP Human foot placement location

FPE-HFP Error Distance between the FPE and the HFP

MT Distal 5^{th} metatarsal head

C Fibular trochlea of the calcaneus

LM Lateral malleolus

FH Proximal fibular head

GT Greater trochanter

AP Acromion process

ϵ_{LM} Horizontal distance between the FPE and LM during contact onset (cm)

ϵ_{MT} Horizontal distance between the FPE and MT (when foot is flat) during contact onset (cm)

μ Average

σ Standard deviation

ρ Correlation coefficient

g The acceleration due to gravity (9.81 m/s^2)

h COM height (m)

h_{peak} Peak height the COM can reach with 1 foot on the ground (m)

Ho_1 Angular momentum about contact point o, prior to contact ($kg\ m^2/s$)

Ho_2 Angular momentum about contact point o, after contact ($kg\ m^2/s$)

H_{LMGP} Angular momentum about the ground projection of the LM ($kg\ m^2/s$)

J_{com} Moment of inertia about the COM ($kg\ m^2$)

J_i Inertia of the i^{th} segment ($kg\ m^2$)

m Mass (kg)

m_i Mass of the i^{th} segment (kg)

L Leg length (m)

$\vec{r}_i$ Vector to the COM of the i^{th} segment (m)

$\vec{r}_{COM}$ Vector to the entire body's COM (m)

$\vec{r}_{LM}$ Vector to the LM (m)

$\vec{r}_{LMGP}$ Vector to the LM ground projection (m)

T Kinetic energy of the body (J)

$T + V$ System energy (J)

t_C Time of contact onset (s)

V Potential energy of the body (J)

$\vec{v}(t)_i$ Linear velocity of the COM of the i^{th} segment (m/s)

v_x X component of the pre-contact COM velocity (m/s)

v_y Y component of the pre-contact COM velocity (m/s)

$X(\phi)$ The location of the FPE on the floor (m)

ϕ Angle between the vertical and the lead leg (rad)

$s\phi$ $sin(\phi)$

$c\phi$ $cos(\phi)$

$\frac{\partial X(\phi)}{\partial H_{LMGP}}$ Rate of change of $X(\phi)$ w.r.t H_{LMGP} $(m/[kg\ m^2/s])$

$\frac{\partial X(\phi)}{\partial J_{COM}}$ Rate of change of $X(\phi)$ w.r.t J_{COM} $(m/[kg\ m^2])$

$\frac{\partial X(\phi)}{\partial L}$ Rate of change of $X(\phi)$ w.r.t L (m/m)

$\frac{\partial X(\phi)}{\partial (T+L)}$ Rate of change of $X(\phi)$ w.r.t $T + L$ (m/J)

$\vec{\omega}_i$ Angular velocity of the i^{th} segment about its COM (rad/s)

$\dot{\theta}_1$ Angular speed of the body before contact (rad/s)

$\dot{\theta}_2$ Angular speed of the body after contact (rad/s)

Ch. 7 Discrete Spatial Balance Corrections using Foot Placement

3DFPE Three dimensional Foot Placement Estimator

Euler Pendulum

p The point of contact between the contact ring and the ground

q The center of mass of the Euler pendulum

$\hat{\mathbf{1}}$ $\hat{\mathbf{2}}$ $\hat{\mathbf{3}}$ The local coordinate frame of the Euler pendulum. Note that the Euler pendulum can spin relative to this local axis in the $\hat{\mathbf{1}}$ direction

$\hat{\mathbf{z}}$ The vertical unit direction vector

$\hat{\mathbf{r}}$ The horizontal unit vector created by crossing the $\hat{\mathbf{2}}$ and $\hat{\mathbf{z}}$ axes

$\vec{\omega}_{123}$ The angular velocity of the $\hat{\mathbf{1}}$ $\hat{\mathbf{2}}$ $\hat{\mathbf{3}}$ frame $(\frac{rad}{s})$

ω_{rel} The angular velocity of the Euler pendulum about the $\hat{\mathbf{1}}$ axis in the inertial frame $(\frac{rad}{s})$

m The mass of the Euler pendulum (kg)

$[J]$ The inertia matrix of the Euler pendulum $(kg\,m^2)$

J_1,J_2 The entries of the main diagonal of the Euler pendulum inertia matrix $(kg\,m^2)$

c The height of the Euler pendulum (m)

a The diameter of the base of the Euler pendulum (m)

β The rotation of the Euler pendulum relative to the $\hat{\mathbf{1}}$ $\hat{\mathbf{2}}$ $\hat{\mathbf{3}}$ frame (rad)

α The rotation of the Euler pendulum about the $\hat{\mathbf{2}}$ axis (rad)

θ The rotation of the $\hat{\mathbf{1}}$ $\hat{\mathbf{2}}$ $\hat{\mathbf{3}}$ frame about the $\hat{\mathbf{z}}$ axis (rad)

$\vec{L}_q$ The angular momentum

$\vec{\tau}_R$ The rolling resistance torque between the contact ring and the ground (Nm)

$\vec{\tau}_F$ The spin friction torque between the contact ring and the ground (Nm)

$\vec{F}$ The reaction force vector at the point of contact p (N, N, N)

$\mathcal{L}_\beta$ The rolling resistance terms that affect $\ddot{\beta}$ $(\frac{rad}{s^2})$

$\mathcal{L}_\alpha$ The rolling resistance terms that affect $\ddot{\alpha}$ $(\frac{rad}{s^2})$

$\mathcal{L}_\theta$ The rolling resistance terms that affect $\ddot{\theta}$ $(\frac{rad}{s^2})$

$\vec{r}_{q/p}$ The vector from point p, the contact point, to point q, the center of mass of the Euler pendulum (m, m, m)

$\vec{r}_{p/q}$ The vector from point q, the center-of-mass, to point p, the contact point of the Euler pendulum (m, m, m)

$\vec{H}p_0$,$\vec{H}p_1$, $\vec{H}p_2$ The angular momentum of the Euler pendulum about point p a finite time before contact, the instant prior to contact, and the instant following contact while rocking ($\frac{kg\,m^2}{s}$)

$\vec{\omega}_0$,$\vec{\omega}_1$,$\vec{\omega}_2$ The angular velocity of the Euler pendulum about point p a finite time before contact, the instant prior to contact, and the instant following contact while rocking ($\frac{rad}{s}$)

U,U_0,U_1,U_2 The potential energy of the Euler pendulum while spinning; while rocking and a finite time prior to contact, the instant before contact, and the instant after contact (J)

T,T_0,T_1,T_2 The potential energy of the Euler pendulum while spinning; while rocking and a finite time prior to contact, the instant before contact, and the instant after contact (J)

V,V_0,V_1,V_2 The potential energy of the Euler pendulum while spinning; while rocking and a finite time prior to contact, the instant before contact, and the instant after contact (J)

$\vec{v}_{cm}$ The velocity of the center-of-mass, point q, of the Euler pendulum ($\frac{m}{s}$)

R The magnitude of the rolling resistance torque (Nm)

κ The coefficient of rolling resistance ($m\,s^2$)

$\hat{\boldsymbol{\omega}}_T$ The unit vector that is aligned with the angular velocity of the pendulum tangent to the surface

S The magnitude of the spin friction torque (Nm)

μ_S The coefficient of spinning friction ($m\,s$)

$\hat{\boldsymbol{\omega}}_N$ The unit vector that is aligned with the angular velocity of the pendulum normal to the surface

h_{peak} The peak height of the center of mass of the pendulum with the contact ring still touching the ground (m)

$\vec{F_C}$ The average contact force during a rocking contact (N, N, N)

Δt The impulse duration during a rocking contact (s)

μ_L The coefficient of translational friction

Modeling Foot Placement

$\vec{H}_{GP}$ The angular momentum of the inverted pendulum taken about the center-of-mass ground-projection location ($\frac{kg\,m}{s}$)

$\hat{\mathbf{u}}$ The horizontal unit vector that is perpendicular to the horizontal components of the angular momentum vector

ϵ The fraction of the angular momentum vector that is perpendicular to $\hat{\mathbf{u}}$ (%)

$\vec{r}$ The vector from the center of mass to the point of contact ((m, m, m))

ϕ The FPE angle the leg must be held at (relative to the vertical) at contact to catch the balance of the pendulum (rad)

h The height of the center of mass above the ground plane (m)

$\vec{v}_1^{||}$ The component of the translational velocity of the center-of-mass of the pendulum projected into a vertical plane with unit vectors $\hat{\mathbf{u}}$ and $\hat{\mathbf{k}}$ ($\frac{m}{s}$)

$\vec{v}_{1xy}^{||}$ The horizontal velocity component of $\vec{v}_1^{||}$ ($\frac{m}{s}$)

$\vec{v}_{1z}^{||}$ The vertical velocity component of $\vec{v}_1^{||}$ ($\frac{m}{s}$)

$\omega_1^{\perp}$ The angular velocity of the inverted pendulum that is perpendicular to both $\hat{\mathbf{u}}$ and $\hat{\mathbf{k}}$ ($\frac{rad}{s}$)

$L_{FPE}(\phi)$ The coordinates of the 3DFPE on the floor relative to the center-of-mass ground projection location (m, m, m)

L_{CAP} The coordinates of the capture point on the floor relative to the center-of-mass ground projection location (m, m, m)

k_{CAP} The stiffness of the spring used in Pratt's [82] equivalent linear inverted pendulum model (N/m)

$f_{0,CAP}$ The pre-load placed on the spring used in Pratt's [82] equivalent linear inverted pendulum (N)

Experimental Methodology

$D_{FPE,H}$ The horizontal Euclidean distance between the 3DFPE location and the subject's heel at contact onset (m)

$D_{CAP,H}$ The horizontal Euclidean distance between the CAP location and the subject's heel at contact onset (m)

$\vec{r}_C OM$ The vector to the center-of-mass of the subject (m, m, m)

$\vec{r}_C OP$ The vector to the center-of-pressure of the subject (m, m, m)

$\vec{r}_s$ The vector from the subject's center-of-pressure to the center-of-mass (m, m, m)

$\vec{F}_{GRF}$ The ground reaction force vector measured by the force plate under the subject's foot (N, N, N)

k The observed stiffness of the subject's leg $(\frac{N}{m})$

$\frac{\partial L_{FPE}(\phi)}{\partial L}$ The rate change of the 3DFPE location w.r.t. changes in leg length $(\frac{m}{m})$

$\frac{\partial L_{FPE}(\phi)}{\partial J_{COM}}$ The rate change of the 3DFPE location w.r.t. changes in moment of inertia $(\frac{m}{kg\,m^2})$

$\frac{\partial L_{FPE}(\phi)}{\partial (T+V)}$ The rate change of the 3DFPE location w.r.t. changes in system energy $(\frac{m}{J})$

$\frac{\partial L_{FPE}(\phi)}{\partial (\vec{H}_p \cdot (\hat{\boldsymbol{\imath}} + \hat{\boldsymbol{\jmath}}))}$ The rate change of the 3DFPE location w.r.t. changes in horizontal angular momentum $(\frac{m}{kg\,m^2/s})$

ΔL The maximum change in leg length from contact onset between the center-of-mass passed over the center-of-pressure (m)

ΔJ_{COM} The maximum change in moment-of-inertia from contact onset between the center-of-mass passed over the center-of-pressure $(\frac{kg\,m^2}{s})$

$\Delta(T+V)$ The maximum change in system energy from contact onset between the center-of-mass passed over the center-of-pressure (J)

$\Delta(\vec{H}_p \cdot (\hat{\boldsymbol{\imath}} + \hat{\boldsymbol{\jmath}}))$ The change in the horizontal component of angular momentum from contact onset until 50 ms [66] after contact $(\frac{kg\,m^2}{s})$

A_L The estimated 3DFPE error caused by varying leg length (m)

$A_{J_{COM}}$ The estimated 3DFPE error caused by a varying moment-of-inertia (m)

A_{T+V} The estimated 3DFPE error caused by a varying system energy (m)

A_{Hp} The estimated 3DFPE error caused by changes of momentum at contact (m)

A_{MSE} The total 3DFPE error measure of A_L,$A_{J_{COM}}$,A_{T+V}, and A_{Hp} assuming each error is independent (m)

E_{ORB} The orbital energy of the biped during stance, a quantity the capture point algorithm assumes is constant ($\frac{m^2}{s^2}$)

A_{ORB} The percentage change in orbital energy from contact to mid-stance (%)

Chapter 1

Introduction

A computer model and simulation system capable of predicting the kinetics and kinematics of human locomotion would be a useful tool in the many disciplines concerned with assessing and improving the way people walk and balance. The quality of the solution from such a system is intimately linked to the fidelity of the model, the access the control system gives the model to the human motion space, and the definition that is used to measure how human-like a particular gait is. Each of these problem facets are only partially understood; each contain active areas of research. While it is generally accepted that it is reasonable to use idealized joints to approximate the hips, knees and ankles of a gait model, there is no accepted way to model the foot-ground contact, nor an accepted way to validate the foot contact model. The freedom of movement the control system gives to the model is related to the means that are used to plan and manipulate the motion of the model. If a purely optimization-based approach is used [5, 1, 2] then the access the model has to the human motion space is limited by the tendency of the optimization routine to become trapped by local minimum. If a control system is used to balance the biped [64], the access it has to the human motion space is related to how easily the control system can be manipulated to make functionally-relevant changes in the gait of the model. The ability of a computer simulation to access the human motion space is typically not mentioned, nor quantified in the literature. Finally, the kinds of solutions found by the system are heavily influenced by the definition used to measure how human-like a particular gait is. Although gaits which consume a minimum of metabolic energy are often defined as being human-like [5, 1, 65], this definition is incomplete. It has been experimentally shown that

humans select step-length and step-frequency combinations that coincide with metabolic minima [113]. It has not been shown that humans choose muscle activation patterns that consume a minimum of metabolic energy. Electromyographic (EMG) recordings of muscle activity during walking [109] actually show that humans do not choose metabolically minimal muscle activation patterns due to the presence of co-contraction of agonist and antagonist muscle pairs. Despite the EMG evidence, cost functions that favour metabolically minimal muscle activation patterns are commonly used to quantify how human-like a particular gait is [1, 2, 65, 4]. It is clear that the field of human gait simulation is fraught with imperfect models, partial access to the human motion space, and incomplete measures for how human-like a particular motion is.

The means used to find a human-like movements affect how useful the research is outside of the computer. While optimization-based approaches [5, 2] and heuristic methods [97] are sufficient to make a computer model walk in a human-like way, these methods do not yield insight into how a human accomplishes this motion. Instead, if the model is used to aid in the development and assessment of candidate locomotor control systems, it may eventually be possible to not only simulate human locomotion in a computer, but also to understand how humans control their gait in real life.

Computer models have been used to aid in the formulation and assessment of human-like control systems of the upper limb for over twenty years. Beginning in the mid 1980s a productive cycle of theoretical and experimental research began on the control of the upper limb, enabled by haptic robots [40]. These haptic robots allowed researchers to apply force fields to the human arm in motion [69], to observe and quantify motor learning, and also to validate or refute their own mathematical models of upper limb control [89]. Bhushan and Shadmehr's planar upper limb motor control model [6] represents the current state of the art which is quite sophisticated, taking into account muscle dynamics and signal delays that are characteristic of the human body. Bhushan and Shadmehr's model and control system was able to exhibit similar learning behaviour and transient responses (when the force field created by the haptic robot changed) as human subjects. These advanced models of motor control have been judiciously used to develop robotic rehabilitation programs for stroke victims that are at least as effective, and in some cases more effective [58], at upper limb control rehabilitation than a therapist.

The study of human balance has not enjoyed the same productive cycle of theoretical and experimental research. This cycle of research has not yet begun because haptic ma-

chines capable of applying a force field to the lower limb and torso during walking are still quite novel [88, 77] making it very challenging to systematically validate or refute mathematical formulations for balance control. Correspondingly, diagnosing balance maladies, and rehabilitating a patient's balance after it has been damaged, are both very difficult. Diagnosing balance problems is challenging because there is not yet an accepted way of measuring how unstable a biped is, nor how effectively the biped restores its balance. While there are rigorous mathematical definitions of balance used by the robotics and dynamic walking community, balance cannot currently be assessed in a general manner because these methods assume small perturbations (such as shifting a back pack) that do not disturb the periodic motion of walking [15]. Humans, in contrast, are often subjected to large perturbations (such as tripping), and catch their balance using a single, well-placed, aperiodic, compensatory step. The rehabilitation of human walking is also limited. Current approaches consist of supporting a patient's body weight using a suspension system while trained physiotherapists guide their legs through walking motions . Understandably this therapy is both physically demanding on the physiotherapists and expensive for the patients. Robotic therapy machines [45] designed to guide the patient's legs through a normal kinematic walking pattern do not appear to be as effective as similar therapy delivered by a physiotherapist [43, 106]. A recent advancement in rehabilitation technology [77] takes a different approach. Instead of forcing the subject's legs through a walking motion, the machine catches the subject if they fall and applies support or perturbations to the subject's torso as they move. Although this new approach looks promising, it has not yet been experimentally established if this new therapy is superior to previous attempts. It is my hope that improvements in the simulation of human gait will lead to improvements in balance diagnosis and balance rehabilitation.

1.1 Motivating Work: Predicting Human Gait using Joint Trajectories

The first gait model and control system presented in Ch. 3 of this thesis controls the periodic trajectory of the leg joints, then regulates the orientation of the torso to allow the model to walk multiple steps without falling over. Although this model is one of the very few humanoid models in the literature that can walk many steps without falling

[65, 97, 112, 76, 25, 96], the formulation is not flexible enough to allow the trajectories of the legs to be adjusted without causing the model to fall. In addition, the kinematics and kinetics of this model compare poorly with experimental human data. The poor ground reaction force profiles of this model inspired further work into foot contact modeling, and the control of the stance phase in Chs. 4 and 5. The fragile sense of balance of this model led to the work on foot placement and balance in Chs. 6 and 7.

1.2 Volumetric Foot Contact Model

To have a model that can walk like a human, it is necessary to accurately model the foot because the foot heavily influences the kinetics of the model. The foot contact model affects how the ground reaction force profile develops, which in turn affects joint torques, and thus the metabolic energy consumption of the model. Interestingly, although there are many different foot models in the literature, none have been validated *in-vivo* in a convincing manner. Chapter 4 presents an analytical foot pad, and two-segment foot model formulated using a lumped parameter volumetric contact model. Tangential forces are modeled using a Coulomb friction model. A novel *in vivo* method was used to validate both the foot pad and foot contact models.

1.3 Predicting Human Gait using Simple Models and Torso Trajectories

The poor performance of the foot contact model used in Ch. 3 is only partially responsible for the un-human ground reaction force profiles that the simulation predicted. Ground reaction force profiles are created and shaped by not just the foot, but the way in which the entire leg is controlled during the stance phase. Formulating a stance leg controller that yields human-like ground reaction force profiles is very challenging because there are many gaits that are humanly possible, yet experimental records suggest [109] that we choose to walk in a very specific way. Finding the most likely gait a human would use is often treated as an optimization problem. The most common formulation for predicting human gait involves first deriving the equations of motion for a multibody musculo-skeletal model

of a human, then formulating a cost function that has a minima at a likely solution, and finally solving this problem using an optimization method.

The tractability of any optimization problem depends strongly on the selected optimization variables. While it is understood what optimization variables are most appropriate for some well-studied problems — such as finding fuel optimal flight paths for aircraft — it is not clear what the most appropriate optimization variables are for human gait simulation. Muscle excitations are commonly used as optimization variables for high-fidelity musculo-skeletal models [1]. Although systems that use muscle excitations as optimization variables can find metabolically minimal gaits given a target trajectory, there is evidence that the cost function space has many local minima [2] — two different metabolic minimas were found with very similar joint kinematics — making it challenging to do something as basic as changing the length of a stride, or the path of the torso during stance. In contrast, the optimization variables used for simple point-mass, telescoping leg gait models are the contact angle of the leg, and the linear force generated by the telescoping leg [95]. The choice of optimization variables for the simple model makes it easy for the optimization algorithm to change higher-level variables such as foot contact location and center-of-mass trajectory because it can set these variables directly due to the greatly simplified swing phase a massless leg affords. At the present time, simple models appear to be best suited for finding desirable gross parameters of the stance phase — such as foot placement location and center-of-mass (COM) trajectory — while detailed musculoskeletal models are better suited to finding joint torques and muscle excitation profiles that realize a given trajectory.

The intent of the research presented in Ch. 5 is to develop a control system that will allow the optimization variables to be higher-level variables (such as torso trajectory) rather than low-level variables (such as muscle activations), making it easy for the optimization routine to make functionally relevant kinematic changes to the gait of the model. This will be achieved by partitioning the difficult problem of simulating human walking into two simpler problems. A relatively simple model will be used to find human-like torso COM trajectories. The multibody model will emulate the simple models gait through the use of a control system. This partitioned approach allows the optimization routine to adjust the gait of the simple gait model, and then assess the quality of its solution by simulating the multibody model; ideally avoiding many local minima in the process.

The stance phase will be the main focus of the control system development because it

requires the highest torques — and therefore consumes the most metabolic energy — and is responsible for controlling the state of the torso. The stance limb control system will be developed to ensure that the torso of the multibody model converges to a candidate torso trajectory. Candidate torso trajectories can be generated by any means, however, in this thesis candidate torso trajectories will be generated by a simple spring loaded inverted pendulum (SLIP) model because it is able to emulate human COM trajectory and ground reaction force (GRF) profiles well. Introducing a control system for the stance limb has several practical benefits: balance is guaranteed as long as the stance limb can fully control the state of the torso, and it is relatively easy for an optimization routine to alter the target path of the torso, the most massive body segment.

A series of planar gait models of increasing likeness to the human form will be used in Ch. 5 to develop the input-output feedback linearization control systems [44] that will ultimately allow a multibody gait model to emulate a SLIP model. The first model considered is a bipedal extension of an existing monopedal, articulated SLIP (ASLIP) model [79]. The bipedal ASLIP model is closer to the human form than the SLIP model because it has torso dynamics, though it retains the actuated massless prismatic legs of its predecessor. The second model considered is the articulated leg ASLIP (LASLIP) model, which includes massless articulated legs that have hip, knee and ankle joints. Both the ASLIP and the LASLIP simplified models interact with the ground through an instantaneous revolute joint, have massless legs, and an instantaneous swing phase. The final model considered is an 11 degree-of-freedom (DOF) multibody sagittal plane model that interacts with the ground using a foot comprised of two spherical contacts (one for the heel and another for the forefoot) attached to a foot model that is allowed to flex through the metatarsals.

The stance limb control systems presented in Ch. 5 are conceptually very different from the one employed in Ch. 3. In Ch. 3, and in the vast majority of the literature, the end goal of the control system is periodic leg motion that leads to balanced walking. In Ch. 5 the end goal of the control system is to use the legs to control the state of the torso such that it moves in a human-like manner. By using the legs to control the state of the torso, periodic leg movement ceases to be the goal of the control system, but becomes a side effect of having legs of finite length. It should be noted that the state of the stance leg is not directly controlled in this torso-centric control paradigm, but instead is allowed to evolve throughout the stance phase.

The models used in Ch. 5 are of modest fidelity relative to their upper limb coun-

terparts. Muscle dynamics and transmission delays are ignored, and so, both the control system and joint actuators can respond far faster than their human counterparts. Although bipedal models have been developed that include neuromuscular dynamics, rigorous nonlinear control systems have not yet been developed to allow these models to walk. These higher-fidelity biomechanical models have been made to walk using experimental data to provide a tracking reference [99], powerful optimization methods [5, 1], or heuristic control techniques [97]. While tracking experimental data, using optimization, or heuristic control systems may yield results for a particular simulation, none of these approaches will yield insight into how, or why, a human accomplishes such motions. The model simplifications used in Ch. 5 have been made in an effort to make the task of control system formulation and analysis tractable. The control systems formulated in this chapter do not yet have any clinical application but instead contribute to ongoing efforts to model human gait.

1.4 Sagittal Plane and Spatial Balance Corrections using Foot Placement

In Ch. 5, a control system was used to allow a multibody model to emulate the SLIP, ideally inheriting the human-like gait of the SLIP in the process. Similarly, the multibody model also inherits the limitations of the SLIP model that it is emulating. Although the SLIP can be made to run and walk with human-like COM and GRF profiles, it can only do so at a fixed velocity. While the SLIP model can maintain a very consistent gait, the control it has over its balance is poor because it cannot stop. Gait termination is of particular interest to kinesiologists and clinicians, because humans use these types of movements to prevent falls and ultimately injury. Clearly, the simple model that the multibody model emulates needs to be able to catch its balance like a human.

In this thesis, the concept of balance is explored using two different paradigms: the continuous balance control that the stance limb applies to the torso during ground contact in Ch. 5 and the discrete changes of balance that occur when a swing limb becomes a stance limb in Chs. 6 and 7. This paradigm division is necessary because experimental data suggest that humans modulate both the location of their foot placement on the ground plane [74] and the torques they apply to the hip, knee and ankle joints in response to perturbations [19]. The connection between foot placement location and discrete balance

correction is established theoretically using a Lyapunov stability analysis [44] applied to simplistic planar [108] and spatial models in Chs. 6 and 7, respectively. Following the stability analysis, a method for calculating a foot placement location that can restore balance to the unstable model is presented. The accuracy of the foot placement models, and their assumptions, are examined experimentally using human kinetic and kinematic data. The resultant foot placement algorithms will be useful for simulating human gait and may also be of clinical use to quantify imbalance and balance performance.

Chapter 2

Literature Review

In this chapter we briefly review the literature associated with multi-step human gait simulations, contact modeling of the feet, the discrete balance corrections created by foot placement location, and continuous balance control provided by the stance limb.

2.1 Motivating Work: Predicting Human Gait using Joint Trajectories

Forward-dynamic human gait simulations usually only simulate a single step [5, 24] in an effort to avoid modelling foot contact and formulating balance control systems. The few multi-step forward-dynamic simulations in the literature have used a relatively fixed gait [65, 97, 112, 76, 25, 96]. In contrast, Peasgood *et al*'s [76] forward dynamic simulation is predictive: the simulated gait is altered in an effort to find metabolically efficient or 'human-like' gaits, allowing it to estimate how a person would walk in a new situation — e.g. with a new lower-limb prosthesis.

A computer simulation that is able to reliably predict how a person would walk in a new situation would be extremely useful to many health care professionals and researchers studying human gait. Peasgood et al.'s system finds 'human-like' or metabolically minimal gaits by searching for joint trajectories of the hip, knee and ankle that minimize metabolic cost per distance traveled. The model is not supported or balanced by any

artificial means, and so, poorly chosen trajectories can overwhelm the balance controller, causing the model to fall. Chapter 3 will evaluate and extend Peasgood et al.'s work, and identify the shortcomings of current multi-step forward dynamic gait simulations.

2.2 Volumetric Foot Contact Model

The foot forms an important kinematic and kinetic boundary between the human body and the ground. This is true both in the contexts of real and simulated human walking. If the simulated foot-ground contact is not representative of a human's, then the loads applied to the simulated joints of the leg will also be different. The stance phase of a gait model with an unrealistic foot will never simultaneously achieve human-like stance kinematics and kinetics. The foot contact model used in Ch. 3 is not representative of a human foot, and is partially responsible for the un-human ground reaction profiles generated during Peasgood et al.'s [76], and Millard et al.'s [65], predictive forward-dynamic gait simulations. An accurate model of the foot is a prerequisite for an accurate simulation of human walking.

Modelling the human foot is very challenging. The human foot is comprised of 26 bones that are connected by over 90 flexible ligaments, actuated by a multitude of muscles, and padded on the bottom by a layer of specialized fat to protect the skeleton during foot-ground contact. The foot has been modeled using finite-element (FE) methods [33], and lumped parameter continuous contact models [65, 1, 97, 76, 112]. While FE models are capable of simulating the stress and strain distribution of the foot tissue to a high level of detail, they are computationally intensive to solve. Although lumped parameter models do not simulate the deformation of tissue, and thus can only be viewed as crude approximations, their vastly superior computational efficiency makes them attractive when the foot is not the entire focus of the numerical study.

When modelling the foot, it is important to accurately model the specialized fat tissue that the foot pads are comprised of, as well as the structure and movement of the foot as a whole. Studies to determine the stiffness and damping properties of human foot pads have failed to produce consistent results. Traditionally *in vivo* experimental results disagree by orders of magnitude from *in vitro* experiments. In the past, *in vivo* experiments have measured the tissue compression and load by impacting an instrumented mass into a subject's heel [103, 51]. As long as the skeletal system of the body acts like a perfect

ground, the deceleration of the mass will be entirely due to the compression of the heel pad. Aerts *et al* [3] was able to experimentally demonstrate that this assumption is invalid: a significant amount of energy is lost through the body, skewing the stiffness values reported from *in vivo* pendular experiments to be nearly one-sixth the published *in vitro* values. *In vitro* stiffness and damping estimates obtained using an Instron material testing machine are also suspect because the tissue may not be representative of living foot pad tissue from the general population.

While foot tissue models are often developed and validated in isolation from the multi-body gait model, the same cannot be said for foot contact models [97, 112, 76]. This approach is problematic: if the ground reaction force representation is poor, it is impossible to know if it is due to an error in the foot contact model or due to the way the foot is being used by the assumed control system. The only foot contact model that was tested separately from the gait simulation [28] was validated in a naive way: ankle joint torques and forces estimated from an inverse dynamics analysis were applied to a forward dynamic simulation of the foot model; the fidelity of the foot model was evaluated by comparing the kinematics of the simulated foot to the experimental data. This approach is naive because the quantization and measurement error that is inherent in an experimental inverse dynamics analysis will cause the forward dynamic simulation to diverge from the experimental observations, even if the model is perfect. Chapter 4 will present a lumped parameter tissue model and a novel means of validating the model *in vivo*.

2.3 Predicting Human Gait using Simple Models and Torso Trajectories

Control of the stance leg simultaneously affects how human-like the ground reaction force profiles are, and how well the model balances. The joint-trajectory based stance limb controller used in Ch. 3 endowed Peagood et al.'s [76], and Millard et al.'s [65] gait models with a fragile sense of balance, and created ground reaction force profiles that poorly match human experimental data [109]. An improved stance limb controller is required if the model of Ch. 3 is to simulate human walking accurately.

While much effort has been spent by both the robotics and kinesiology communities to formulate bipedal gait controllers that result in periodic leg movements typical of walking

(as in Ch. 3), relatively little effort has been spent investigating how the hip, knee and ankle joint torques might instead be coordinated during stance to control the state of the torso. The focus on the stability of periodic walking has led to the development of a rigorous theoretical framework for analyzing periodic systems with applied impulses (the impulses occur when the rigid foot models contact the ground), be they robot [32, 105] or human [15]. Many heuristic controllers have also been developed on the assumption that the key feature of walking is the periodicity of the legs [65, 97, 112, 76]. Controllers that regulate the orientation of the torso have been formulated for passive walking machines [63, 111], partial gait models [52], and more recently a sagittal plane walking model [25]. Each of these models has its drawbacks when considered in the context of human walking: the passive walking machines display a lot of torso sway relative to a human [109]; the partial gait model [52] assumes that the hip torque applied to the torso does not change the force vector applied to the hip; and the sagittal plane walking model [25] uses a heuristic controller, which has unknown stability properties and exhibits more torso sway than a human does while walking [109]. None of the human-like bipedal models in the literature have used the legs to do more than regulate the orientation of the torso.

Recently, Poulakakis and Grizzle [79, 80] used input-output feedback linearization to embed desirable torso dynamics into the controller of a simplified planar robot (Fig. 5.1B). Their model, the asymmetric spring loaded inverted pendulum (ASLIP), consists of a planar biped with massless, telescoping legs that attach at the hip joint of the torso. The COM of the torso is not coincident with the hip joint, adding non-trivial torso dynamics to the system equations of the biped. Poulakakis and Grizzle used the hip torque, and leg force (the linear force generated by the telescoping leg) of the model to control the state of the torso. This control was achieved by embedding the dynamics of the desired plant, the spring loaded inverted pendulum (SLIP model) (Fig. 5.1A) into the control laws for the hip torque and leg force using input-output feedback linearization [44].

Interestingly the similarities between human COM kinematics and ground reaction force profiles to those of the SLIP model during both walking and running [26] are unmatched by any other model in the literature. The COM kinematics and ground reaction force profiles can be made to fit simultaneously within ± 1 standard deviation of human profiles [109] if the point contacts of the SLIP model are allowed to translate forward at a velocity that is similar to the center of pressure (COP) velocity in humans [7]. The quality of fit between the SLIP model and human walking and the illustration that this gait can be embedded in

more elaborate models [79, 80] using input-output feedback linearization, compelled me to see if SLIP dynamics could be embedded into a sagittal plane human gait model. The lower dimensional SLIP model COM trajectory is embedded in a series of models of increasing likeness to the human form in Ch. 5.

2.4 Discrete Planar Balance Corrections using Foot Placement

Although the control systems presented in Ch. 5 allowed several models to emulate the human-like gait of the SLIP model, this approach did nothing to improve upon the limitations of the SLIP model. The SLIP model can walk or run in a manner that resembles a human, but only at a fixed pace. The SLIP model cannot initiate, nor terminate gait. Although the SLIP model has been used to study the control and stability properties of a particular gait [92], this model has not shed light on how humans stop. Understanding how balance is controlled during gait termination is of vital importance to kinesiologists and health care professionals because humans use these actions to prevent falls and injury.

Balance control is a multi-faceted process that relies on state estimation, the prediction of a desirable future state, the means to make the transition (through foot-placement, center of pressure manipulation or some other mechanism), and the physical ability to execute the desired action. Foot placement has been identified by some researchers as the primary means that humans use to restore balance [74, 71]. Foot placement is an important component of balance control because the location of the foot determines the origin and possible directions of the ground reaction force vector which ultimately serves to balance the body. Wight et al. [108] developed a relationship between foot placement and balance — the foot placement estimator (FPE) — that calculates a foot contact location that will *restore* balance to a simplified biped that is falling. The aim of the FPE is to restore balance makes it well suited for analyzing human gait, because humans are unbalanced for 80% of the gait cycle [71]. The aim of Ch. 6 is to determine if the FPE can predict sagittal plane human foot placement (HFP) during gait initiation, termination, and continuous walking.

The biomechanics community has investigated foot placement for many years. Lee et al. [56] were one of the first to conclude that foot placement location is carefully controlled

when they observed the astonishingly small takeoff foot placement error (8 cm) of elite long jumpers who were sprinting high speed (9 m/s). Patla extended Lee's research by showing that foot placement is guided by vision [73], modified by the presence of obstacles [72], and contributes to dynamic balance [71] in everyday activities. Redfern et al. [87] characterized foot placement as a function of velocity and vision. Redfern's work has a limited scope of applicability because it is based on heuristics. Townsend et al.[101] developed and tested several foot placement algorithms using a computer simulation of gait. Townsend et al.'s foot placement models were never validated using human experiments, nor were they derived with the aim of restoring balance.

Balance and foot placement are also primary concerns of roboticists. Robotics researchers have explored machine-learning techniques [46, 98], trajectory tracking [112, 76], passive swing dynamics [63, 84, 55], approximate methods [85], and zero-moment point (ZMP) [104] methods to balance bipedal robots. Little can be learned about human balance using machine learning techniques because they are based on numerical approximation and curve fitting [46, 98]. Trajectory tracking bipeds [65, 112, 76] have a very fragile sense of balance, which suggests that humans do not use this method. Passive swing dynamics explain how humans might be choosing step lengths as a function of walking velocity [54, 107] but cannot be applied to gait initiation and termination. The most popular balance definition is the ZMP [104] that is employed in Honda's bipedal robot Asimo [39]. The ZMP is not well-suited for analyzing human gait because it requires that at least one foot remains flat on the floor at all times. Humans rarely have one foot flat on the ground while walking [110]. Chapter 6 will investigate the applicability of Wight et al.'s foot placement estimator (FPE) [108] to human gait. Wight et al.'s FPE is unique because it is accompanied by a stability proof, and does not require that the stance foot be flat on the floor.

2.5 Discrete Spatial Balance Corrections using Foot Placement

The planar FPE presented in Ch. 6 has assumptions that are compatible with mechanics of human walking, and predicts locations that correspond well with experimentally measured human foot placement locations. Humans, in contrast to the FPE, and models presented

in this thesis, walk in 3 dimensions (3D). Before the human-gait simulation partitioned approach detailed in Ch. 5 can be extended to 3D, the planar FPE presented in Ch. 6 needs to be extended to the spatial domain.

Although foot placement has been studied by both roboticists and kinesiologists, there are few methods that have been developed for three-dimensional (3D) systems, accompanied by a stability proof, and compatible with human gait. Few balance control methods have been developed for 3D systems [84, 85, 104] with the vast majority of works applied in the sagittal plane, or in 2 vertical perpendicular planes [62, 53, 83]. While extending a planar foot placement method to 3D by using 2 perpendicular planes is appealing, the approach is flawed for foot placement algorithms that assume energy conservation, since energy is a scalar quantity and cannot be split up into components. Most works assume that perturbations to the gait of the biped are small [65, 15, 112, 76, 84, 55, 85] with few approaches being valid when large perturbations are applied [108, 104, 83]. A stability proof is of great value to show that a method functions and also to clearly communicate the assumptions and limits of the proposed method. The zero-moment-point (ZMP) and linear-inverted pendulum [47] formulations are the only 3D balance theories that do not assume that all perturbations are small, and are accompanied by a stability proof. The ZMP is incompatible with human balance because it assumes that one foot remains flat on the floor at all times yet humans rarely have one foot flat on the ground while walking [109] and are airborne for many common activities like running. The linear inverted pendulum balance theory [47] assumes that the center of mass (COM) of the biped stays at a constant height which is rarely true for human movement. Although Wight et al.'s planar FPE is not the only foot placement algorithm in existence, it is a good starting point for a 3D foot placement method because it is valid for small and large perturbations, is accompanied by a stability proof, and is compatible with human gait [66]. A full 3D theoretical extension to Wight et al.'s planar FPE (3DFPE) is presented in Ch.7 and is accompanied by a preliminary experimental validation.

Chapter 3

Motivating Work: Predicting Human Gait using Joint Trajectories

Peasgood et al.'s system represents the first attempt at developing a predictive, multi-step gait simulation that searches for metabolically efficient gaits. Nearly 1000, 10-step simulations were required to find a metabolically efficient, 'human-like' gait. Originally the 1000 gait simulations took 10 days to perform on a single computer using the popular mechanical modeling package MSC.Adams [68]. DynaFlexPro [60] (or MapleSim as it is now called), another modeling package, developed since Peasgood et al.'s work, offers substantial performance advantages over Adams: the updated version of Peasgood et al.'s predictive system now takes only 8 hours to run. Peasgood et al.'s work was taken, carefully examined, analyzed, improved, and implemented in DynaFlexPro.

3.1 Dynamic Model

Peasgood et al. developed a predictive gait simulation using a 2D, 7 segment, 9 degree of freedom (dof), anthropomorphic model shown in Fig. 3.1 with a continuous foot contact model. This is a fairly standard model topology for gait studies. The upper body is simplified into a single body representing the head, arms and trunk (HAT); the thigh and shank are each one segment, as is the foot [5, 1, 27]. An additional simplification has been made in this model by fusing the HAT to the pelvis. There was an unintended error in

Peasgood et al.'s original model: there was an extra body attached to the foot that had a moment of inertia of 1.5 $kg \cdot m^2$, which is comparable to the HAT segment. The various model and control parameters associated with this implementation can be found in App. A.

A convergence study was performed on both the DynaFlexPro and the corrected Adams gait models by dropping both unactuated models onto the floor from the same initial conditions. The convergence of each model was checked individually. The results from the DynaFlexPro model converged for every simulation listed in Tbl. 3.1, whereas the Adams model failed to converge with an integrator error tolerance of 10^{-5}. The maximum relative error between the Adams and DynaFlexPro result sets is shown in Table 3.1 for the horizontal position of the left hip, the angle of the right ankle and the contact force developed under the right heel. The relative error was computed by taking the largest absolute difference between the two simulations and dividing it by the largest absolute value from the DynaFlexPro result set. Interestingly, the simulations with an integrator error tolerance of 10^{-7} had the smallest relative error, and allowed the DynaFlexPro model

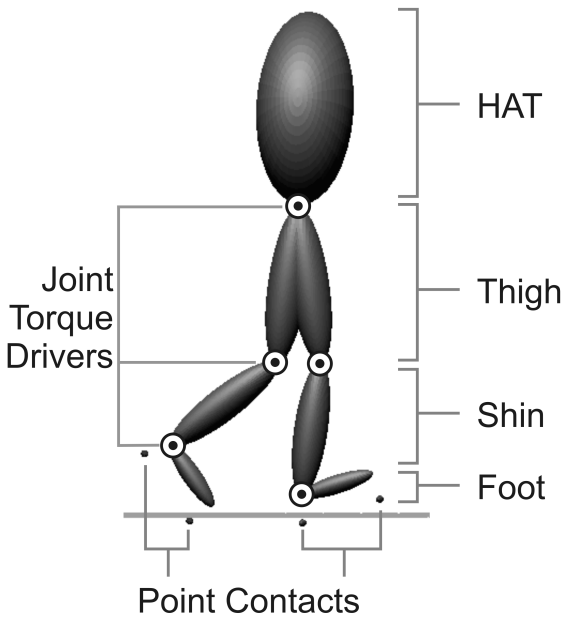

Figure 3.1: Peasgood et al.'s 7 segment, 9 degree of freedom, planar gait model with a 2-point continuous foot contact model

to simulate four times faster than the Adams model as shown in Table 3.1.

Table 3.1: Performance comparison between the Adams and DynaFlexPro 2D 7 segment gait models for a 10 second simulation. The Adams simulation with an integrator error tolerance of 10^{-5} failed to converge. The relative error increases from the hip position to the foot angle: the large mass of the HAT attenuates position error of the hip, while foot position is more sensitive to errors due to its light mass. The high stiffness of the heel contact makes the simulated contact forces very sensitive to errors

	Adams	DynaFlexPro	Maximum Relative Error (%)		
Integrator	GSTIFF (I3)	ode15s (NDF)	Left hip	Right ankle	Right heel
Error Tol.	Simulation Time (s)		disp. (x)	angle	contact force
10^{-5}	29	4.1	3.02	5.65	14.30
10^{-7}	33	7.3	0.09	0.16	0.27
10^{-9}	36	30	0.24	0.48	0.73

3.2 Point Contact Foot Contact

Foot contact forces were calculated using a 2-point foot contact model, with a point contact located at the heel and metatarsal. Normal forces were calculated using the Adams implementation [68] of the continuous Hunt-Crossley [42] point contact model:

$$f_n = -ky^p - c(y)\dot{y} \tag{3.1}$$

The Hunt-Crossley contact model calculates normal force (f_n) as a function of penetration depth (y), penetration rate ($\dot{y}$), material stiffness (k, p), and material damping ($c(y)$). The damping coefficient ($c(y)$) is increased from zero to its maximum value as a function of penetration depth (y) using a cubic spline [68] to prevent an instantaneous normal force that would be created using a simple damping term such as ($c_{max}\dot{y}$) (Fig. 3.2). A dry Coulomb model was used to calculate the force of friction between the points and the plane:

$$f_f = \mu(\dot{x})f_n \tag{3.2}$$

This friction model has stiction (μ_s) and dynamic friction (μ_d) coefficients that are interpolated using a cubic step function [68] between the stiction velocity (v_s) and the sliding velocity (v_d) using the tangential contact velocity ($\dot{x}$) as an input (Fig. 3.2). The particular contact and friction parameters used for the gait simulation were chosen by the pattern search routine (described later) to match the ground reaction forces created during healthy gait [109].

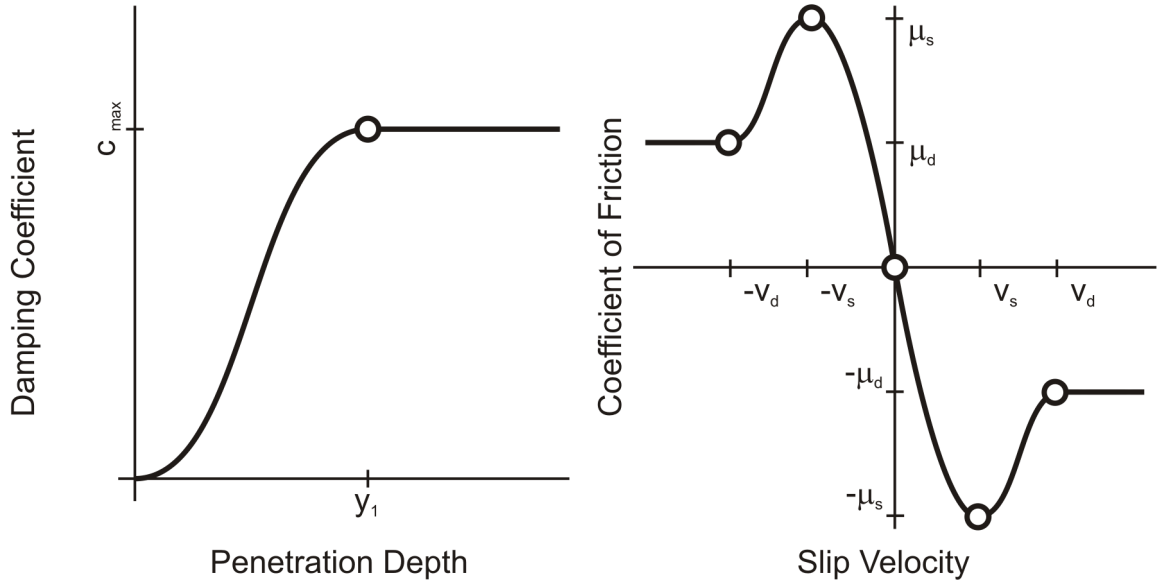

Figure 3.2: Both the coefficient of damping (left panel) and the coefficient of friction (right panel) were interpolated using cubic spline curves

3.3 Joint Trajectory Control

Pre-computed joint trajectories are used to define the nominal gait of the model at the position level. Each joint is actuated using a proportional-derivative (PD) controller that modifies and regulates the predefined joint trajectories. The initial joint trajectories were taken from an existing experimental data set of a healthy gait of an average-sized male [109] and interpolated using a 5-term Fourier series defined by the Fourier coefficients (A_k, B_k, and C_0) and period length (λ). The PD gains were chosen by hand initially to allow the

model to walk. Once this initial gait was established, a pattern search routine was used to find the PD gains that minimized the estimated muscle fatigue [12] of the model.

$$\theta_j(t) = C_0 + \sum_{k=1}^{5} \left[A_k \sin\left(\frac{2\pi kt}{\lambda}\right) + B_k \cos\left(\frac{2\pi kt}{\lambda}\right) \right] \tag{3.3}$$

Some adjustments were made to the trajectories in order to apply them to a sagittal plane gait model: the swing phase of the ankle trajectory had to be altered to prevent the foot from dragging on the ground. This makes sense because the 2D sagittal plane model cannot use hip roll and body sway in the frontal plane to adjust the floor clearance of the swing limb, unlike the subject used in the experiment data set. The interpolated joint trajectories were applied to the PD joint controllers to achieve an initial simulated gait. The optimization routine adjusts the values of the Fourier series coefficients for each limb to search for new gaits. The same Fourier coefficients are used for each limb, offset in phase by π radians, restricting the model to walk with a symmetric periodic gait.

3.4 Balance and Velocity Control

A balanced gait and a desired forward velocity is achieved by manipulating the pitch of the HAT. The pitch controller works by monitoring the orientation of the HAT relative to a desired set angle and speeding up or slowing down the progression of the legs through the joint trajectories to keep the HAT at a desired angle. When the HAT pitches forward (backward) beyond the desired set angle, the legs are driven faster (slower) to walk ahead (behind) of the HAT. The velocity controller is very similar to the pitch controller: when the model is moving too slowly (quickly), the reference angle for the pitch controller is increased (decreased), causing the model to lean forward (backward), making the balance controller force the model to walk faster (slower). A detailed account of the pitch and velocity controllers can be found in Peasgood et al.'s original paper [76]. The pitch and velocity controllers balanced the model, but only over a very narrow range: the model could not initiate gait from a stand still, but had to begin the simulation with carefully selected initial conditions. These initial conditions were used for every simulation.

3.5 Pattern Search Optimization Routine

Peasgood et al. tuned the control system parameters and the joint trajectories using a pattern search optimization routine. The algorithm is conceptually described below. A more formal treatment of the material can be found in Lewis et al. [57].

1. Repeat for all parameters:
   (a) Add amounts $+\Delta$ and - Δ (called the grid size) to one parameter.
   (b) Evaluate the objective function. Save parameter changes that improve the objective function for later use.
2. Update all parameters with the improved values from Step 1 .
3. Evaluate the objective function. If it improves, accept the new parameter set from Step 2; else use the original parameter set.
4. Decrease Δ by half, return to Step 1. Continue until Δ is below a predefined tolerance.

The performance of this algorithm relies on the assumption that a set of individual changes to the joint trajectories will collectively result in an improvement. This assumption is valid if the set of parameters are independent. Peasgood et al.'s assumption of independence does not hold when applied to joint trajectories: a beneficial change to the hip joint trajectory may cause the model to fall when combined with a beneficial change to the knee joint trajectory. Thus this search routine only ever improved the objective function when a set of individual parameter changes was found that just happened to collectively improve the simulated gait.

The pattern search optimization routine was used to find joint trajectories that minimized muscle fatigue [12] cost. Only once in an optimization run that included 717 simulations did all of the individual improvements found by the pattern search routine result in a more efficient gait when used collectively. This one single improvement was able to decrease the metabolic cost of the simulated gait by 21.5%. When I examined the optimization log file it revealed that there were many individual parameter changes that improved the objective function but were ignored. Further investigation showed that a set

of individually beneficial parameter changes caused the model to fall when applied simultaneously. I adjusted the pattern search algorithm to take advantage of good individual parameter changes immediately, resulting in a greedy pattern search routine. A further adjustment was made by allowing the pattern search to continue making adjustments to a single parameter that improved the objective function until the improvements ceased.

3.6 Results

The joint angles for the final simulated gait and a healthy human gait [109] are shown in Fig. 3.3. The standard deviation of the joint angles, torques and ground reaction forces for the current results are negligible, indicating that the gait is very consistent. The joint trajectories of the knee and hip are similar between all three data sets, but the ankle joint trajectories, and torques are quite dissimilar. The log file of the optimization routine revealed that increasing the ankle extension led to a significant reduction in metabolic cost. The adjusted pattern search routine was able to find a gait that resulted in 47.6% less metabolic cost, a 26.1% improvement over Peasgood et al.'s original approach.

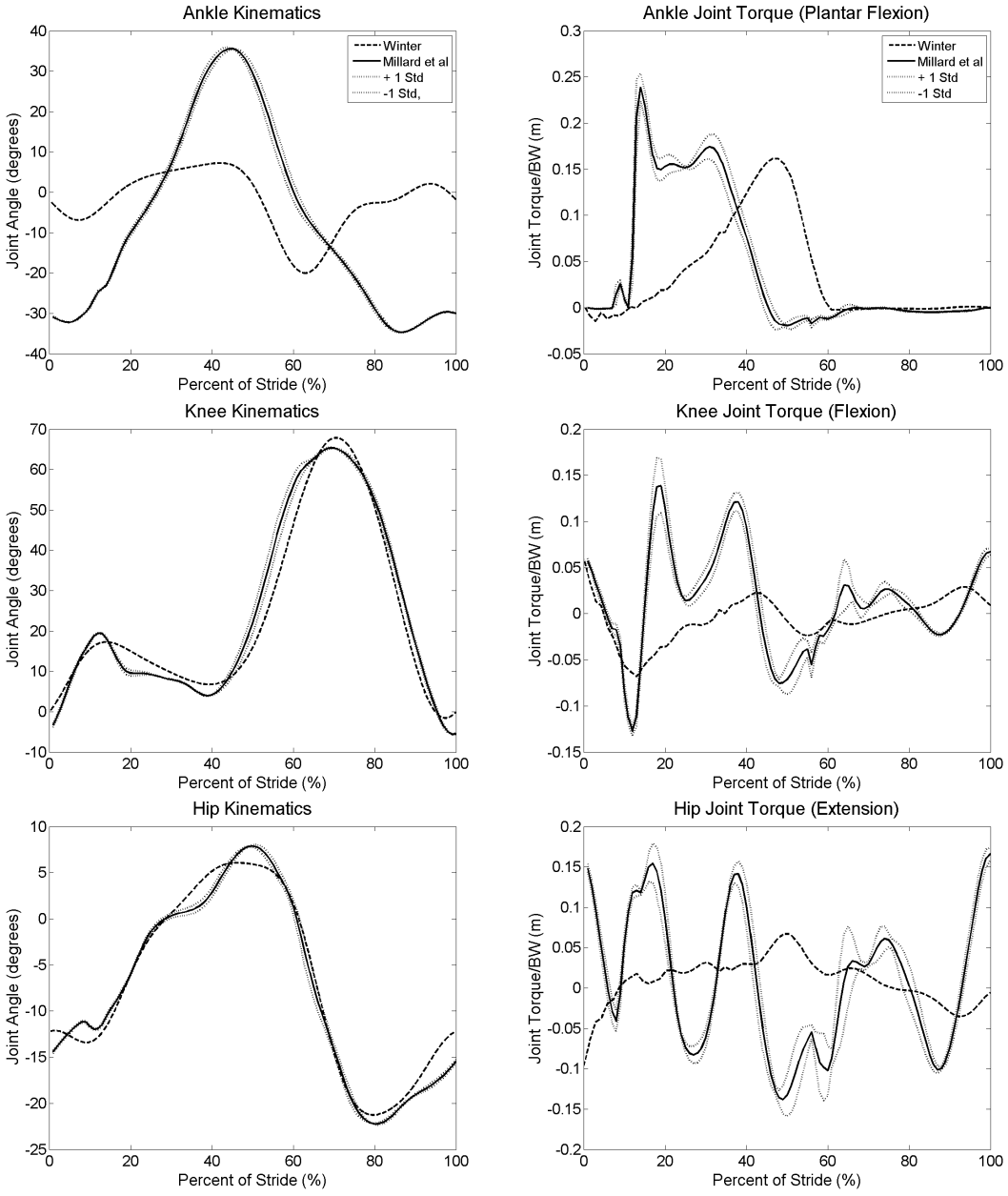

Figure 3.3: Joint trajectory and torque comparison between Winter's recordings of human gait [109], and the current results

The foot contact model produced ground reaction forces that differ substantially from those observed during normal human gait [109], as shown in Fig. 3.4. The poor performance

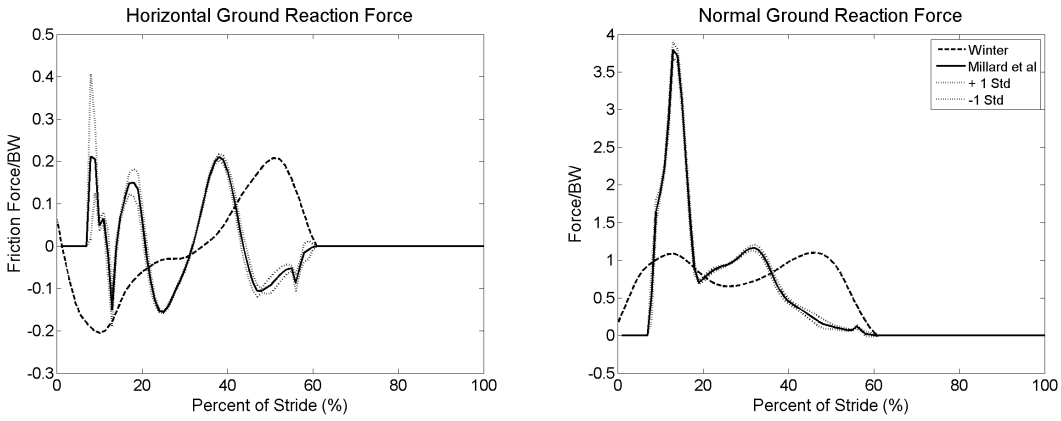

Figure 3.4: Normal and friction force comparison between Winter's recordings [109] and the current 2-point foot contact model

of the foot contact model is partly responsible for the joint torque differences seen between healthy human gait and the simulated results in Fig. 3.3. The kinematics of the foot contact model also exhibited heel and metatarsal compressions exceeding 40.0 mm, far greater than compression levels of real human heel [23] and metatarsal pads [10]. The kinematics and kinetics of this gait differ from healthy human gait [109], and are highly influenced by differences between the simulated foot contact model and a human foot.

3.7 Discussion

The balance controller of this model is so sensitive to changes in gait parameters that very little of the gait space can be searched without making the model fall. The latest optimization run consisted of 721 simulations; 543 of these simulations resulted in the model falling. As well, the current system is not well suited to making changes to single parameters without having potentially disastrous effects: changing any one of the Fourier coefficients will alter the entire gait cycle. A parameter change that improves the efficiency of the stance phase, may cause the model to fall during the swing phase. A more advanced balance control system that allows the swing and stance phases to be tuned separately would be a great improvement to the current system.

The computationally efficient, but low-fidelity foot contact model produced ground reaction forces and foot pad compressions that were drastically different than those observed in healthy human gait, and negatively affected the simulated joint kinetics. A high-fidelity foot contact model is especially important for a predictive gait simulation: contact forces at the foot will affect the loads at the joints of the legs, and thus the metabolic cost of the leg muscles. If the model does not have a realistic foot contact model, it will be impossible to produce metabolic cost estimates that correspond to what one would expect from a human [113]. A predictive gait simulation without a high-fidelity foot contact model could not converge to a 'human-like' gait.

3.8 Conclusions

Multi-step, forward-dynamic human gait simulations do not yet have the fidelity to create precise predictions of how humans would walk in new situations. Peasgood et al.'s [76] system was a first attempt at developing a predictive human gait simulation using a control-based approach. Although Peasgood et al.'s system was the first to show that prosthetic gait has a greater metabolic cost than healthy gait *in silico* using a forward dynamic simulation, the predicted kinetics of Peasgood et al.'s healthy model were significantly different from published joint kinetics of human gait found using inverse dynamics analysis [110]. A high-fidelity kinetic response is required for high-fidelity gait predictions since metabolic cost is a function of muscle tension and thus joint torque: if the kinetic response of the

model is poor, the model will not be able to converge to a human-like gait. Further work is required to improve the kinetic response of the model by developing a more realistic foot contact model, and stance limb controller.

Chapter 4

Volumetric Foot Contact Model

In Ch. 3 a model and computer simulation was presented that searched for metabolically efficient, or human-like gaits, in an effort to predict how a human might walk. Since muscles consume energy as a function of the tension they develop, and their contraction velocity [102], it is very important for the model to be able to walk with human-like muscle activations and resultant joint torques. Ground reaction force profiles heavily influence the torques that each joint must develop, and thus the energy consumed by the associated musculature. The foot contact model affects the way ground reaction forces develop, and thus how the model consumes metabolic energy. An accurate model of the foot is a necessary component for a predictive gait simulation. The ground reaction force profiles of the predictive gait simulation presented in Ch. 3 (Fig. 3.4) do not resemble experimentally measured human ground reaction profiles during walking [109], in part, because the 2-point foot contact model does not resemble a human foot.

The aim of the work presented in this chapter is to develop and validate a dynamic model of the foot that simultaneously replicates the *in vivo* kinematics and kinetics observed at the ankle [109] of human feet during the stance phase. Simulating contact is computationally intensive, and so, a lumped parameter formulation is used in this chapter in the hopes of finding a foot model that is both efficient and accurate. Although a lumped parameter formulation will not simulate the deformation of the foot pad, and thus can only be viewed as an approximation, it can calculate the net forces the foot pads exert on the foot (and thus the ankle) in a computationally efficient manner. Gonthier et al.'s [31] volumetric contact model is employed to calculate contact forces between the pads of the feet and the

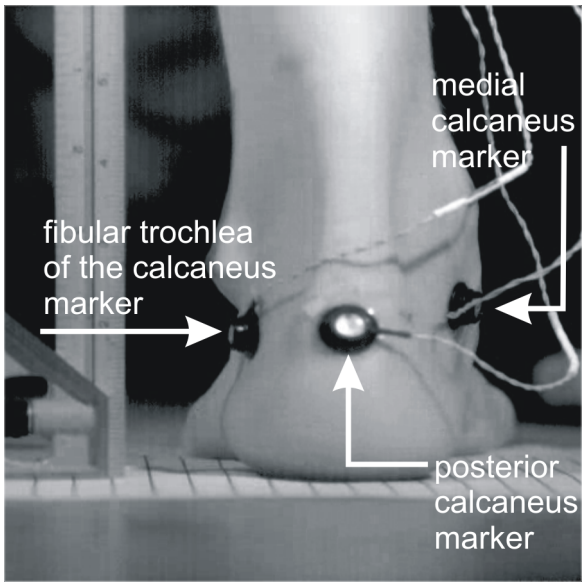

Figure 4.1: Marker array used for heel pad compression experiments

ground. A Coulomb friction model is used to calculate the shear forces between the foot pads and the ground. Both the foot pad and the foot models are validated using a novel *in vivo* approach.

4.1 Methods

The approach taken in the current work to assess candidate foot contact models is different from previous attempts [27]: a contact model that was suitable for modeling heel tissue was first identified, then candidate foot contact models were created using these contact elements. Heel pad models were validated by comparing an experimentally collected bare heel pad compression loop against the simulated version. The experimentally collected compression loop was recorded by having one subject lower and raise their heel on a force plate while the kinematics of the heel (markers placed at the medial, lateral and posterior sides of the calcaneus) were recorded using Optotrak infrared diodes (IREDs) (Fig. 4.1. The vertical displacement of the heel was used to infer the compression of the heel pad. Similarly, the foot model was validated by comparing the simulated ground reaction forces to the experimental profiles when the foot was driven through a kinematic path that

matched the experimental foot. A simple experiment was undertaken to collect the data required to test the candidate foot models: a subject's ankle position, foot orientation, and ground reaction force profiles during normal gait were recorded using Optotrak IREDs and a force plate. The subject walked at three different subjective paces (slow, normal and quickly) to assess the sensitivity of the model to different load rates typical of different walking speeds. The following sections will detail work to create and validate a new foot model based on volumetric contact.

4.2 Modelling Foot Pad Contact

Theoretical contact modelling is a very active research area [31] with relatively sparse experimental work [11, 29]. Most continuous contact models assume that the geometry of the contacting bodies does not deform, that the magnitude of the contact force is a function of the interpenetration distance and velocity, and that the direction of the contact force is a function of the normal direction of the surface geometry of each body. Contact models defined based on surface geometry properties fail to compute stable normal direction vectors [31] when the contacting bodies have discontinuous surface geometry (such as corners). A new contact model based on *interpenetration volumes* [31] has been developed that has a numerically stable means of calculating normal directions and is currently being used by the Canadian Space Agency to simulate Canadarm operations. This contact model was chosen as an ideal candidate for a new foot contact model because of its stable normal direction calculation, and because it can be used in conjunction with complicated geometry.

Gonthier et al. [31] analytically derived expressions for the normal force $\vec{f}_N$ (in direction $\hat{\mathbf{n}}$), and rolling resistance $\vec{\tau}_T$ (which is parallel to the tangential angular velocity of the two bodies $\vec{\omega}_T$) for a linearly elastic Winkler foundation of stiffness k and damping a impacted by a body with a normal velocity of v_N :

$$\vec{f}_N = kV(1 + av_N)\ \hat{\mathbf{n}} \tag{4.1}$$

$$\vec{\tau}_T = ka[J_c] \cdot \vec{\omega}_T \tag{4.2}$$

These very general expressions assume it is possible to calculate the volume of interpenetration (V), and the second moment of area of the contact surface ($[J_c]$, where square brackets denote a matrix). These parameters can be very challenging to compute for arbitrarily shaped bodies, and so analytical expressions for V and $[J_c]$ were developed for spherical primitives. The foot contact model was then created out of an array of spherical elements. Spheres were used to model the pads of the feet because they are complicated enough to approximate the geometry of the foot pads, and yet are simple enough in shape to permit analytical expressions for the volumetric properties, $[V]$ and $[J_c]$, to be symbolically derived [30].

4.3 Modelling Foot Pad Friction

Every foot contact model developed to date has made use of a Coulomb friction model without any experimental justification. There has not been any effort to date to develop experiments to determine the shear and friction properties of human heel pad *in vivo* or *in vitro*. Typically the tangential ground reaction forces found in simulated feet are accompanied by unrealistically high initial transient forces, [27, 97], or in the very least force profiles that deviate [76] from experimental ground reaction force recordings [109]. Initially a Coulomb model of Eqn.3.2 in Ch.3 was adopted to see how it would perform with the new foot contact models.

4.4 Multibody Model of the Foot

Several foot contact model topologies were considered beginning from the very simple and progressing in complexity (Fig. 4.2) to achieve the desired fidelity. Each two-dimensional foot contact model was driven at the ankle through experimentally measured foot trajectories in order to generate a simulated ground reaction force profile. An optimization routine was used to tune the geometry of the foot, contact properties of the pads (on a subset of the data, termed the training data), and the stiffness of the midfoot joint (Fig. 4.2d), in an effort to make the ground reaction force profile of the model match the experimental ground reaction force and limit the predicted maximum compression of the heel ($\approx$12 mm for the test subject's 22.8 mm thick heel pad [18]) and forefoot pads ($\approx$7 mm [10] for the test

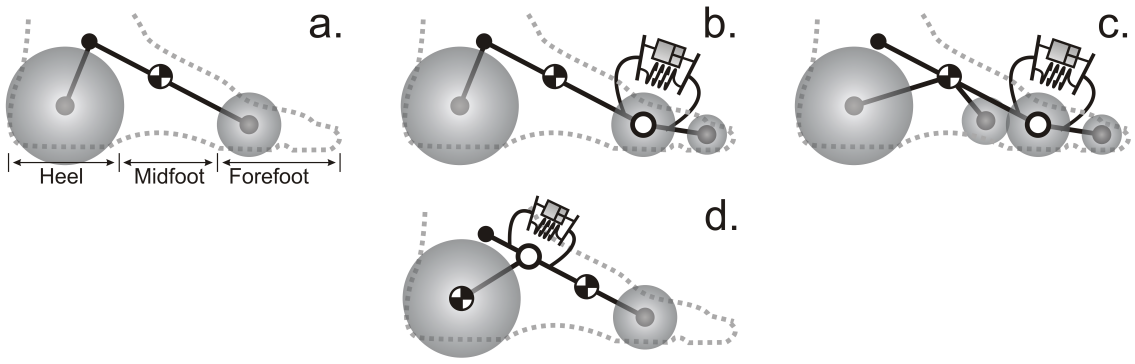

Figure 4.2: Foot contact models consisting of 2,3, and 4 spheres shown in a., b., c., and d. Models b. and c. have a flexible toe joint while model d. has a flexible metatarsal joint

subject's 13.2mm 2nd metatarsal foot pad [18]) to realistic values. A linear spring-damper element was used to model the flexibility of the midfoot as a simple first approximation for the final foot model. It is unknown at the present time if a linear spring-damper element is the most appropriate passive element to use.

The model was validated using a different set of ankle trajectories than the ones used to tune the foot model. The simulated and experimental ground reaction force profiles were compared to validate the foot model. This method of validation is very challenging because the computed ground reaction forces are be very sensitive to errors in foot geometry and foot pad contact properties. This approach is desirable because it will clearly show errors in the model. Conversely, the more conventional validation method [27, 93] of applying experimental ground reaction forces the the foot model and comparing the simulated and experimental kinematics of the foot is insensitive and will hide performance differences between the experimental and simulated feet.

4.5 Results

The heel pad compression loops (Fig. 4.3) show that a single volumetric spherical contact element is able to achieve a good agreement with the experimental *in vivo* load curves in all but one of the trials. The hysteresis loops obtained during the preliminary experiment have energy losses ranging from 21%-37%. This level of energy dissipation is higher than the

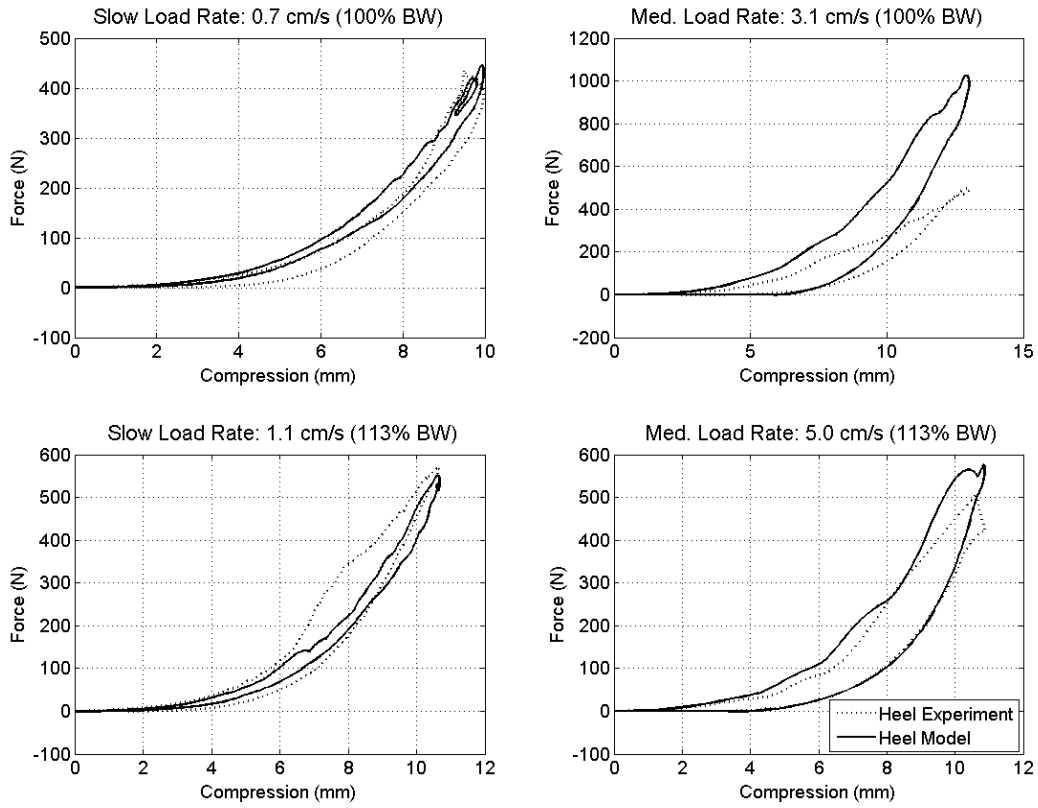

Figure 4.3: Compression load cycles of a tuned volumetric sphere vs experimental data for a single subject. Stiffness and damping are constant. The label 'BW' stands for body weight, and the load rate reported is the maximum normal velocity the heel achieves as it contacts the floor

17%-19% reported by Gefen et al.'s *in vivo* study [23] and grossly lower than the 46.5%-65.5% reported by Aerts et al. Since only one trial under each loading condition was collected it is impossible to know if the ill-fitting trial is a consequence of the 'memory' of foot tissue observed *in vitro* [3], or skin movement artifact, or due to a fundamental difference between the contact model and the contact properties of human heel pads.

The first three foot contact models (Fig. 4.2) feature a rigid foot with variations on the toes. It proved difficult to adjust the properties of these foot models without excessive forefoot pad compression, particularly at the end of stance. Human feet actually flex

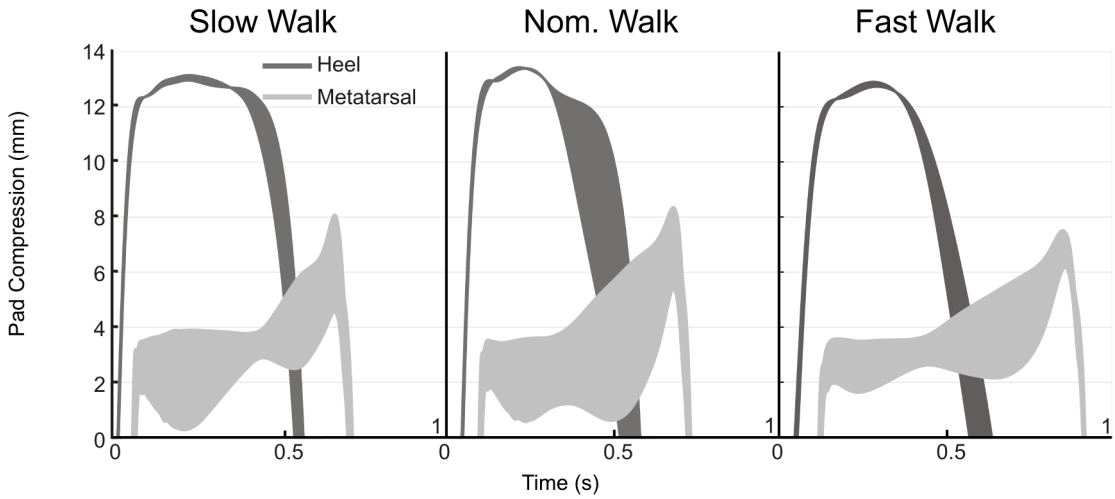

Figure 4.4: Simulated heel (dark grey) and metatarsal (light grey) pad compressions. The thickness of each of the bands spans from ± 1 standard deviation

slightly through the mid foot at the tarsal joints (10° is typical [9, 34]) during stance. This additional flexibility between the forefoot and the heel was introduced in the final foot contact model (Fig. 4.2 d.), making it possible to adjust the midfoot stiffness of the foot such that the virtual heel and forefoot pads underwent a realistic amount of compression (Fig. 4.4).

Tuning the geometric and contact properties of the final foot contact model (Fig.4.2 d.) such that the virtual and experimental ground reaction force profiles matched was very challenging. Several different optimization approaches were employed using Matlab, including a Newton-Levenburg search, the simplex method, and a genetic algorithm. The best contact profile results (Fig. 4.5) were obtained by hand tuning the final parameters (see App. B for details) returned by a genetic algorithm. Although the simulated heel and forefoot pads underwent a plausible 50% compression during stance [10] (Fig. 4.4) — while there is one *in vivo* recording of the compression of the 2^{nd} metatarsal foot pad during walking [10], there are not corresponding recordings of the compression of the heel pad during walking in the literature — the vertical ground reaction force profiles only crudely resemble the experimental data (Fig. 4.5). The simulated horizontal force profiles (Fig. 4.6) bare no resemblance the experimental profiles.

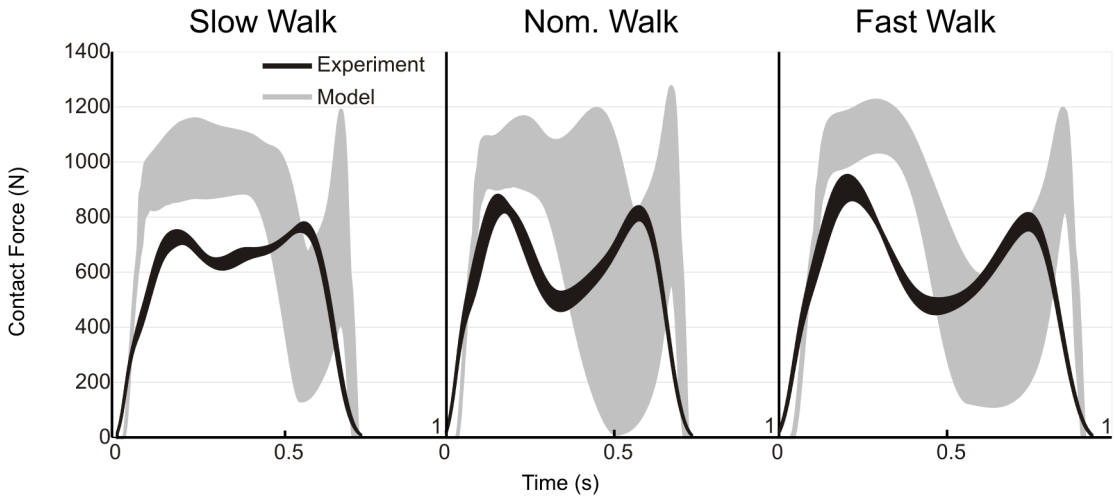

Figure 4.5: Simulated (gray) and experimental (black) vertical ground reaction force profiles. The thickness of each of the bands spans ±1 standard deviation

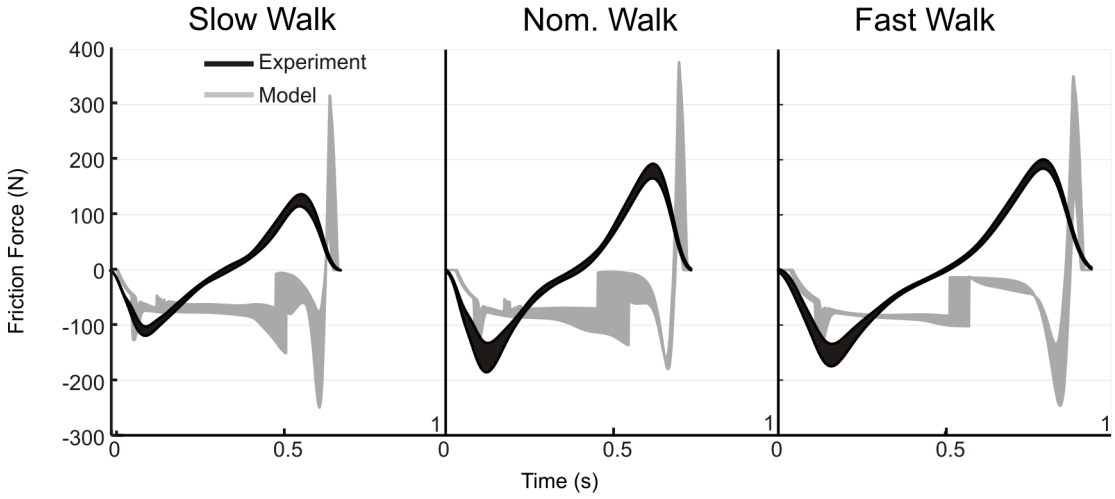

Figure 4.6: Simulated (gray) and experimental (black) horizontal ground reaction force profiles. The thickness of each of the bands spans ±1 standard deviation

4.6 Discussion

Insight into the poor performance of the foot contact model may be gained by closely examining the properties of the simulated results. Since the experimental vertical and

horizontal ground reaction force profiles have small standard deviations, the compression and shear profiles of the experimental heel and forefoot pads (not measured) will likely also have small standard deviations. In contrast, the standard deviation of the compression of the simulated foot pads is quite large (Fig. 4.4). Since the model is identical during each of the trials, the variation in foot pad compression originates from the kinematic data that is being used to drive the foot. When the experimental foot pads deform and metatarsals splay during stance, the skin covering the foot stretches and moves the optical markers (relative to the foot bones) in the process. The distance between the lateral and medial calcaneus markers, which should be constant, was examined to estimate skin stretch: the distance of 68.0 mm changed by 2.0 mm on average during a load cycle, indicating that skin stretch has likely skewed the data.

Videofluoroscopy is a cinematic X-ray technology that can capture both Optotrak IREDs and the bones of the feet during the stance phase of walking. A unique video showing both the bones of the foot, and Optotrak IREDs attached to the skin (courtesy of Prof. Tom Jenkins [100]) clearly shows a significant amount of movement between the Optotrak IREDs and the bones of the foot (Fig. 4.7). Several foot bone-marker pairs were registered (using the outline of the bones) across twenty frames (recorded at 30 Hz) to reveal skin movement on the order of 5-15 mm (Fig. 4.7) during stance. This level of kinematic noise is unacceptable because the compression and shear of the experimental foot pads is equal to, or less than the kinematic noise present in the Optotrak data. Although it is encouraging that the vertical force and foot pad compression profiles crudely approximate a real foot, the kinematic data used to drive the foot is not accurate enough to validate the contact model definitively.

4.7 Conclusions

The joint torque profiles of the simulated gait are highly influenced by the ground reaction forces applied at the foot. Foot contact models were created using spherical elements and contact forces were calculated using Gonthier et al.'s volumetric contact model. The models were validated by driving the heel through experimentally recorded calcaneus trajectories and examining the quality of match between the ground reaction forces developed at the simulated foot, and the human foot. Current modelling efforts indicate that it is important

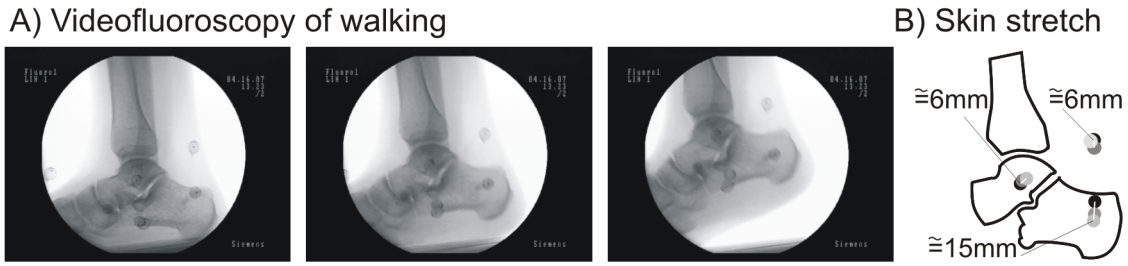

Figure 4.7: Videofluoroscopy of foot skin stretch during walking A). The movement of each marker relative to the skeleton is apparent when each of the markers is registered using the outline of the foot bones B). These images were reproduced with permission of Prof. Tom Jenkins [100]

to represent the heel, and metatarsal foot pads in the contact model as well as the flexibility of the mid-foot. The results of the contact and friction model validation were not ideal due to excessive skin movement artifact present in the experimentally measured stance foot kinematics. More accurate means of experimentally measuring the stance foot and foot pad kinematics are required before the foot contact models can be validated thoroughly using the methodology employed in this study.

Chapter 5

Predicting Human Gait using Simple Models and Torso Trajectories

As noted in Ch. 4, ground reaction force profiles affect the way the model consumes metabolic energy, and ultimately the final gait the predictive system deems most human-like. Ground reaction forces are not only influenced by the way the foot is modeled, but by the way the stance leg is controlled. The ground reaction force profiles of the predictive gait simulation presented in Ch. 3 (Fig. 3.4) do not resemble experimentally measured human ground reaction profiles during walking [109] due to both the poor representation of the foot, and the way the stance limb is controlled. Although there are a number of multibody forward-dynamic gait simulations in the literature [2, 5, 96, 97, 112], a stance limb controller that yields human-like ground reaction force profiles does not yet exist. Multibody models walk poorly because it is difficult to formulate controllers for such systems due to their large, inherently unstable, nonlinear, and high-dimensional equations of motion. In contrast, the simple spring-loaded inverted-pendulum (SLIP) model can be tuned to emulate human COM and GRF profiles during steady state walking and running with an accuracy that is unmatched by any other model [7, 26].

This chapter focuses on using control to embed the desirable COM and GRF profiles of the SLIP model into an anthropomorphic multibody model to make its gait more human-like. The intent of this approach is to partition the very difficult problem of simulating human walking using an anthropomorphic model into two simpler problems. The low-dimensional SLIP model is used to compute human-like torso kinematics that the control

system of the anthropomorphic model uses to compute the hip, knee, and ankle torques required to accomplish this motion on the multibody model. It should be noted that the second part of this approach may seem like an inverse dynamics simulation, but it is still a forward-dynamics simulation because only the desired kinematics of the torso are defined; the kinematics of the legs are not. The state of the legs is not controlled, but allowed to evolve during stance as the multibody model moves.

Torso tracking control systems are developed for a series of dynamic models, of increasing likeness to a human (Fig. 5.1), to assess the feasibility of this approach. The tracking controllers are formulated using input-output feedback linearization [49]. In this application, input-output feedback linearization is identical to enforcing position and velocity-level constraints (the trajectory of the torso in this case) at the acceleration level — making it equivalent to a computed torque controller — using the actuators of the system. Penalty terms for position and velocity errors are included in the acceleration constraint to ensure that the model eventually satisfies the desired trajectory. The first model presented is the standard SLIP model and Poulakakis and Grizzle's monopedal (to simulate running) asymmetric spring-loaded inverted-pendulum (ASLIP), an extension to the SLIP. A bipedal extension (Fig. 5.1C) to Poulakakis and Grizzle's monopedal ASLIP [79] is then presented. Next, a torso tracking control system is developed to allow a model with massless anthropomorphic legs (Fig. 5.1D)— the legged asymmetric spring-loaded inverted-pendulum (LASLIP) — to walk with a torso trajectory that matches the SLIP model. Finally, the chapter concludes by developing a torso-tracking control system for an 11 DOF, bipedal sagittal-plane gait model with simulated foot contact. In each case the control system formulation is presented, followed by an evaluation using numerical simulation.

5.1 The SLIP and ASLIP models

The standard planar SLIP model (denoted with a subscript 'S' in equations) consists of a point mass (m), with two massless linear springs with a fixed resting length (r_0) and no preload (Fig. 5.1A). Each leg behaves like a massless prismatic joint (actuated by forces of magnitude $p_{S,1}$ and $p_{S,2}$) connected to the ground (during stance) with revolute joints. Although the dynamic equations of the SLIP model, Eqns. 5.1-5.2 , are very simple, it can be made to walk or run with human-like GRF and COM profiles [26] using optimized

initial conditions selected to yield limit-cycle walking or running.

$$\ddot{x}_S = \frac{1}{m} f_{Sx} \tag{5.1}$$

$$\ddot{y}_S = \frac{1}{m}(f_{Sy} - mg) \tag{5.2}$$

The legs of the SLIP behave like linear springs attached to the ground through a revolute joint at point (cx_i, cy_i) until the foot leaves the ground (when $r_0 + \frac{y_S}{\sin(\alpha_{S,i})} < 0$, note $\alpha_{S,i}$ is negative) putting the leg into swing. The swing limb is held at a constant angle ϕ_S relative to the stance limb until the foot contacts the ground (when $r_0 + \frac{y_S}{\sin(\alpha_{S,i})} \geq 0$). It is assumed that the spring freely rotates about both the mass and the ground during stance, and that the contact end of the spring sticks and does not slip.

The net force acting on the point mass, (f_{Sx}, f_{Sy}), can be found using Eqns. 5.4 and 5.5 as the sum of the spring forces generated by each leg defined in Eqn. 5.3. The variable n is used throughout the equations in this paper to denote the number of legs in contact with the ground; n is set to 1 for single stance, and 2 for double stance.

$$p_{S,i} = -k_i(r_i - r_0) \tag{5.3}$$

$$f_{Sx} = \sum_{i=1}^{n} -p_{S,i}\cos(\alpha_{S,i}) \tag{5.4}$$

$$f_{Sy} = \sum_{i=1}^{n} -p_{S,i}\sin(\alpha_{S,i}) \tag{5.5}$$

Substituting in Eqns. 5.3-5.5 into Eqns. 5.1-5.2 yields the dynamic equations of motion for a monopedal SLIP (n set to 1) and the bipedal SLIP (n set to 2) during stance.

$$\ddot{x}_S = \frac{1}{m}\sum_{i=1}^{n} k_i(r_i - r_0)\cos(\alpha_{S,i}) \tag{5.6}$$

$$\ddot{y}_S = \frac{1}{m}\left(\sum_{i=1}^{n} k_i(r_i - r_0)\sin(\alpha_{S,i}) - mg\right) \tag{5.7}$$

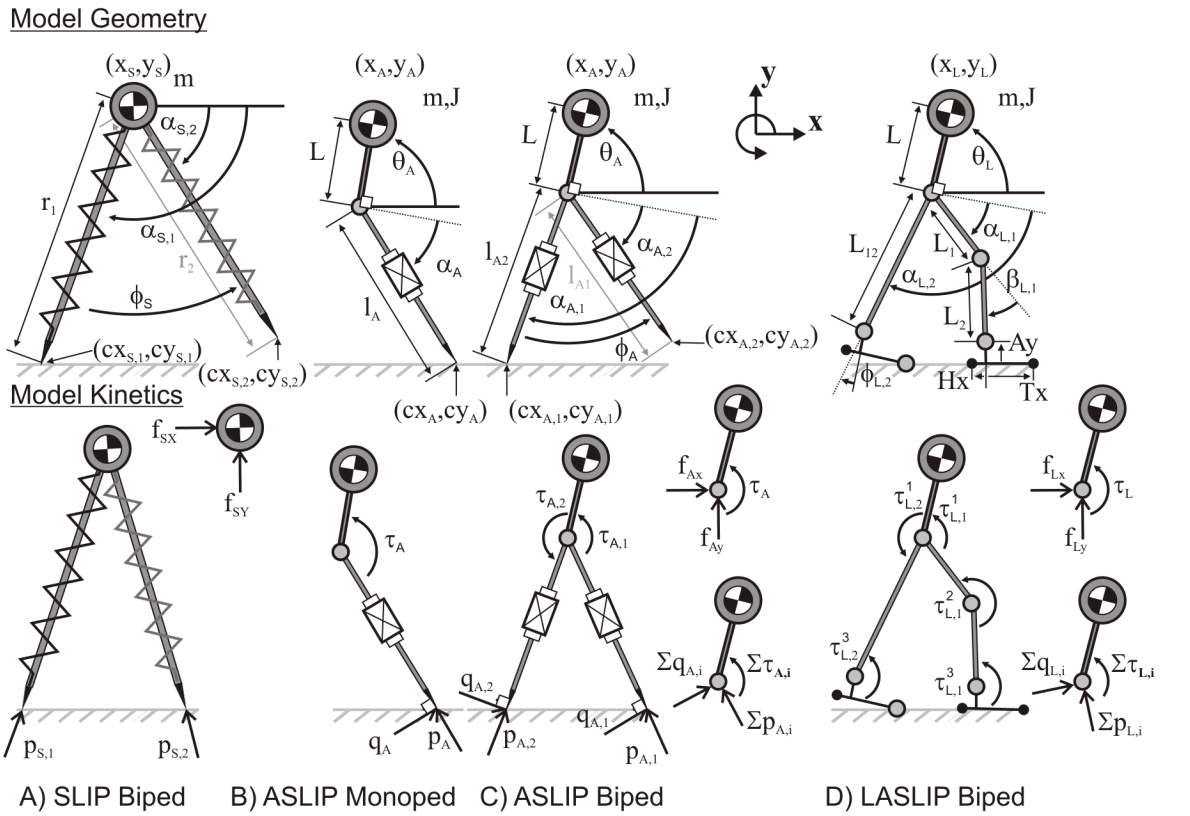

Figure 5.1: The bipedal SLIP model is shown in panel A). The monopedal ASLIP [79] is shown in panel B). The bipedal ASLIP developed in this work is in panel C). The anthropomorphic LASLIP model is pictured in panel D). Not all of the angles and torques have been drawn in the positive sense due to space restrictions. The sign of each angle and torque follows the right hand rule

The ground reaction force profiles and COM kinematics of human gait and the gait of the SLIP model can be very similar [26], which suggests that humans control their legs to behave like linear springs during steady state walking and running. The similarity can be further improved if the contact point is translating forward at a constant velocity that is matched to the average center of pressure velocity of the human [7]. Sliding the SLIP model forward at a constant velocity fortunately does not affect its equations of motion.

The SLIP model can be made to resemble the human form more closely by adding a hip joint and a torso above the massless legs. Poulakakis and Grizzle introduced an asymmetric monopedal (running) SLIP model (ASLIP, denoted with a subscript 'A') that

included a torso, with the linear leg actuators terminating at a hip joint (Fig. 5.1B). The equations of motion of the ASLIP, Eqns. 5.8-5.10, are very similar to those of the SLIP but include torso (of mass m and inertia J) dynamics, which are a critical component for an anthropomorphic gait model.

$$\ddot{x}_A = \frac{1}{m} f_{Ax} \tag{5.8}$$

$$\ddot{y}_A = \frac{1}{m}(f_{Ay} - mg) \tag{5.9}$$

$$\ddot{\theta}_A = \frac{1}{J}(L(f_{Ax}\sin(\theta) - f_{Ay}\cos(\theta)) + \tau_A) \tag{5.10}$$

The forces applied to the hip (horizontal f_{Ax} and vertical f_{Ay} forces) are no longer simply spring forces, but are the sum of the forces generated by the linear actuator $p_{A,i}$, and the reaction force $q_{A,i}$ created by the applied hip torque τ_A, as shown in Eqns. 5.15-5.16.

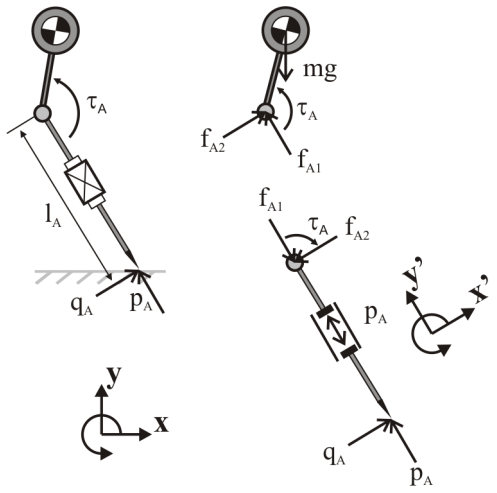

Figure 5.2: Free body diagram of the ASLIP. The leg has been drawn to emphasize that it behaves like a massless telescoping force actuator

A statics analysis (Fig. 5.2) of the massless leg can be used to obtain the expressions for the forces and torques applied to the torso. In the local (x', y') axis parallel to the leg we

have

$$\sum F \cdot \hat{x}' = 0,\ q_A - f_{A2} = 0 \tag{5.11}$$

$$\sum F \cdot \hat{y}' = 0,\ p_A - f_{A1} = 0 \tag{5.12}$$

$$\sum \tau = 0,\ -\tau_A + q_A l = 0 \tag{5.13}$$

$$\tag{5.14}$$

Solving Eqns. 5.11-5.13 for the net force applied to the torso ($f_{A2}\hat{x}' + f_{A1}\hat{y}'$) as a function of the actuator outputs (p_A and τ_A), and resolving the result into the global coordinate frame yields

$$f_{Ax} = \sum_{i=1}^{n} -p_{A,i}\sin(\theta + \alpha_{A,i}) + \frac{\tau_{A,i}}{l_{A,i}}\cos(\theta + \alpha_{A,i}) \tag{5.15}$$

$$f_{Ay} = \sum_{i=1}^{n} p_{A,i}\cos(\theta + \alpha_{A,i}) + \frac{\tau_{A,i}}{l_{A,i}}\sin(\theta + \alpha_{A,i}) \tag{5.16}$$

Substituting in Eqns. 5.15-5.16 into Eqns. 5.8-5.10 gives the equations of motion of the ASLIP during single stance (n=1) and double stance (n=2) phases. Note that since Poulakakis and Grizzle's ASLIP model is monopedal, it only makes use of the single stance ($n = 1$) phase.

$$\ddot{x}_A = \frac{1}{m}\sum_{i=1}^{n}\left(-p_{A,i}\sin(\theta + \alpha_{A,i}) + \frac{\tau_{A,i}\cos(\theta + \alpha_{A,i})}{l_{A,i}}\right) \tag{5.17}$$

$$\ddot{y}_A = \frac{1}{m}\sum_{i=1}^{n}\left(p_{A,i}\cos(\theta + \alpha_{A,i}) + \frac{\tau_{A,i}\sin(\theta + \alpha_{A,i})}{l_{A,i}}\right) - g \tag{5.18}$$

$$\ddot{\theta}_A = \frac{1}{J}\sum_{i=1}^{n}\left(\tau_{A,i}\frac{l_{A,i} - L\sin(\alpha_{A,i})}{l_{A,i}} - Lp_{A,i}\cos(\alpha_{A,i})\right) \tag{5.19}$$

5.2 ASLIP Single Stance Phase Control

Poulakakis and Grizzle developed the planar, monopedal ASLIP, an extension to the SLIP model that includes a torso (Fig. 5.1 B). The ASLIP is able to run exactly like a SLIP model using the control laws that Poulakakis and Grizzle formulated that embedded the dynamics of the SLIP model into the closed-loop equations of the ASLIP. Poulakakis and Grizzle chose the hip torque, τ_A, to regulate the orientation of the torso of their single stance — single stance and monopedal are equivalent terms — model using input-output feedback linearization [49]. This control law can be found by setting the angular acceleration of the torso to an error term ν, as shown in Eqn. 5.20, and solving for τ_A as in Eqn. 5.21.

$$\ddot{\theta}_A = \nu_\theta \tag{5.20}$$

The hip torque that regulates the orientation of the torso to the error term ν_θ that can be found by substituting Eqn. 5.20 into Eqn. 5.10 and solving for τ_A.

$$\tau_A = \nu_\theta J - L(f_{Ax}\sin(\theta_A) - f_{Ay}\cos(\theta_A)) \tag{5.21}$$

After substituting in Eqns. 5.15-5.16 for the single stance phase, Eqn. 5.21 becomes

$$\tau_A = l_A \frac{\nu J + L p_A \cos(\alpha_A)}{l_A - L\sin(\alpha_A)} \tag{5.22}$$

where all of the above subscript A terms refer to quantities associated with the monopedal ASLIP model (Fig. 5.1 B). Poulakakis and Grizzle formulated the feedback error term,ν, for single stance, to render the desired orientation of the torso, θ_0, to an exponentially stable set point. The subscript A is left off the θ below, as this equation is used for the ASLIP, LASLIP and multibody models.

$$\nu_\theta = -K_\theta(\theta - \theta_0) - D_\theta\dot{\theta} \tag{5.23}$$

After performing a coordinate transformation, Poulakakis and Grizzle arrived at a control law for the leg force, p_A, that renders the dynamic equations of the ASLIP identical to the SLIP when $\nu_\theta = 0$.

$$p_A = \frac{l_A - L\sin(\alpha_A)}{r_A} p_S \tag{5.24}$$

The nonlinear coordinate transformation required to map the state equations of the ASLIP to those of the SLIP is quite involved because both the SLIP and ASLIP models are underactuated (they have few actuators than degrees of freedom). Refer to Poulakakis's thesis [78] and Isidori [44](Ch. 4) for details.

Substituting Eqns. 5.22 and 5.24 into Eqns. 5.17-5.19 for the single stance phase case ($n = 1$) results in the closed-loop equations of motion for the monopedal ASLIP model.

$$\ddot{x}_A = \frac{(l_A - L\sin(\alpha_A))(l_A\sin(\theta_A + \alpha_A) - L\cos(\theta_A))\frac{p_S}{r} - \cos(\theta_A + \alpha_A)\nu J}{m(L\sin(\alpha_A) - l_A)} \tag{5.25}$$

$$\begin{aligned}\ddot{y}_A = &\frac{(l_A - L\sin(\alpha_A))(-l_A\cos(\theta_A + \alpha_A) - L\sin(\theta_A))\frac{p_S}{r}}{m(L\sin(\alpha_A) - l_A)} \\ &+\frac{mg(l_A - L\sin(\alpha_A)) - \nu J\sin(\theta_A + \alpha_A)}{m(L\sin(\alpha_A) - l_A)}\end{aligned} \tag{5.26}$$

$$\ddot{\theta}_A = \nu \tag{5.27}$$

After making use of a trigonometric identity (detailed in Poulakakis thesis [78]), the closed loop ASLIP equations become identical to the dynamic equations of the SLIP (Eqns. 5.6 and 5.7) but only when the torso of the ASLIP is being perfectly regulated ($\nu = 0$). The ASLIP and SLIP COM accelerations will differ when the torso of the ASLIP is not at the desired set point ($\nu \neq 0$ because $\theta_A \neq \theta_0$ and/or $\dot{\theta}_A \neq 0$) due to the extra hip torque that is required to regulate the orientation of the torso to the desired set point.

5.3 ASLIP Double Stance Phase Control

Here we extend Poulakakis and Grizzle's single stance ASLIP controller to function during double stance. The bipedal ASLIP and SLIP models both have a single stance phase as before, but now they also have a double stance phase which is necessary to simulate walking. In order to emulate the SLIP model during double stance, a control law must

be derived that renders the closed loop bipedal ASLIP dynamic equations identical to the dynamic equations of the SLIP model.

$$\ddot{x}_A = \ddot{x}_S \tag{5.28}$$

$$\ddot{y}_A = \ddot{y}_S \tag{5.29}$$

$$\ddot{\theta}_A = \nu_\theta \tag{5.30}$$

The expression for the two hip torques ($\tau_{A,1}$ and $\tau_{A,2}$) that satisfy Eqn. 5.30 can be found by setting $\ddot{\theta}_A = \nu_\theta$ in Eqn. 5.19 and solving for $\tau_{A,1}$ and $\tau_{A,2}$.

$$\sum_{i}^{2} \tau_{A,i} \left(\frac{l_{A,i} - L\sin(\alpha_{A,i})}{l_{A,i}} \right) = \nu J + \sum_{i=1}^{2} L p_{A,i} \cos(\alpha_{A,i}) \tag{5.31}$$

During double stance the ASLIP model is overactuated because Eqn. 5.31 shows that there are four control variables to solve for (two hip torques $\tau_{A,1}$, $\tau_{A,2}$ and two leg forces $p_{A,1}$, $p_{A,2}$) yet only three equations, Eqns. 5.28-5.30, that these leg forces and hip torques need to satisfy. Although there is no unique solution to this system of equations, it can be solved analytically if a fourth equation is introduced. Here we introduce a fourth equation that constrains the torque generated by each hip to be proportional to the vertical component of the ground reaction force beneath each corresponding telescoping leg ($f_{Ly,1}$ and $f_{Ly,2}$). A physical interpretation of this heuristic is that torque is shared between each hip according to how much traction is present under the respective foot, an important consideration given that hip torques will usually create a relatively large horizontal ground reaction force. Note that Eqn. 5.32 is a convenient heuristic, as it is not presently known how humans share torque across their hips during double stance.

$$\frac{\tau_{A,1}}{f_{Ay,1}} - \frac{\tau_{A,2}}{f_{Ay,2}} = 0 \tag{5.32}$$

Since the four equations (Eqns. 5.28- 5.32) are linear in the four unknowns of interest ($\tau_{A,1}$, $\tau_{A,2}$, $p_{A,1}$ and $p_{A,2}$), they can be solved symbolically (using Maple [60]). The solution yields expressions for the two hip torques ($\tau_{A,1}$ and $\tau_{A,2}$) and leg forces ($p_{A,1}$ and $p_{A,2}$) that when substituted into the dynamic equations of the ASLIP will regulate the orientation of

the torso and cause the COM trajectory of the ASLIP and SLIP models to match. The solutions for the previously described leg forces and hip torques are not reproduced in this manuscript due to their unwieldy size (the final expressions span several pages). As a note, this system of four equations linear in 4 unknowns can also be solved numerically. The performance differences between the symbolic and numeric solutions is presently not known, and is left as a topic for future work.

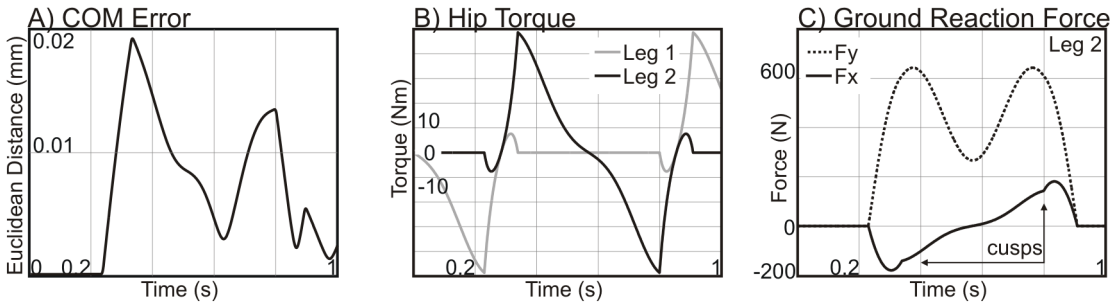

Figure 5.3: Simulation results for a bipedal ASLIP model. The Euclidean distance between the bipedal ASLIP COM and SLIP COM is shown in panel A). The hip torques of the bipedal ASLIP during steady state walking are shown in panel B). The ground reaction forces generated by Leg 2 are shown in panel C)

The bipedal ASLIP and a bipedal SLIP (Eqns. 5.1-5.2) models were simulated (using ode45 in Matlab Simulink [61]) for comparison purposes. The bipedal ASLIP was simulated by using Poulakakis and Grizzle's closed loop expressions Eqns. 5.25-5.27 during single stance, and then Eqns. 5.17-5.19 ($n = 2$) using the solutions to Eqns. 5.28- 5.32 for the hip torques ($\tau_{A,1}$,$\tau_{A,2}$) and leg forces ($p_{A,1}$, $p_{A,2}$) during double stance. The bipedal SLIP model was simulated using Eqns. 5.6-5.7. The parameters chosen for the models were consistent with those of an $1.80\,m$ tall, $80\,kg$ man walking at $1.2\,m/s$. The mass and inertia of the ASLIP and SLIP models represent the mass and inertia of the head, arms and trunk of this person (in this case $m = 54.2\,kg$, $J = 3.6\,kg\,m^2$) calculated using anthropometric tables [110]. The legs of the bipedal SLIP model had a stiffness of $13\,kN/m$ and were held $\phi_{SW} = 0.6$ radians apart during swing. The stiffness of the legs was chosen to be consistent with the natural frequency ($f = \sqrt{k/m}$) of a translating SLIP model that closely matches the COM and COP profiles of a human [26]. The swing angle of the ASLIP model, $\phi_{A,SW}$, was set so that the feet of both the SLIP and the ASLIP would coincide. The initial conditions of the model and the swing angle were selected using optimization (using

fminsearch in Matlab) to yield a gait with a stable limit cycle.

Simulation results show that that there are subtle but marked differences between the gait of the bipedal ASLIP and human gait. The ASLIP is able to regulate its torso far more accurately (within 2e-16 radians, of the desired orientation) than the $1^\circ - 2^\circ$ of torso sway that is typical of human gait [109] because its hip torques are not bandwidth limited. The sharp change in hip torque as the leg transitions from single to double stance (and vice versa) causes a subtle cusp in the horizontal ground reaction force profile (Fig. 5.3 C) that is not present in human ground reaction force profiles. Despite these subtle differences, the ground reaction force profiles closely emulate human profiles in contrast to the multibody model presented in Ch. 3 (Fig. 3.4).

5.4 Bipedal Articulated Leg ASLIP Model

Here we present the articulated-leg bipedal ASLIP (LASLIP), an anthropomorphic extension of the bipedal ASLIP model. The main purpose of the LASLIP (Fig. 5.1D) is to serve as a relatively simple test case to evaluate the quality of a partitioned approach to simulating human gait. The LASLIP model is well suited for this task because it has the same leg joints as an anthropomorphic multibody gait model (allowing the joint torques of the LASLIP to be compared to human joint torques), yet relatively concise equations of motion. The equations of motion of the model are kept to a manageable size by modeling the legs as massless links, foot contact as a revolute joint or a unilateral constraint, and by selectively locking the knee to ensure that each leg has only 3 degrees-of-freedom (DOF) during stance. The knee was chosen to be locked (rather than the hip or ankle) during heel-contact and toe-off because the hip joint is required to balance the torso at all times, and the ankle is required for propulsion at toe-off [109]. These simplifications yield concise equations of motion that greatly simplify the development and analysis of a bipedal SLIP mapping for the anthropomorphic legs of the LASLIP model.

5.4.1 Leg Kinematics

The bipedal SLIP and ASLIP models are used as geometry references to help determine the hip, knee and ankle angles of the articulated legs of the LASLIP. The leg posture of the

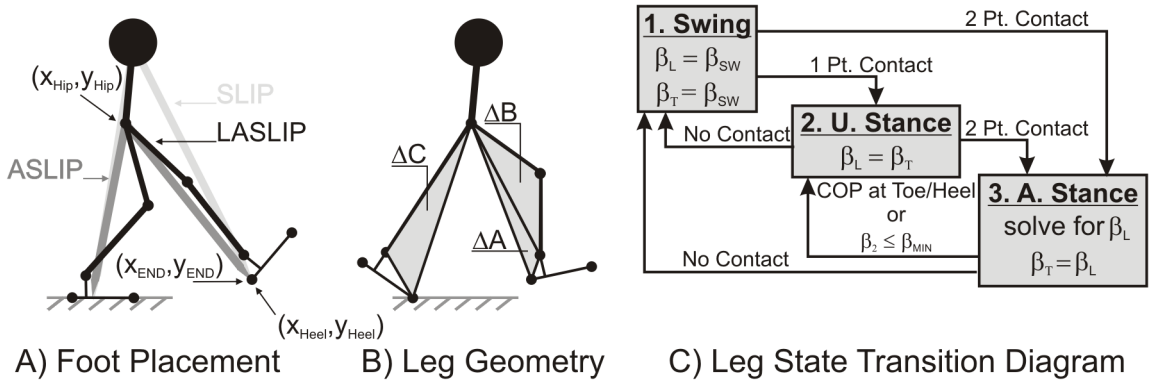

Figure 5.4: LASLIP foot placement relative to the contact point of the SLIP in A). During stance the posture of the legs are found by solving a series of triangles B). The knee remains at a fixed angle when the leg is in swing, or underactuated stance (in contact at a point), and is free to vary during (flat-footed) stance as described in C)

LASLIP model is calculated at every time step using its hip joint (x_{Hip}, y_{Hip}) location, foot geometry and knee angle (which is sometimes fixed); the location of the contact point of the SLIP model (x_{END}, y_{END}); and the sine and cosine laws. The unloaded length of the SLIP and ASLIP legs (r_i and l_i) have to be matched (prior to simulation) to the anthropometry of the legs of the LASLIP, and the range of the hip angles limited, to ensure that the SLIP and ASLIP contact points are always in the workspace of the articulated leg.

The knee of the LASLIP is locked during certain parts of the gait cycle to ensure that each leg has only 3 DOF. The state of the leg is used to determine if the knee should be locked, and at what angle it should be fixed. The leg can be in one of 3 states (Fig. 5.4C): swing, underactuated stance (u.stance) and actuated stance (a.stance). The leg is underactuated when the foot is in contact with the ground at a single point (at either the toe or the heel) since the contact point acts like a revolute joint. The leg is fully actuated when the foot is flat on the ground (and the COP of the foot is between the heel and toe) because the model has 3 DOF, and 3 actuated joints (hip, knee and ankle). The knee is locked in the underactuated leg states, and free to rotate when the leg is fully actuated. The knee is also locked to β_{MIN} before it is perfectly straight ($\beta_L = 0$) to avoid a singularity in the forces applied to the hip joint (described later in Eqns. 5.37 and 5.38).

The hip, knee and ankle angles are computed geometrically by applying the sine and cosine laws to the triangles between the hip, knee, ankle and a contacting point on the foot

(Fig. 5.4B). It is assumed that the heel (toe) is in contact with the ground when the COM is behind (ahead) the ankle. During swing, the knee is fixed and the heel of the LASLIP model is placed so that it aligns with the SLIP contact points (Fig. 5.1D), satisfying Eqn. 5.33.

$$(x_{Heel}, y_{Heel})^T = (x_{END}, y_{END})^T \tag{5.33}$$

The hip and ankle angles can be solved for during swing and heel contact by applying the sine and cosine laws to triangles ΔA and ΔB (Fig. 5.4B), because the knee is fixed at a predefined angle β_{SW}. The predefined angle for the knee during swing just prior to contact, β_{SW}, must be chosen prior to simulation. The hip, knee and ankle angles can be solved for during actuated stance by applying the sine and cosine laws to triangles ΔA and ΔB if the COM is behind the ankle, or ΔB and ΔC if the COM is ahead of the ankle. It is necessary to use different pairs of triangles to solve for the hip, knee and ankle angles because the area of triangles ΔA and ΔC will be zero in some postures, but not simultaneously. When the actuated stance phase has ended, the knee is locked at its last valid angle if it has not reached β_{MIN}. During toe-off, the hip and ankle angles can be found by applying the sine and cosine laws to triangle ΔC (Fig. 5.4C).

5.4.2 Torso Dynamics

The dynamic equations of the torso are identical to those of the ASLIP (Eqns. 5.8-5.10), though the applied forces and torques (f_{Lx}, f_{Ly}, τ_L) are different.

$$\ddot{x}_L = \frac{1}{m} f_{Lx} \tag{5.34}$$

$$\ddot{y}_L = \frac{1}{m}(f_{Ly} - mg) \tag{5.35}$$

$$\ddot{\theta}_L = \frac{1}{J}(L(f_{Lx}\sin(\theta) - f_{Ly}\cos(\theta)) + \tau_L) \tag{5.36}$$

The forces applied to the hips of the LASLIP are nonlinear functions of the torques applied at the hip, ankle and knee joints. Different equations are used when the knee is locked that only depend on the hip and ankle joint torques. Since the legs are massless, the equations

for f_{Lx} and f_{Ly} only depend on the torques applied to each joint and the posture of the leg. Despite these simplifications, the equations for f_{Lx} and f_{Ly} (derived using MapleSim [60]) have to be left in functional form because they are too large to print.

$$f_{Lx} = \sum_{i=1}^{2} F_x(\tau_{L,i}^1, \tau_{L,i}^2, \tau_{L,i}^3, \theta, \alpha_{L,i}, \beta_{L,i}, \phi_{L,i}) \tag{5.37}$$

$$f_{Ly} = \sum_{i=1}^{2} F_y(\tau_{L,i}^1, \tau_{L,i}^2, \tau_{L,i}^3, \theta, \alpha_{L,i}, \beta_{L,i}, \phi_{L,i}) \tag{5.38}$$

$$\tau_L = \sum_{i=1}^{2} \tau_{L,i} \tag{5.39}$$

The force applied at the hip joint is not a function of the foot contact force because foot-ground contact is being modeled using unilateral constraints. The contact is modeled as an instantaneous revolute joint when the foot is rotating about the heel or toe. When the foot is flat on the ground, the foot is assumed to be fixed to the ground, and the ankle is free to rotate as long as the COP stays within the base of the foot. It is assumed that the foot does not slip in the horizontal direction, as is conventionally done with the SLIP and ASLIP models.

5.4.3 Mapping Linear Leg Forces onto Articulated Massless Legs

In order to make the LASLIP torso COM track the SLIP COM path, the hip, knee and ankle torques of the articulated legs of the LASLIP model satisfy the emulation equations shown below.

$$\ddot{x}_L = \ddot{x}_S \tag{5.40}$$

$$\ddot{y}_L = \ddot{y}_S \tag{5.41}$$

$$\ddot{\theta}_L = \nu_\theta \tag{5.42}$$

As with the ASLIP model, a fourth equation is introduced during double stance to make

it possible to solve for a set of joint torques in this overactuated pose.

$$\frac{\tau^1_{L,1}}{f_{Ly,1}} - \frac{\tau^1_{L,2}}{f_{Ly,2}} = 0 \tag{5.43}$$

Several different mappings were developed because the topology of the model changes between single and double stance, and when the knee is locked (Fig. 5.5). Each leg can be in one of 4 different topological states: swing (S), underactuated stance with toe contact (Ut), fully actuated stance (F) and underactuated stance with heel contact (Uh). Two legs thus have 16 different state combinations they can be in, though only 5 are used during walking (Fig. 5.5). The mappings required to emulate the ASLIP model are developed for each of these different topologies.

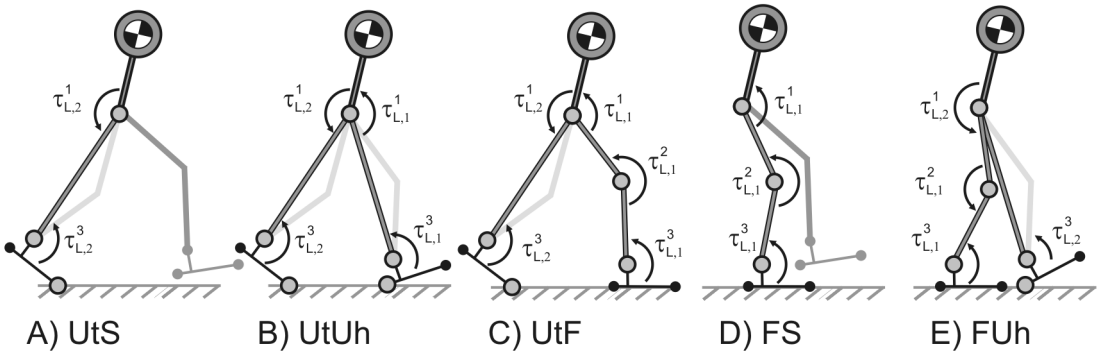

Figure 5.5: Relevant leg postures during walking. A different mapping to make the bipedal LASLIP emulate the bipedal ASLIP is required for each phase of gait. Capital letters indicate the state of the leg: 'U' indicates a leg is underactuated (foot is rotating about point), 'F' that the leg is fully actuated (foot is flat on the ground), and 'S' that the leg is in swing. When a leg is underactuated, the point the foot is rotating about is indicated with lower case letters: 't' for the toe, and 'h' for the heel

Mapping ASLIP hip forces and torques is most challenging during toe-off (UtS in Fig. 5.5A) because the model is underactuated. It may be possible to use the same approach employed by Poulakakis and Grizzle [79] to find a nonlinear transformation that embeds the dynamics of the SLIP in the LASLIP, though the size and complexity of the LASLIP equations of motion have thus far thwarted attempts to find such a transformation. For the present investigation, hip and ankle torques that satisfy Eqns. 5.40 and 5.42 are applied to the model, while Eqn. 5.41 is ignored.

The double stance pose (UtUh in Fig. 5.5B) where both feet are contacting the ground at points has two hip torques and two ankle torques as control inputs. The three SLIP emulation equations (Eqns. 5.40,5.41 and 5.42) and the fourth hip torque sharing equation (5.43) can be solved to yield an analytical solution for each torque required.

The mapping for an over-actuated double-stance (UtF in Fig. 5.5C) does not have a unique solution because there are five actuated joints, and the model has only three degrees of freedom. For the purposes of this investigation, a two-stage mapping is used: the torque that is applied to one of the ankles is first computed, then the three SLIP emulation equations and the extra hip torque sharing equation are used to solve for the remaining knee, ankle and two hip torques. The ankle torque of the foot which is flat on the ground (the foot to the right in Fig. 5.5C) is calculated by solving the three SLIP emulation equations as if the other leg, which is in push-off, is in swing.

The hip, knee and ankle torques during mid-stance (FS in Fig.5.5D) are most easily mapped using the SLIP emulation equations because there are 3 joint torques to solve 3 emulation equations (Eqn. 5.40-5.42). This set of equations can be solved analytically, though the solution is too large to be included in this manuscript (solved using MapleSim [60].

During slow walking, it is possible that the lead heel contacts the ground before the stance limb moves into toe-off (FUh in Fig. 5.5E). This yields an over-actuated system that is similar to the over-actuated double stance with toe-off previously discussed. The same two-stage mapping that was described for the previous over-actuated state (UtF) was used for this phase of gait.

5.4.4 LASLIP Mapping Evaluation via Simulation

The bipedal LASLIP and SLIP models were simulated for comparison purposes using exactly the same parameters used for bipedal ASLIP simulation (Sec. 5.3). The lengths of the thigh and leg ($L_1 = 48cm$, $L_2 = 48cm$) were found using anthropometric tables [110]. The foot geometry was estimated ($AnkleY = 6.8cm$, $HeelX = 6.8cm$ and $ToeX = 13.7cm$), as no suitable anthropometric table of the foot could be found. The knee angle during swing, β_{SW}, was set to $-12°$, the angle a human knee reaches when the foot flattens on the floor [109] during early stance. The minimum knee angle, β_{MIN}, was set to $-1°$ to avoid a singularity that occurs in Eqns. 5.37- 5.38 when the knee is straight ($\beta = 0$).

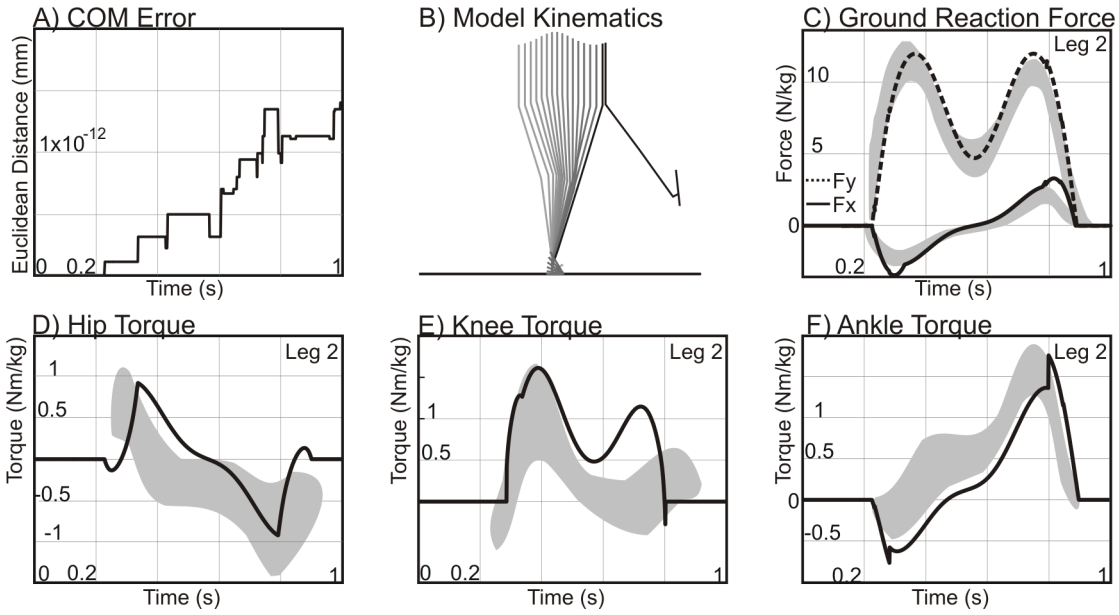

Figure 5.6: Simulation results of the LASLIP. The Euclidean distance between the COM of a bipedal SLIP and LASLIP model is shown in panel A). Panel B) shows an illustration of the kinematics of the gait of the LASLIP. The ground reaction force profiles beneath leg 2 are shown in panel C) with human ground reaction force envelope covering ± 1 standard deviation [109] shown in gray. Panels D), E) and F) show the hip, knee and ankle torques of the LASLIP in black with the corresponding human torque envelopes covering ± 1 standard deviation shown in gray

The simulation results show that the torso tracking control system drove the COM kinematics of the SLIP and the LASLIP model to match to a very high precision (Fig. 5.6A) and regulate the torso orientation very precisely (average error of -1×10^{-16} radians). The LASLIP has retained the characteristic human-like ground reaction forces of the SLIP model (Fig. 5.6C), though with some small cusps at the moment the model makes the transition from single to double stance. Further examination reveals that the hip, knee and ankle torques of the LASLIP model are similar to estimated human hip, knee and ankle torques [109]. The discontinuities present in the LASLIP joint torque profiles are due to the changes in stance limb topology when the knee locks. The phase and magnitude differences between the LASLIP torque curves and the human joint torque curves are likely caused by the large model differences between a full human model and the simplified LASLIP model.

The quality of match between the LASLIP joint torques and human data (Fig. 5.6) is very

encouraging, and indicates that a partitioned approach to predicting human kinematics and kinetics is worthy of further study. The LASLIP also indicates that it is very important to carefully define how the load is shared between the two legs during double stance. Although it was possible to define double stance heuristics (Eqn. 5.43 and those detailed in Sec. 5.4.3) that produced good results, it is highly unlikely that these heuristics will work well in all situations.

5.5 Mapping SLIP Torso Dynamics onto an Anthropomorphic Multibody Gait Model

An 11-dof anthropomorphic gait model (Fig. 5.7) actuated by joint torques calculated from a torso-tracking controller was developed to apply the proposed partitioned simulation approach to a more realistic model. Joint coordinates were used at the knee, ankle and midfoot joints, while the hips were modeled using position constraints to ensure that the contact force at the hip joint — a required quantity by the torso tracking control system — would be a part of the system equations of the model. The model is controlled using 6 joint torques applied at both hips, knees and ankles. The model interacts with the ground using the foot contact model detailed in Ch. 4 consisting of two spherical volumetric contact elements [31] to represent the heel and metatarsal pads. The midfoot is not rigid, but is allowed to flex slightly at a revolute joint that has a spring damper in parallel with it.

Several control laws were developed to calculate the joint torques required to satisfy the emulation equations for this model, listed below. The viscoelastic foot pads used in the multibody model makes it impossible [17] to apply input-output feedback linearization to this model. Instead, an input-output feedback linearization control law is calculated for an approximate model (detailed in Sec. 5.5.1) which has a simplified foot. Since the control model is an approximation of the gait model, feedback control — supplied by the error terms (ν_x,ν_y and ν_θ) — is necessary to ensure that the orientation of the torso is regulated and its position converges with the COM location of the SLIP model.

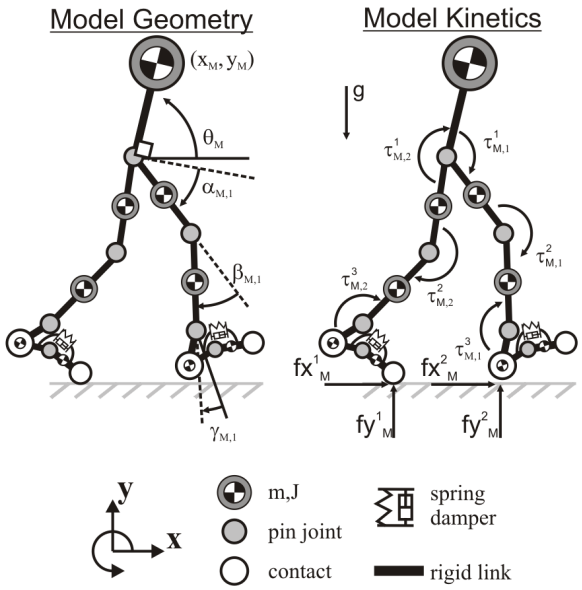

Figure 5.7: The multibody model

$$\ddot{x}_M = \ddot{x}_S + \nu_x \tag{5.44}$$

$$\ddot{y}_M = \ddot{y}_S + \nu_y \tag{5.45}$$

$$\ddot{\theta}_M = \nu_\theta \tag{5.46}$$

Hip, knee and ankle torques that satisfy Eqns. 5.44-5.46 are computed for the multibody gait model using a series of control models (Fig. 5.8) that have a simplified foot, making it possible to use input-output feedback linearization [44]. As with the LASLIP model, a set of three additional heuristic equations are introduced during double stance to permit a unique set of joint torques to be computed to satisfy Eqns. 5.44-5.46 in this overactuated pose (here the torso has 3 dof, and there are 6 joint torques that can be applied).

Since the legs now have mass (in contrast to the previous models) a swing controller is required to guide the leg from its final push-off position to its contact position in a specific amount of time. The SLIP model is used to precompute the swing length (Δ_X) and time since only constant cadence walking is being considered. Guiding the leg from push-off to heel-contact in a set amount of time, in a manner that requires modest torque magnitudes,

and keeps the foot from scuffing the ground is a formidable two-point boundary value problem. A traditional optimal control approach used in robotics [94] was used to find a swing trajectory with these properties. This pre-computed swing trajectory was used as a reference for a computed-torque controller to guide the swing limb on the multibody model. The following subsections detail the approach that was used to control the model during stance (Sec. 5.5.1) and swing (Sec. 5.5.3).

5.5.1 Single Stance Control

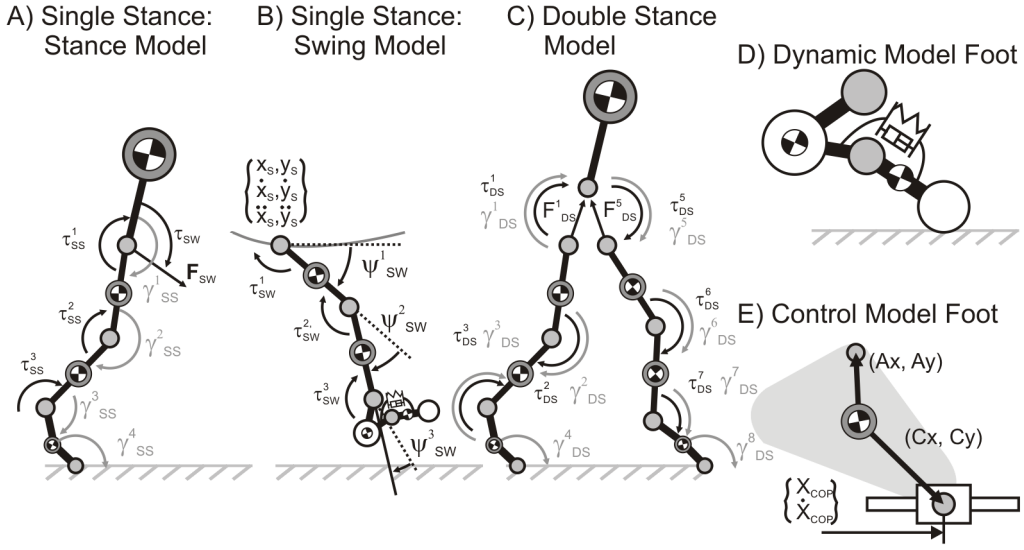

Figure 5.8: The stance model A), the swing model B) and the double stance model C) used by the control system to compute the hip, knee and ankle torques. The actual foot contact model consists of a 2-part model that includes volumetric foot contact pads D), while the abstraction used by the control system treats the foot as a rigid link that rotates about a pin joint that is translating along a prismatic joint E)

While the importance of modeling the compliance of the human foot accurately has been noted by many in the gait modeling research community [5, 1, 65], a flexible and compliant foot complicates the control of the torso substantially. There is little information available in the literature on controlling bipeds that interact with the ground using a compliant foot. The compliance of the foot limits the forces that the leg can apply to the torso. The heel

pad load cycles (Fig. 4.3 of Ch. 4) suggest that human foot pads behave like nonlinear springs between the bones of the foot and the ground. When the foot pads are touching the ground, but have not reached steady state compression, the foot pads behave like a spring of low stiffness. The transient low stiffness of the foot pads greatly limits the ability of the leg to apply a desirable force and torque to the hip joint. As the pads of the foot compress, their apparent stiffness significantly increases and can be approximated as being rigid giving the leg greater control authority over the torso. While a compliant foot is used for the dynamic model (Fig. 5.8.D), a geometrically equivalent but rigid foot is used for the control model (Fig. 5.8.E). During the transient contact phase when the apparent stiffness of the foot pads is quite low, the control model and the dynamic model differ. The two models are made to converge to one and other as the foot pads reach steady state compression by using feed-back control to augment the desired torso accelerations (Eqns. 5.44- 5.46). Each of the feedback error terms (ν_x,ν_y and ν_θ) take the form of a state feedback PD controller:

$$\nu_x = -K_x(x_M - x_S) - D_x(\dot{x}_M - \dot{x}_S) \tag{5.47}$$

$$\nu_y = -K_y(y_M - y_S) - D_y(\dot{y}_M - \dot{y}_S) \tag{5.48}$$

$$\nu_\theta = -K_\theta(\theta_M - \theta_0) - D_\theta(\dot{\theta}_M) \tag{5.49}$$

Input-output feedback linearization [44] is used to compute the hip, knee, and ankle torques required to accelerate the torso of the multibody model such that Eqns. 5.44-5.46 are satisfied. The input-output feedback linearization control expressions are not formulated using the multibody model (Fig. 5.7) — due to the difficulties the full foot model introduces — but with an approximate single stance model (Fig. 5.8A) that includes a simplified foot. To form the control law, we first begin with the equations of motion of the stance control model (Fig. 5.8A) in functional form (using square brackets to denote matrices).

$$\ddot{\vec{\gamma}}_{SS} = [M_{SS}]^{-1}_{4\times4}\left(-\vec{C}_{SS} + [P_{SS}]_{4\times3}\{\vec{\tau}_{SS}\}_{3\times1} + [Q_{SS}]_{4\times3}\left\{\begin{array}{c}\vec{F}_{SW}\\ \vec{\tau}_{SW}\end{array}\right\}_{3\times1}\right) \tag{5.50}$$

In Eqn. 5.50 $\vec{\gamma}_{SS}$ is the vector of joint angles (and respective derivatives) of the single

stance (SS) control model (Fig. 5.8A), $[M_{SS}]$ is the mass matrix, $\vec{C}_{SS}$ the vector of Coriolis, centripetal and gravitational forces; $[P_{SS}]_{4\times3}$ is the matrix that transforms the joint torques $\{\vec{\tau}_{SS}\}_{3\times1}$ into generalized forces; and $[Q_{SS}]_{4\times3}$ is the matrix that transforms the reaction force, and vector $\left\{\vec{F}_{SW}, \vec{\tau}_{SW}\right\}_{3\times1}$ that the swing limb applies to the pelvis into generalized forces. The variables used to describe the general multibody terms in Eqn. 5.50 are used throughout this chapter. The accelerations of the torso $(\ddot{x}_M, \ddot{y}_M, \ddot{\theta}_M)$ can be expressed as a linear combination of the joint accelerations of the stance model. After substituting the Eqns. 5.44-5.45, the SLIP emulation equations, the mapping from the accelerations of the torso to the angular accelerations of the joints of the leg becomes:

$$\begin{Bmatrix} \ddot{x}_S + \nu_x \\ \ddot{y}_S + \nu_y \\ \ddot{\theta}_S + \nu_\theta \end{Bmatrix} = [T_{SS}]_{3\times4} \left\{\ddot{\vec{\gamma}}_{SS}\right\} \tag{5.51}$$

Substituting Eqn. 5.50 into Eqn. 5.51 yields a set of three equations that is linear in the three joint torques $\vec{\tau}_{SS}$.

$$\begin{Bmatrix} \ddot{x}_S + \nu_x \\ \ddot{y}_S + \nu_y \\ \ddot{\theta}_S + \nu_\theta \end{Bmatrix} = [T_{SS}]_{3\times4} [M_{SS}]^{-1}_{4\times4} \left(-\vec{C}_{SS} + [P_{SS}]_{4\times3} \{\vec{\tau}_{SS}\}_{3\times1} + [Q_{SS}]_{4\times3} \begin{Bmatrix} \vec{F}_{SW} \\ \vec{\tau}_{SW} \end{Bmatrix}_{3\times1} \right) \tag{5.52}$$

Once the state of the multibody model has been mapped to an equivalent state of the stance model, Eqn. 5.52 becomes a system of three equations with three unknowns (the three components of $\vec{\tau}_{SS}$) making it possible to compute values of the hip, knee and ankle torques that will satisfy Eqns. 5.44-5.46. The hip, knee and ankle states can be mapped directly from the multibody model to the stance control model.

$$\gamma_{SS}^{1} = -(\theta_M - \frac{\pi}{2} + \alpha_M) \quad (5.53)$$

$$\gamma_{SS}^{2} = -\beta_M \quad (5.54)$$

$$\gamma_{SS}^{3} = -\gamma_M \quad (5.55)$$

$$\dot{\gamma}_{SS}^{1} = -(\dot{\theta}_M + \dot{\alpha}_M \quad (5.56)$$

$$\dot{\gamma}_{SS}^{2} = -\dot{\beta}_M \quad (5.57)$$

$$\dot{\gamma}_{SS}^{3} = -\dot{\gamma}_M \quad (5.58)$$

The geometry of the foot of the control model (Fig. 5.8A) — the length of the link between the COM of the foot and the revolute joint attached to the ground — is adjusted so that the revolute joint that attaches to the ground at a location that coincides with the COP of the foot of the multibody model (Fig. 5.7). The angular velocity of the stance model foot, and the translational velocity of the COP of the stance model ($\dot{\gamma}_{SS}^{4}$ in Fig. 5.8A and $\dot{x}_{COP}$ in Fig. 5.8E) are computed such that the translational velocity of the ankle joints of the stance control and multibody gait model match.

5.5.2 Double Stance Control

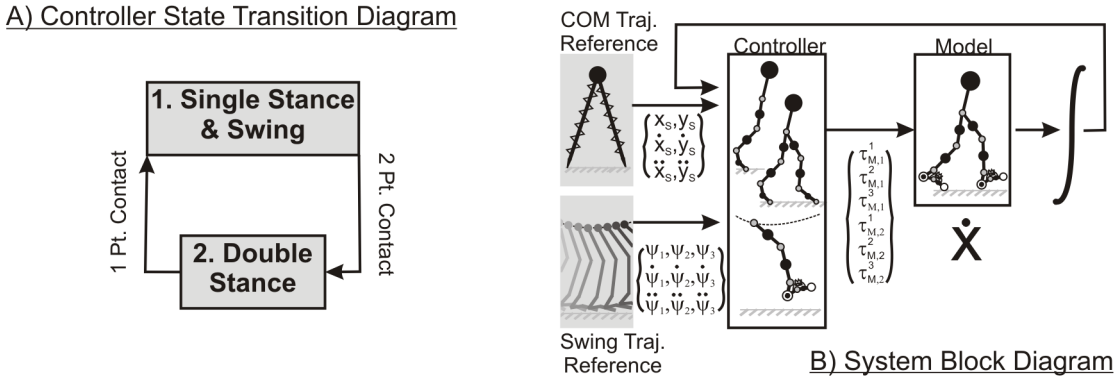

Figure 5.9: The single and double stance control models are switched as a function of foot contact A). The gait model is controlled by the multibody swing and stance models which use the SLIP and swing reference kinematics as desirable trajectories B)

Once the swing foot comes into contact with the ground, the controller changes its internal state from single stance to double stance (Fig. 5.9), and employs a completely different control model (Fig. 5.8C), for which a new control law must be derived. As before, input-output feedback linearization is applied to an approximate double stance model to yield hip, knee and ankle torques for both legs that will satisfy Eqns. 5.44-5.46. The derivation begins by computing the net force and torque that the two legs must apply to the torso to satisfy Eqns. 5.44-5.46.

$$f_{Mx} = m(\ddot{x}_M + \nu_x) \tag{5.59}$$
$$f_{My} = m(\ddot{y}_M + \nu_y + g) \tag{5.60}$$
$$\tau_M = J\nu_\theta - L(f_{Mx}\sin(\theta_M) - f_{My}\cos(\theta_M)) \tag{5.61}$$

Where f_{Mx},f_{My}, and τ_M are the net force and torque that the two legs must apply to the torso (of mass m, inertia J at an orientation of θ_M as before) to satisfy Eqns. 5.44-5.46. The net force and torque applied to the torso is simply the sum of the force and torque that each leg applies to the hip joint.

$$f_{Mx} = (\vec{F}^1_{DS} + \vec{F}^5_{DS}) \cdot \hat{\imath} \tag{5.62}$$
$$f_{My} = (\vec{F}^1_{DS} + \vec{F}^5_{DS}) \cdot \hat{\jmath} \tag{5.63}$$
$$\tau_M = \tau^1_{DS} + \tau^5_{DS} \tag{5.64}$$

Since the net force and torque that is applied to the torso is only comprised of three variables, yet is a function of six joint torques (τ^{1-3}_{DS} and τ^{5-7}_{DS}), there is no unique solution to this system of equations. As before with the LASLIP model, extra heuristic equations are introduced to divide the load between the two legs in proportion to the contact force beneath the respective foot of the multibody model.

$$\frac{\vec{F}^1_{DS}\cdot\hat{\imath}}{fy^1_M}+\frac{\vec{F}^5_{DS}\cdot\hat{\imath}}{fy^2_M} = 0 \tag{5.65}$$

$$\frac{\vec{F}^1_{DS}\cdot\hat{\jmath}}{fy^1_M}-\frac{\vec{F}^5_{DS}\cdot\hat{\jmath}}{fy^2_M} = 0 \tag{5.66}$$

$$\frac{\tau^1_{DS}}{fy^1_M}-\frac{\tau^5_{DS}}{fy^2_M} = 0 \tag{5.67}$$

The system of six equations (Eqns. 5.62-5.64 and Eqns. 5.65-5.67) can be solved for the forces and torques that each leg must apply to hip joint of the torso to satisfy Eqns. 5.59-5.61 and Eqns. 5.62-5.64. The force and torque that each leg applies to the hip joint of the torso can be used in combination with the equations of motion of the double stance model (Fig. 5.8C) to compute the remaining knee and ankle torques that each leg must generate. The equations of motion of the double stance model in functional form are

$$[M_{DS}]_{9\times9}\left\{\ddot{\vec{\gamma}}_{DS}\right\}+\vec{C}_{DS}+\left\{\begin{array}{c}0_{5\times1}\\ \hline \vec{\lambda}_{4\times1}\end{array}\right\}^T\left\{\begin{array}{c}0_{5\times1}\\ \hline \vec{D}_{DS,4\times1}\end{array}\right\}=[P_{DS}]_{9\times6}\left\{\vec{\tau}_{DS}\right\}_{6\times1} \tag{5.68}$$

Position constraint equations $\vec{D}_{DS}$ have been used to model the hip joints (rather than using joint coordinates) to make it possible to solve for the force that the legs apply at this joint. The reaction force at the hip can now be expressed as

$$\left\{\begin{array}{c}\vec{F}^1_{DS}\\ \vec{F}^5_{DS}\end{array}\right\}_{4\times1}=[B_{DS}]_{4\times4}\left\{\vec{\lambda}_{4\times1}\right\} \tag{5.69}$$

where matrix $[B]_{4\times4}$ is a matrix that transform the Lagrange multipliers into reaction forces. After solving Eqn. 5.69 for the Lagrange multipliers that yield the desired joint reaction forces and substituting the result into Eqn. 5.68 we have

$$[M_{DS}]_{9\times 9}\left\{\ddot{\vec{\gamma}}_{DS}\right\} + \vec{C}_{DS} + \left\{\begin{array}{c} 0_{5\times 1} \\ \hline [B_{DS}]^{-1}\left\{\begin{array}{c}\vec{F}^{1}_{DS} \\ \vec{F}^{5}_{DS}\end{array}\right\}_{4\times 1}\end{array}\right\}^{T}\left\{\begin{array}{c} 0_{5\times 1} \\ \hline \vec{D}_{DS,4\times 1}\end{array}\right\} = [P_{DS}]_{9\times 6}\left\{\vec{\tau}_{DS}\right\}_{6\times 1} \tag{5.70}$$

Since the two hip torques (τ^1_{DS} and τ^5_{DS}) and forces (f^1_{DS} and f^5_{DS}) are known from the solution to Eqns. 5.62-5.64 and Eqns. 5.65-5.67, Eqn. 5.70 has embedded in it a set of four equations (the constraint equations) that are linear in four unknowns (τ^2_{DS}, τ^3_{DS}, τ^6_{DS}, and τ^7_{DS}). After the state of the multibody model (Fig. 5.7) is mapped to the equivalent state of the double stance control model (Fig. 5.8) — using the same procedure detailed in Sec. 5.5.1 — Eqn. 5.69 can be solved for the remaining knee and ankle torques required to satisfy Eqns. 5.59-5.61.

5.5.3 Swing Control

The swing phase has been a topic of robotics research for many years and has resulted in a number of standard approaches: active trajectory tracking [39, 105], passive swing [62, 111], and a combination of passive and active swing techniques [81]. Although a lot of research has been done on the topic of swing, little of it is directly applicable to simulating a human swing phase. A purely passive swing is quite limiting because the swing frequency of the limb is fixed by the geometrical and inertial properties of the limb. In addition, it has been shown that a purely passive swing is incompatible with the human swing phase [107]. A purely trajectory driven approach is convenient, however, great care must be taken to choose a trajectory that does not require joint torques that would be impossible for a human to generate. Beginning the swing phase passively and finishing with trajectory tracking [81] seems ideal, though care must be taken to blend the two phases in a manner that does not cause torque transients.

For this preliminary investigation, optimization was used to pre-compute a human-like swing trajectory. During the multibody simulation, the swing limb was driven to follow the pre-computed optimal swing trajectory using a computed torque controller with feedback. Human-like swing kinematics that fit the swing phase of the target SLIP model were found by searching for a trajectory that minimized a convex function of joint work for the

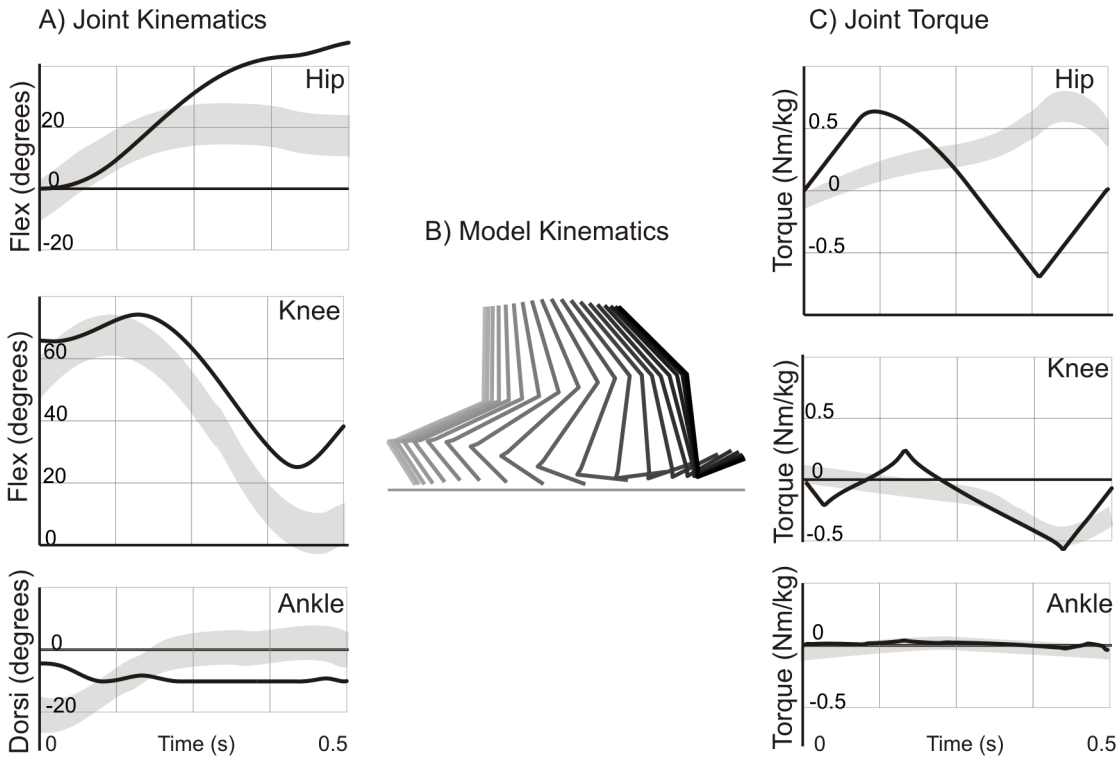

Figure 5.10: Swing phase simulation results. Model and human joint kinematics (in gray) are shown in A), a stick figure diagram is presented in B) and plots of model and human joint torques (in gray) are shown in C). Human data [109] is presented as a gray band that encompasses ±1 s.d.

swing model (Fig. 5.8B). A convex function of joint work was employed to crudely emulate the increased metabolic cost of eccentric and concentric contractions relative to isometric contractions [91]. Note that the joint angles of the swing model are represented using the variables ψ^1_{SW},ψ^2_{SW},ψ^3_{SW} in the place of α_M,β_M and γ_M for convenience.

$$min \sum_{i=1}^{3} \int_{t0}^{tf} (\tau^i_{SW} \dot{\psi}^i_{SW})^2 dt \tag{5.71}$$

Unlike the stance model, bandwidth-limited joint torque actuators were used during the optimization process. It was critical to use bandwidth-limited joint torque actuators to prevent the optimization algorithm from converging on a solution that required sharp

changes of joint torque outside of human capabilities. Each torque actuator was modeled as having a second-order, critically damped ($\zeta = 1$, $\omega_N = 8Hz \times 2\pi\, rad$) impulse response to a torque demand μ^i to crudely approximate the behavior of an equivalent set of muscles [110].

$$\ddot{\tau}^i = \omega_N^2 \mu^i - 2\zeta\omega_N \dot{\tau}^i - \omega_N \tau^i \tag{5.72}$$

Direct collocation [86] was used to solve this constrained problem to find solutions that satisfied the equations of motion,

$$[M_{SW}]_{3\times3} \left\{ \ddot{\vec{\psi}}_{SW} \right\} + \vec{C}_{SW} = [P_{SW}]_{3\times3} \{\vec{\tau}_{SW}\}_{3\times1} \tag{5.73}$$

prevented the heel and toe from touching the ground during the swing period,

$$\left\{ \begin{array}{c} y_{HEEL} \\ y_{TOE} \end{array} \right\} > 0 \tag{5.74}$$

and finished with the heel at the desired contact location.

$$\left\{ \begin{array}{c} x_{HEEL} \\ y_{HEEL} \end{array} \right\} = \left\{ \begin{array}{c} \Delta_X \\ 0 \end{array} \right\} \tag{5.75}$$

The accelerations of the hip, required in Eqn. 5.73, were set to the vertical and horizontal accelerations of the SLIP model.

The kinematics and torques of the minimal joint work swing trajectory reveal differences from human swing (Fig. 5.10). Although the hip and knee initial positions are very similar, the final position of the model requires more flexion at the hip and knee than is typical of a human swing [109]. The hip torque of the model is markedly different from human hip torques [109] (estimated using inverse dynamics analysis), taking on a sinusoidal form. These differences are likely due to both model differences — none of the passive muscle properties are being modeled — and cost function differences. For the present study this plausible, but clearly un-human swing trajectory will be used to guide the swing leg to its final position at heel contact.

Once the swing trajectory was established, the swing limb was controlled to follow this trajectory using a standard computed torque controller [94] as shown in Eqn. 5.76.

$$\{\vec{\tau}_{SW}\}_{3\times1} = [P_{SW}]^{-1}_{3\times3}\left([M_{SW}]_{3\times3}\left\{\ddot{\vec{\psi}}^{*}_{SW}\right\} + \vec{C}_{SW}\right) \tag{5.76}$$

Since the actual hip acceleration of the multibody model may differ from the desired vertical and horizontal accelerations of the target SLIP model, the state feedback controller shown in Eqn. 5.77 was used to ensure that the swing limb would converge to its desired trajectory over time.

$$\begin{Bmatrix} \ddot{\psi}^{*1}_{SW} \\ \ddot{\psi}^{*2}_{SW} \\ \ddot{\psi}^{*3}_{SW} \end{Bmatrix} = \begin{Bmatrix} \ddot{\psi}^{1}_{SW} \\ \ddot{\psi}^{2}_{SW} \\ \ddot{\psi}^{3}_{SW} \end{Bmatrix} - K_{SW}\begin{Bmatrix} \alpha_M - \psi^{1}_{SW} \\ \beta_M - \psi^{2}_{SW} \\ \gamma_M - \psi^{3}_{SW} \end{Bmatrix} - D_{SW}\begin{Bmatrix} \dot{\alpha}_M - \dot{\psi}^{1}_{SW} \\ \dot{\beta}_M - \dot{\psi}^{2}_{SW} \\ \dot{\gamma}_M - \dot{\psi}^{3}_{SW} \end{Bmatrix} \tag{5.77}$$

5.5.4 Multibody Control Mapping Evaluation via Simulation

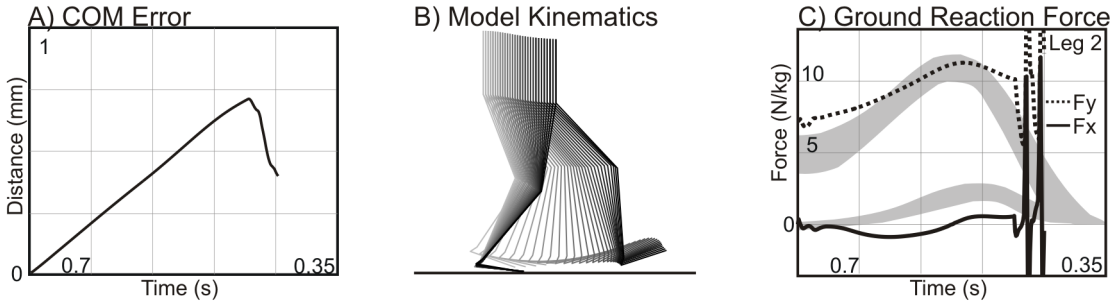

Figure 5.11: Multibody gait simulation results. SLIP tracking works very well during single stance but fails at the end of swing

The multibody model and control system was numerically simulated. At each timestep Eqns. 5.76 and 5.77 were used to apply torques to the hip, knee and ankle of the swing limb to ensure that it tracked the desired swing trajectory. The reaction force and torque, F_{SW} and τ_{SW}, that the swing limb applied to the hip joint, along with the desired torso accelerations from Eqns. 5.44-5.46 were substituted into Eqn. 5.52 prior to solving for the

stance limb control torques τ^1_{SS},τ^2_{SS} and τ^3_{SS} during single stance; and Eqn. 5.70 during double.

The simulation results (Fig. 5.10) indicate that the swing and stance controllers performed well, but problems were encountered during the transition between these phases. The stance controller limited the (Euclidean) distance error between the torso of the multibody model and the SLIP reference model to less than 1mm, though relatively high levels of feedback were required ($K_x = K_y = D_x = D_y = 10^3$ $\frac{N}{m}$ and $\frac{Ns}{m}$ respectively;$K_\theta = D_\theta = 10^4$ $\frac{Nm}{rad}$ and $\frac{Nms}{rad}$ respectively) to make the SLIP and the multibody torso trajectories converge. During this time, the stance foot moved from being flat on the ground to rotating about the toe smoothly. When the swing limb reached its final posture, the target accelerations $\ddot{\psi}^i_{M,W}$ and velocities $\dot{\psi}^i_{M,W}$ were set to zero. This sudden change in desired acceleration and velocity caused the swing controller of Eqn. 5.76 to apply large torques to the swing limb. These large control torques resulted in correspondingly large reaction forces at the hip joint, causing the stance controller to go unstable (Fig. 5.11). Double stance was never reached.

The failure of this control system highlights a fundamental challenge of controlling the state of the torso during stance, and then controlling the state of the leg during swing: blending these two different control paradigms smoothly is difficult. Since the state of the leg is not controlled during stance (the state of the torso is), the posture of the leg at the end of stance is not known a priori. The state feedback terms (Eqn. 5.77) in the present swing controller (Eqn. 5.76) compute large control torques if the state of the leg was different from the pre-computed swing trajectory. It is likely that similar spurious control torques would be observed during the transition from stance to swing.

5.6 Conclusions

Although SLIP models have human-like running and walking gaits, it is challenging to map this behavior to an anthropomorphic model. A bipedal extension of Poulakakis and Grizzle's ASLIP monopedal model and control laws was presented. The presented control laws for the bipedal ASLIP make its state equations identical to the bipedal SLIP model. The LASLIP model, an anthropomorphic extension to the bipedal ASLIP model, was presented along with preliminary work to map SLIP leg forces into the joint torque space

of the LASLIP. The LASLIP model regulated the orientation of its torso very effectively and closely tracked the trajectory of the target SLIP model (Fig. 5.6). The joint torque profiles of the LASLIP were similar in shape and magnitude to human joint torque profiles [109] estimated using inverse dynamics analysis, with the exception of a small discontinuity in the ankle torque profile. The LASLIP model indicates that the approach of partitioning the task of defining human-like kinematics and kinetics into two different models is worthy of further investigation, and in addition, that care must be taken when defining how the two legs are coordinated during double stance. Mapping the torso dynamics of the SLIP model onto the joint torque space of a full multibody sagittal plane model with simulated foot contact proved challenging. Although a new stance controller formulation was developed that functions smoothly when the stance foot transitions from multiple to single point contact, the transition from swing to stance (and likely vice-versa) resulted in large control torques, eventually causing the model to fall. Future work should concentrate on determining how best to coordinate the legs during double stance, and on developing controllers that allow the multibody model to emulate the SLIP while ensuring smooth transitions stance to swing.

Chapter 6

Discrete Planar Balance Corrections using Foot Placement

In Ch. 5 control systems that allowed several models to emulate a SLIP were developed, giving the anthropomorphic models the human-like gait of the SLIP [7, 26]. Similarly, the anthropomorphic models also inherit the limitations of the SLIP model that they are emulating. Although the SLIP can be made to run and walk with human-like COM and GRF profiles, it can only do so at a fixed cadence. While the SLIP model can maintain a very consistent gait, the control it has over its balance is poor because it cannot stop. Gait termination and compensatory stepping movements are of particular interest to kinesiologists and clinicians, because human use these types of movements to prevent falls. Clearly the simple model that the multibody model emulates needs to be able to catch its balance in a single step like a human [13].

Foot placement has long been recognized as the primary mechanism that humans use to restore balance [71]. While the continuous control of balance that occurs during stance is critical, as mentioned in Ch. 5, the chosen foot placement location is equally important because it determines the family of forces that the stance limb can apply to the torso. Many biomechanists have examined where humans place their feet during gait, perturbations, and during athletic events. Roboticists have also used foot placement as a means of control, but with limited success. Recently Wight et al. introduced a planar foot placement estimator (FPE) algorithm that will *restore* balance to a simplified biped that is falling. In this chapter, the 2D FPE is explained and tested as a candidate function for sagittal-plane

human-foot-placement (HFP). The kinematics of 14 healthy subjects while they performed 10 walking trials at three paces were recorded in order to calculate the FPE and compare it to HFP locations at heel contact.

People might not step on the location calculated by the FPE for a variety of reasons. Wight et al. proved that a simplified biped becomes statically balanced in a single step if it steps directly on the FPE (Fig. 6.2c). Subjects might not step on the FPE because they do not behave like the simplified biped. A sensitivity analysis will be used to determine how closely humans behave like Wight et al.'s simplified biped. Subjects also may not step at the FPE location when they do not want to become statically balanced (Fig. 6.2).

While people may not always step on the FPE when walking, we expect they will place their feet in locations that allow them to stop within a single step. The simplified biped has a contact point (Fig. 6.1), whereas a human foot has a contact area giving people some flexibility about where they choose to place their feet. The center of pressure (COP) is the closest physical analogue to the simplified biped's contact point because, like the contact point, moments of the ground reactions about this location sum to zero. As long as the FPE lies within the contact area of the foot, the subject would be guaranteed of stopping by moving their COP on or ahead of the FPE (Fig. 6.2b). This constraint means that the FPE should fall behind the leading edge of the foot when forward motion is desired.

6.1 Model

Wight et al. developed the FPE to restore balance to a simplified biped (Fig 6.1) because more complicated bipeds — such as humans — have unmanageably large equations of motion. The biped consists of a single body with 3 degrees of freedom (planar translation and rotation), and two infinitely small contact points that represent feet attached to the body with rigid massless links. The FPE will calculate where the biped should place its contact point so that after impact it has just enough kinetic energy to transition to a standing position (Fig. 6.2c). The derivation for the final expression of the FPE for a simplified biped is shown below. It is assumed that angular momentum (H) is conserved during contact about the point of contact o (Fig. 6.1). The instant before contact is denoted with a subscript 1, the instant after contact with a subscript 2.

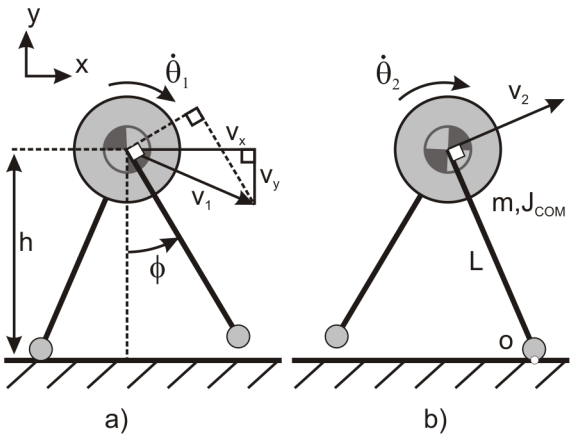

Figure 6.1: The simplified biped before and after foot contact, assuming the foot sticks to the ground and momentum is conserved [108]

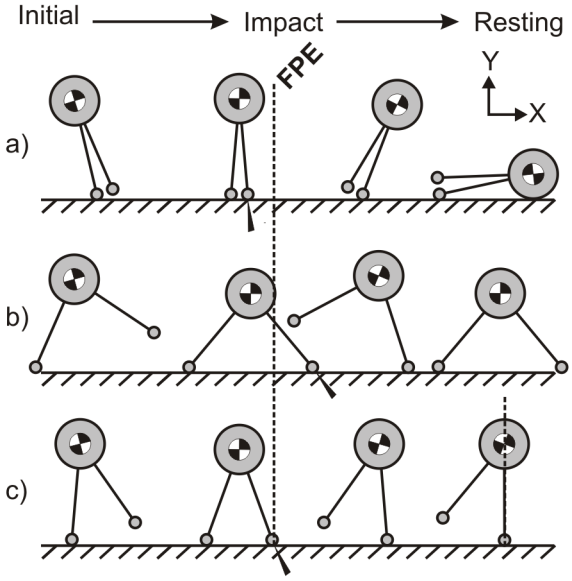

Figure 6.2: The simplified biped stepping relative to the FPE [108]. (a) Stepping closer than the FPE causes the biped to fall forward. (b) Stepping further than the FPE causes the biped to fall back onto the swing leg. (c) Stepping precisely at the FPE will perfectly balance the COM above the standing foot

$$Ho_1 = Ho_2 \tag{6.1}$$

The expression for planar angular momentum (using $s\phi,\ c\phi$ for $\sin\phi,\ \cos\phi$) can be expanded using the biped's mass (m), moment of inertia about the system COM (J_{com}), leg length (L) and its current COM linear (v_x,v_y) and angular ($\dot{\theta}$) speed.

$$mL(v_x\, c\phi + v_y\, s\phi) + J_{com}\, \dot{\theta}_1 \quad = \quad (mL^2 + J_{com})\, \dot{\theta}_2 \tag{6.2}$$

Whole-body average angular speed ($\dot{\theta}_1$ above) is calculated using the equivalent momentum [20] of the tracked body segments.

$$\dot{\theta}_{Avg} = \frac{\sum_{i=1}^{n} J_i \dot{\theta}_i}{\sum_{i=1}^{n} J_i} \tag{6.3}$$

Leg length is described in terms of the current height h to allow for variable leg lengths.

$$L = \frac{h}{c\phi} \tag{6.4}$$

Defining leg length (L) in this manner means that the FPE can find locations that might not be reachable by a human leg at a given moment in time. The post-impact angular speed of the biped $\dot{\theta}_2$ can be found by substituting Eqn. 6.4 into Eqn. 6.2.

$$\dot{\theta}_2 = \frac{mh(v_x\, c\phi + v_y\, s\phi)c\phi + J_{com}\, \dot{\theta}_1\, c^2\phi}{mh^2 + J_{com}\, c^2\phi} \tag{6.5}$$

The FPE is the contact location where the biped's post-contact system energy is equal to its peak potential energy. Peak potential energy is reached when the COM is at its maximum height (h_{peak}) with one contact point still on the ground. System energy refers to the sum of kinetic (T) and potential (V) energy.

$$T_2 + V_2 = mgh_{peak} \tag{6.6}$$

Since the simplified biped is in pure rotation after contact, Eqn. 6.6 becomes:

$$\frac{1}{2}(J_{com} + mL^2)\dot{\theta}_2^2 + mgL\, c\phi = mgL \tag{6.7}$$

Substituting Eqn. 6.5 into Eqn. 6.7 results in the nonlinear FPE equation to calculate ϕ, the angle at which the leg should be placed.

$$0 = \frac{[mh(v_x\, c\phi + v_y\, s\phi)c\phi + J_{com}\dot{\theta}_1\, c^2\phi]^2}{mh^2 + J_{com}\, c^2\phi} + 2mgh\, c\phi(c\phi - 1) \tag{6.8}$$

Simple trigonometry can be used to find $X(\phi)$, the location on the floor where the foot should be placed relative to the COM position.

$$X(\phi) = h\ \tan\phi \tag{6.9}$$

6.2 Experimental Methods

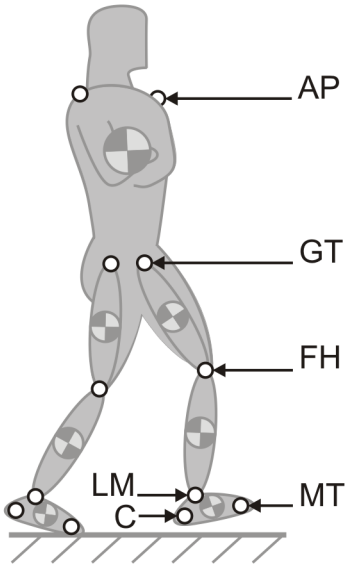

Figure 6.3: Sagittal plane marker layout

Fourteen healthy subjects (7 males and 7 females) with a wide range of heights (1.42 - 1.92m) and masses (69.5 - 114.5 kg) were instrumented with OptoTrak IRED markers to track the movements of 7 body segments (2 feet, shanks, legs and 1 lumped HAT) for 8 seconds at 200 Hz in the sagittal plane and record heel contact locations while they walked. IREDs were placed on the distal head of the 5^{th} metatarsal (MT), fibular trochlea of the calcaneus (C), the lateral malleolus (LM), the proximal fibular head (FH), the greater trochanter (GT) and the acromion process (AP). Subjects walked with their arms crossed (eliminating the need to track arm movements) through the (approximately) 5 m long collection volume for 10 trials at 80%, 100%, and 120% of their natural pace, using a metronome to cue step timing. Two trial types were recorded: constant cadence walking, and walking that included gait initiation and termination. Anthropometric tables [110] were used to estimate each of the 7 segment masses and inertias (2 feet, shanks, legs and 1 HAT). The FPE's prediction was compared to the subject's lateral malleolus location during contact onset. The difference between these two locations, ϵ_{LM}, was studied using a $14 \times 2 \times 3$ (subject by trial type by pace) repeated measures ANOVA. Contact was identified kinematically (Sec. 6.2.1) to allow a larger number of steps to be analyzed than could be done with a limited number of force plates.

At contact onset (t_C), the horizontal location of the lateral malleolus marker ($\overrightarrow{LM}(t_C) \cdot (\hat{x})$) was subtracted from $X(\phi)$ (Eqn. 6.9) to obtain the FPE-HFP error (ϵ_{LM}). Similarly, the flat-footed horizontal location of the 5^{th} metatarsal ($\overrightarrow{MT}(t_C) \cdot (\hat{x})$) was subtracted from the FPE (forming ϵ_{MT}) to determine if the FPE was ahead of the contact area of the foot. These differences are shown in Eqn. 6.10, where the letter 'A' has been used to replace marker identifiers LM and MT.

$$\begin{aligned} \epsilon_{LM} &= X(\phi(t_C)) - \overrightarrow{LM}(t_C) \cdot \hat{x} \\ \epsilon_{MT} &= X(\phi(t_C)) - \overrightarrow{MT}(t_C) \cdot \hat{x} \end{aligned} \tag{6.10}$$

The lateral malleolus was chosen as the reference point for analysis because of its ease of identification across subjects. Contact onset was used because it allowed a simultaneous measurement of human foot placement and the state of the body before it was affected by ground reaction forces.

6.2.1 Kinematically Identifying Contact Onset

Accurately measuring the time of contact onset using foot kinematics was challenging. Thresholding the height of the foot can only identify contact with an accuracy of 100 ms [48], which is too crude for the present study. Ground reaction forces develop very quickly during heel contact and affect the velocity of the foot. Different velocity signatures of contact onset were investigated: the vertical and horizontal speeds of the three markers on the foot, and the angular velocity of the foot.

Contact onset was identified using a combination of thresholding and velocity signature analysis. Heel-first contacts caused the horizontal speed of the LM marker to increase when the heel gripped the ground and pitched the foot forwards. Unfortunately, two subjects often contacted the ground flat-footed, eliminating the LM velocity signature. Flat-footed contacts could be identified by the large differences in the contact times estimated by the thresholding method [48] and the LM velocity signature. These two methods were used to measure foot contact time with a high temporal resolution and ignore steps where they disagreed.

A trial was collected with both kinematic and force plate data to validate the foot contact identification algorithm. The force plate measured the true time of contact onset when its vertical load exceeded twice the standard deviation ($\sigma = 2.11\,N$) of the resting noise of the plate. The kinematic contact time lagged the estimate of the force plate by $0 - 10\,ms$, at which time the load on the plate was between $2.86 - 16.3\,N$. The effect of the delay on the FPE-HFP error (ϵ_{LM}) was estimated by multiplying the FPE-HFP velocity ($\frac{d\,LM_x}{dt} - \frac{d\,X(\phi)}{dt}$) by the maximum $10\,ms$ time lag.

6.2.2 Validation of Assumptions

Violations of the assumptions of the FPE were quantified using a sensitivity analysis. The FPE makes four assumptions: that momentum is conserved during contact, and that the leg length, moment of inertia, and system energy (the sum of kinetic and potential energy) are constant after contact. Since the FPE is continuously differentiable it is possible to take partial derivatives of $X(\phi)$ of the FPE with respect to the quantities that are assumed to be constant. The change in angular momentum (ΔHo), leg length (ΔL), moment of inertia (ΔJ_{COM}) and kinetic and potential energy sum ($\Delta(T+V)$) was calculated between

foot contact and the time the COM passes over the lateral malleolus (Fig. 6.5) — the moment when Wight et al.'s simplified biped comes to rest when it steps on the FPE. The error of the FPE due to the observed violations was estimated by taking the product of the partial derivatives and the observed differences.

Examining the assumption that angular momentum is conserved during heel strike is difficult because the simplified biped has a fixed contact point whereas the human foot has a moving contact area. The center of pressure (COP) could be analyzed because it is the closest physical analogue to the contact point of the simplified biped. Calculating angular momentum about the COP (Eqn. 6.11) produces misleading results because the COP movement has a dramatic effect on the angular momentum profile.

$$\vec{H}o_{ref}(t) \;=\; \sum_{i=1}^{7} J_i\,\vec{\omega}_i(t) + (\vec{r}_i(t) - \vec{r}_{COP}) \times m_i(\vec{v}_i(t)) - \vec{v}_{COP}(t) \tag{6.11}$$

Since the magnitude of the $J_i\vec{\omega}_i$ terms of the angular momentum of the body are minimal [38], the cross product terms $(\vec{r}_i - \vec{r}_{COP}) \times m(\vec{v}_i - \vec{v}_{COP})$ dominate. In early stance the COP moves forward quickly, making the $(\vec{v}_i - \vec{v}_{COP})$ term small, resulting in small angular momentum values. The COP slows down in mid-stance making the cross product terms significantly larger, increasing the calculated angular momentum. The large variation in angular momentum is misleading because it is being caused by the movement of the COP, rather than the contact event.

A fixed point of reference is required to determine if angular momentum is conserved during foot contact. The ground projection of the LM at mid stance (when the COM is over the LM) was chosen as a reference point. This location was chosen because it approximates the final location of the COP if the person stopped as the simplified biped does. Whole body angular momentum was calculated by summing the angular momentum of each segment about its own COM ($J_i\vec{\omega}_i$) and then about the reference point $(\vec{r}_i - \vec{r}_{LMGP}) \times m_i(\vec{v}_i)$ as in Eqn. 6.12.

$$\vec{H}_{LMGP}(t) \;=\; \sum_{i=1}^{7} J_i\,\vec{\omega}_i(t) + (\vec{r}_i(t) - \vec{r}_{LMGP}) \times m_i(\vec{v}_i(t)) \tag{6.12}$$

Leg length was measured using the Euclidean distance between the whole body center of mass (COM) and the LM ground projection of the contacting foot to be consistent with Wight et al.'s FPE [108]:

$$L(t) = |\vec{r}_{COM}(t) - \vec{r}_{LM}(t)| \tag{6.13}$$

The moment of inertia of the body (J_{COM}) was calculated about the COM of the body using the parallel axis theorem:

$$J(t)_{com} = \sum_{i=1}^{7} J_i + m_i|\vec{r}_i(t) - \vec{r}_{COM}(t)|^2 \tag{6.14}$$

The sum of kinetic and potential energy was calculated for each segment as:

$$T(t) + V(t) = \sum_{i=1}^{7} \frac{1}{2} m_i|\vec{v}_i(t)|^2 + \frac{1}{2} J_i|\vec{\omega}_i(t)|^2 + m_i g h_i(t) \tag{6.15}$$

Changes in each of these quantities (ΔA), except angular momentum (Ho), were calculated by taking the maximum difference that occurred between foot contact and the time the COM of the body passed over the lead ankle.

$$\Delta A = max(A(t)) - min(A(t)) \tag{6.16}$$

Unlike the changes in the quantities listed above, the change in angular momentum (ΔH_{LMGP}) was calculated by taking a local maximum difference using its value at contact onset ($H_{LMGP}(t_C)$) as a reference. Contact onset must be used as a reference because the model assumes that angular momentum is conserved during contact. After contact, angular momentum is free to vary, and in the case of the model decreases to zero when the biped becomes balanced.

The required differentials were calculated numerically at the time of foot contact:

$$\frac{\partial X(\phi)}{\partial H_{LMGP}} = \frac{X(\phi,(1+\delta)H_{LMGP}) - X(\phi,H_{LMGP})}{\delta H_{LMGP}} \tag{6.17}$$

$$\frac{\partial X(\phi)}{\partial J_{COM}} = \frac{X(\phi,(1+\delta)J_{COM}) - X(\phi,J_{COM})}{\delta J_{COM}} \tag{6.18}$$

$$\frac{\partial X(\phi)}{\partial L} = \frac{X(\phi,(1+\delta)L) - X(\phi,L)}{\delta L} \tag{6.19}$$

$$\frac{\partial X(\phi)}{\partial (T+V)} = \frac{X(\phi,(1+\delta)(T+V)) - X(\phi,(T+V))}{\delta (T+V)} \tag{6.20}$$

Each partial derivative was assessed for numerical stability by calculating the relative error between each partial using progressively smaller values of δ (0.01, 0.001, and 0.0001). The largest discrepancy between any of the partial derivatives was a mere 0.37%, indicating that an appropriately small value of δ had been chosen for each partial derivative. These sensitivity equations can also be computed symbolically by taking a partial derivatives of Eqn. 6.8.

6.3 Results

The 4257 step locations recorded (on average just over 5 steps were recorded per trial) in this study are highly correlated with the predictions of the FPE ($\rho \geq 0.997$ in Tbl. 6.1). In addition, the standard deviation σ_{LM} of the FPE-HFP error (here we are using μ to indicate a mean, and σ to indicate a standard deviation) is much smaller than the stride length standard deviation, σ_{SL} (Tbl. 6.1), suggesting that the model is successfully capturing the important dynamics of the foot placement process. Subjects appear to place the leading edge of their foot *ahead* of the FPE during natural and slower paced walks (see $\mu(\epsilon_{MT})$ and $\sigma(\epsilon_{MT})$ in Tbl. 6.1), allowing them to stop without taking an extra step if they behave like Wight et al.'s inverted pendulum. Only 212 of the 4257 steps analyzed had the MT behind the FPE, with nearly half (95 steps) generated by subject 6 whose natural cadence was a brisk 112 steps per minute, far faster than the rest of the subjects (who averaged 100 ± 7.71 steps per minute). The remaining exceptional steps were generated by

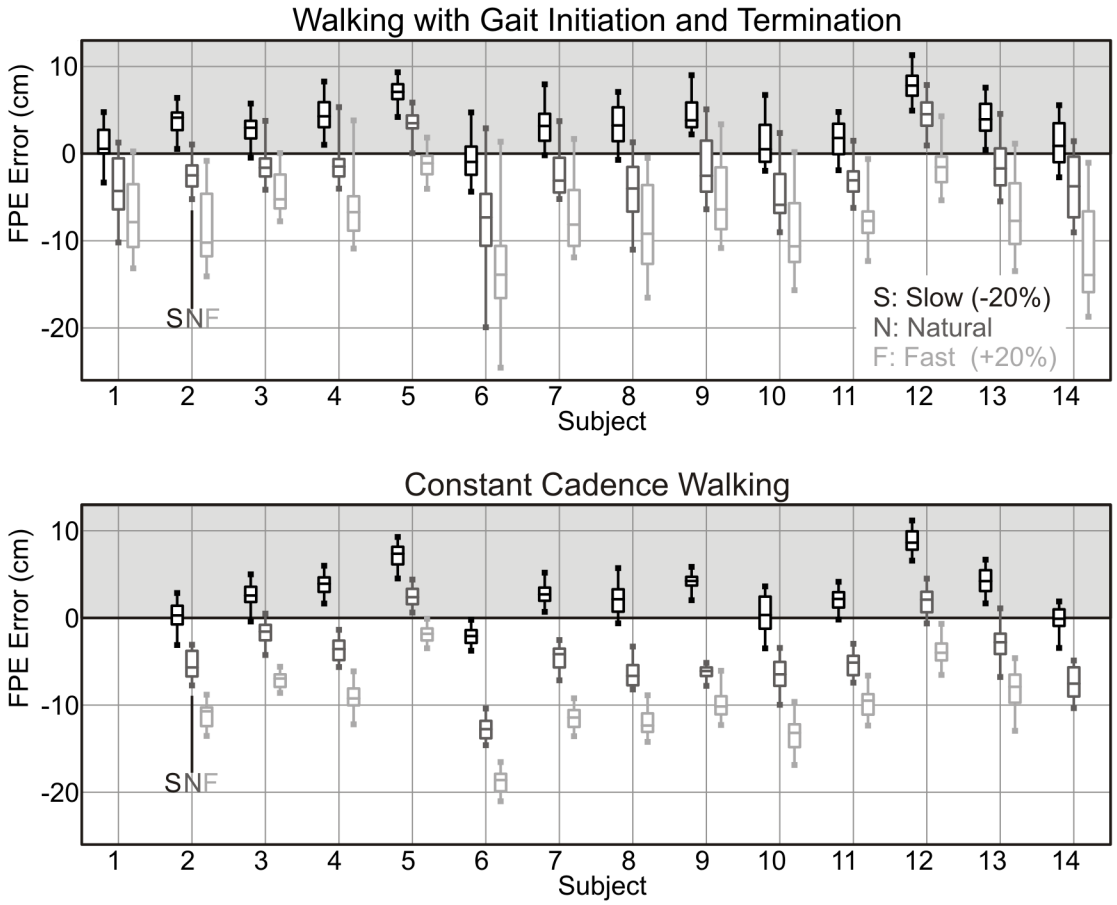

Figure 6.4: Box and whisker plots of the error between the FPE and each subject's lateral malleolus at foot contact. Whiskers run between the 5^{th} and 95^{th} percentiles, boxes between the 25^{th} and 75^{th} percentiles with a hash at the 50^{th} percentile. Natural paced trials align with the subject number; slow trials are immediately to the left and fast trials are to the right. Subjects are motivated by not only balance but pace and acceleration since they step further behind the FPE as they walk faster, and with more variation when they initiate and terminate gait. I failed to collect constant cadence trials for subject 1

other subjects during the fast paced trials (111 steps), with very few occurring in natural paced trials (4 steps).

	Init. and Term.			Cont. Walking		
	Slow	Nat.	Fast	Slow	Nat.	Fast
ρ	0.999	0.999	0.999	0.997	0.997	0.998
$\mu(\epsilon_{LM})$	3.27	-2.02	-6.85	2.57	-4.12	-8.28
$\sigma(\epsilon_{LM})$	2.40	3.18	4.43	1.60	1.50	1.45
σ_{SL}	7.36	10.5	17.6	2.96	2.73	2.15
$\mu(\epsilon_{MT})$	16.2	10.8	5.72	16.2	8.85	3.55
$\sigma(\epsilon_{MT})$	2.57	3.34	4.54	1.92	1.64	1.80

Table 6.1: The FPE and HFP are highly correlated (ρ). The FPE-HFP error means $\mu(\epsilon_{LM})$ and standard deviations $\sigma(\epsilon_{LM})$ change systematically with trial type and pace. The FPE is capturing important dynamics of the foot placement since FPE-HFP error standard deviations $\sigma(\epsilon_{LM})$ are much smaller than the stride length standard deviations σ_{SL}. The mean $\mu(\epsilon_{MT})$ and standard deviation $\sigma(\epsilon_{MT})$ of the distance between the FPE and the flat-footed position of the MT marker ϵ_{MT} indicate that subjects place their MT ahead of the FPE, allowing them to stop in a single step if desired. All quantities except ρ are in units of cm

The FPE-HFP (ϵ_{LM}) error appears to vary systematically for different walking paces (Fig. 6.4). The spread of the FPE-HFP error also appears to vary systematically between trials that included gait initiation and termination, compared to constant cadence trials (Fig. 6.4). A $12 \times 2 \times 3$ (subject by trial type by pace) repeated measures ANOVA analysis was used to study the apparent systematic changes of ϵ_{LM} in detail. The repeated measures ANOVA analysis was completed on the means of each subject, trial type, and pace combination using a subset of 20 ϵ_{LM} measurements per combination. The analysis found significant interaction between pace and trial type ($F(2, 22) = 18.82$, $p < 0.0001$). The strong interaction between trial type and pace indicates that subjects are coordinating their foot placements with both changes in pace and acceleration (constant velocity walking requires no acceleration, while the trial with gait initiation and termination does require acceleration). There are also significant main effects for trial type ($F(1, 11) = 50.52$, $p < 0.0001$), and pace ($F(2, 22) = 373.04$, $p < 0.0001$) though these main effects are not independent due to their significant interaction. These conclusions do not change if all ϵ_{LM} measurements are used to compute the subject, trial, and pace combination means used in the ANOVA analysis rather than a subset of 20 measurements per combination.

The data does not satisfy the assumptions of the ANOVA because only 49 out of 72 of the FPE-HFP error distributions are normal (using Kolmogorov-Smirnov, Cramer-Von Mises and Anderson-Darling tests), and the variances are not equal (using Levene's test). The findings should be unaffected by these assumption violations because the differences are so strong, and a repeated measures ANOVA is robust against such errors [90]. I failed to collect constant cadence walking trials for subject 1, and the fast constant cadence trial for subject 14. I chose to exclude the data of subject 1 and 14 in the analysis to permit a repeated measures ANOVA to be used for analysis.

W	$\frac{\partial X(\phi)}{\partial W} \pm \sigma$	$\Delta W \pm \sigma$	$\frac{\partial X(\phi)}{\partial W}\Delta W \pm \sigma$
H_o	0.27 ± 0.0046	7.31 ± 2.3	2.18 ± 0.64
J	-0.10 ± 0.0056	0.45 ± 0.036	-0.050 ± 0.0054
L	-0.077 ± 0.47	1.12 ± 0.13	-0.11 ± 0.016
T+V	1.25e-4 ± 7.49e-6	15.33 ± 7.25	0.21 ± 0.097
$\frac{d\epsilon_{LM}}{dt}$	-35.6 ± 5.52 $\frac{cm}{s}$	Δt_{max} 0.010	-0.36 ± 0.06
		$\Delta\epsilon_{LM} \pm \sigma$	-2.20 ±0.96

Table 6.2: The sensitivity analysis summary statistics indicate that violating the assumption of conservation of momentum could affect the FPE calculation by 2.18 *cm* on average, which cannot account for the observed -2.2 *cm* FPE-HFP error. The small changes in leg length, inertia and system energy would only influence the FPE-HFP error on the order of millimeters or less. All quantities in the final column are in units of *cm*

The velocity-dependent changes of the FPE-HFP error could be caused by a systematic violation of the assumptions of the FPE as described in Section 6.2. Most of the assumptions of Wight et al.'s model are met (Fig. 6.5), and affect the FPE calculation and the FPE-HFP error very little (Tbl. 6.2). In addition, the temporal error of the kinematic contact estimation technique could have affected the results only by $3.6 \pm 0.6\,mm$ (Tbl. 6.2). The assumption that angular momentum ($\vec{Ho}$) is conserved during contact is broken; angular momentum actually increases, due to a coordinated weight acceptance and push-off phase [16]. When the extra momentum is taken into account, the FPE predicts that the subjects should have stepped $2-3\,cm$ further ahead (Tbl. 6.2 and Tbl. 6.3), when in reality they stepped further behind the FPE as they walked faster. Based on the data and the analysis of the assumptions of the model we suggest that the velocity-dependent FPE-HFP error is volitional rather than being the result of a systematic violation of the

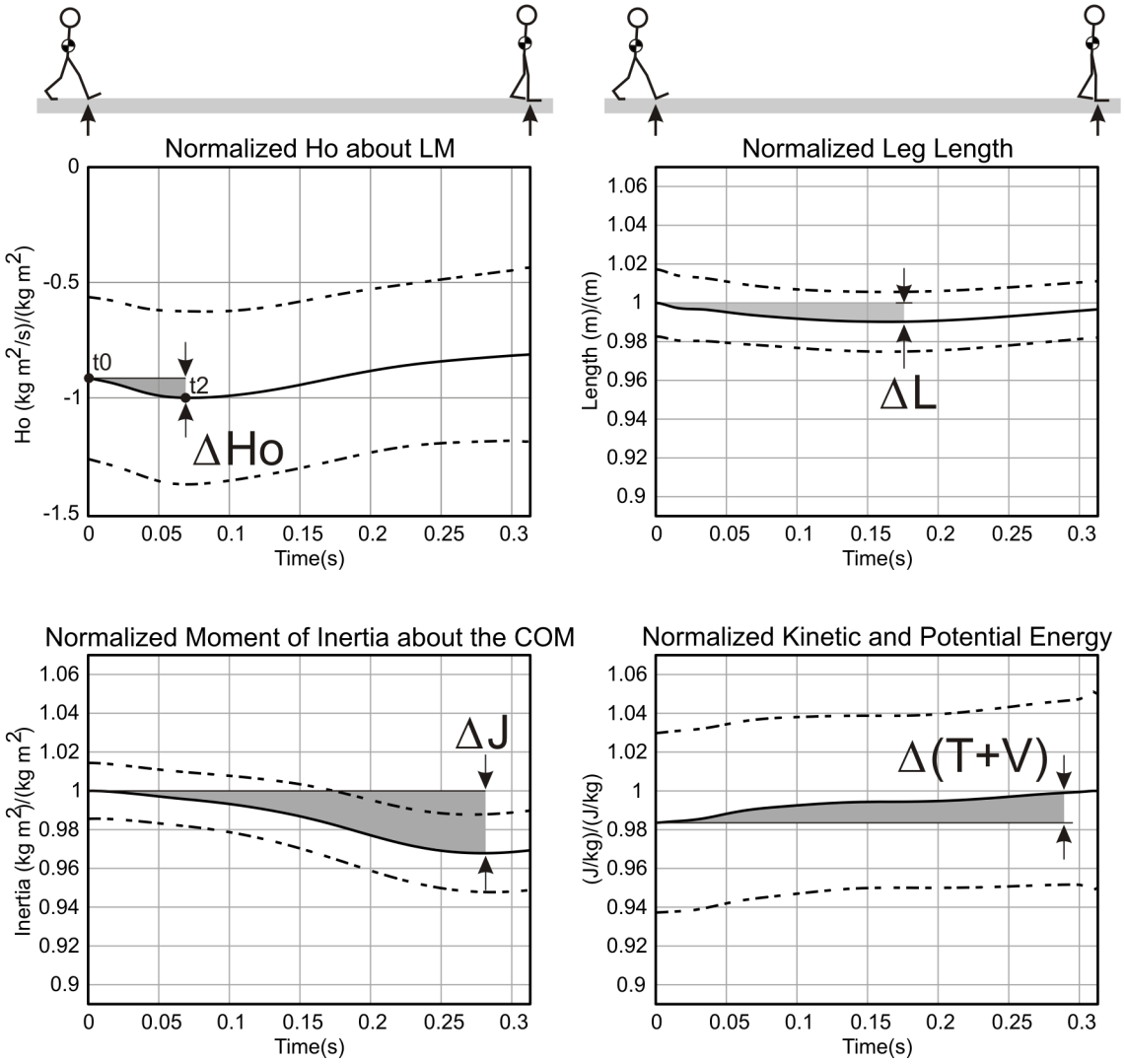

Figure 6.5: Group ensemble plots of dimensionless normalized Ho, L, J, and $T+V$ profiles between heel strike and the moment the COM passes over the LM. Means are drawn with a solid line while ± 1 standard deviation is shown with a dotted line. The natural paced constant cadence trial is shown. The assumption that angular momentum is conserved is violated since it increases. The assumptions of constant L, J and $T+V$ are reasonable. Note that the sum of kinetic and potential energy $(T+V)$ plot does not change appreciably because potential energy (V) dominates and remains relatively constant

FPE assumptions.

Init. & Term.	Slow:-20%	Natural	Fast: 20%
$\frac{\epsilon_{LM}}{\delta H_{LMGP}}\Delta H_{LMGP}$	2.77±1.03	2.68±1.29	2.62±1.55
ϵ_{LM}	3.27±2.40	-2.02±3.18	-6.85±4.43
Cont. Walking	Slow:-20%	Natural	Fast: 20%
$\frac{\delta X(\phi)}{\delta H_{LMGP}}\Delta H_{LMGP}$	2.85 ± 0.62	2.70± 0.87	2.67± 1.04
ϵ_{LM}	2.57± 1.60	-4.12± 1.50	-8.28± 1.45

Table 6.3: Linear approximation of the effect of the velocity-dependent violation of ΔH_{LMGP} on $X(\phi)$. Although the magnitudes are similar to the observed error between $\Delta X(\phi)$ and human foot placement, in almost all cases the systematic violation of the conservation of momentum assumption would make the FPE-HFP error larger than observed. Thus the observed systematic change in FPE-HFP error is likely volitional rather than due to a violation of the assumptions of the model. The final column is in units of *cm*

6.4 Discussion

The simplified biped used by the FPE serves as a useful tool to interpret the functional relevance of the unmodeled velocity and acceleration adjustments that subjects appear to be making. Subjects stepped further behind the FPE as they walked faster (Fig. 6.4). Stepping a constant distance behind the FPE would allow the simplified biped, and thus the person, to maintain a set forward speed rather than stopping (Fig. 6.2). Similarly, stepping further and further behind (ahead) the FPE on each step would cause the simplified biped to accelerate (decelerate) explaining the increased variation in trials with gait initiation and termination.

Most subjects step behind the FPE on average whereas subjects 5 and 6 step ahead; $\sigma(\epsilon_{LM})$ of subjects 3, 5, 11 and 12 hardly changes between continuous walking and trials with gait initiation and termination, whereas it increases appreciably for other subjects. Wight et al.'s simplified biped would suggest that those who on average step ahead of the FPE walk conservatively because they are guaranteed of being able to stop within a single step (Fig. 6.2). Subject-specific biases can also be explained with anthropometric parameter errors. The FPE calculation is dependent on an accurate calculation of whole body angular momentum. The cross product term $((\vec{r}(t)_i - \vec{r}(t)_{LMGP}) \times m_i\vec{v}(t)_i)$ of the

HAT segment makes up 83.6% $\pm$ 1.03% of the whole body angular momentum (across all subjects and trials), making it important to estimate the mass of each subject's HAT segment accurately. The FPE calculation would change by 2-3 cm for a plausible 10% error [50] in the estimate of the mass of the HAT segment. This error is large enough to account for some subject-specific biases, but not all. Accurate means to measure or estimate subject segment masses are needed to interpret the observed subject-specific FPE-HFP biases.

Although the statistical analysis of the FPE-HFP error (ϵ_{LM}) indicates that the predictions of the model correspond well with the experimental data, it does not explain why the simplified model works so well. The model the FPE is based on (Fig. 6.1) bears little physical resemblance to the human form, yet the quantities the model assumes to be constant also appear to be constant during human walking (Fig. 6.5). The normalized group ensemble plots show that three of the four quantities assumed to be constant by the FPE — leg length (ΔL), moment of inertia about the system COM (ΔJ_{COM}) and system energy ($\Delta(T+V)$) — do remain relatively constant during human walking, varying by a few percent at most, and affect the calculated FPE location by millimeters (Tbl. 6.2). Angular momentum however (ΔH_o), does vary during contact and affects the accuracy of the FPE calculation on the order of centimeters (Tbl. 6.2). Although the FPE-HFP error (ϵ_{LM}) is small despite the observed changes in angular momentum, the accuracy of the FPE may change depending on the movement being analyzed. In the case of walking, the assumptions of the FPE appear to be well met, but further study is required to determine what other movements could be analyzed using this algorithm.

6.5 Conclusions

A mathematical understanding of the mechanics of balance control in humans is highly desirable for both its potential to improve gait simulations and also as a clinical diagnostic tool. Foot placement has long been recognized as a critical component of the human balance system, yet relatively little work has been done to find and validate mathematical models to describe this relationship. Wight et al.'s FPE is unique in that it was derived with the sole goal of stabilizing a simplified biped. Importantly, this work has shown that the vast majority of a human step is described by the FPE, and that the differences that do exist are due to an un-modeled adjustment people are making in an effort to maintain

velocity or to accelerate through the stance phase. In addition, during slow and naturally paced gaits, subjects place their metatarsals ahead of the FPE, allowing them to stop without taking an extra step if they desire. Subject-specific differences exist and can be explained using human behavior or anthropomorphic parameter errors. Better means of estimating segment inertial properties are needed before these subject-specific differences can be interpreted properly. This model has great potential to illuminate many areas of gait ranging from quantifying bipedal instability and balance performance, identifying people with compromised balance, and improving forward dynamic gait simulations.

Chapter 7

Discrete Spatial Balance Corrections using Foot Placement

The planar FPE presented in Ch. 6 is able to compute a foot placement location that will allow a human to catch its balance. The FPE has assumptions that are compatible with the mechanics of human walking, and predicts locations that correspond well with experimentally measured human foot placement during both continuous walking and gait termination. The FPE is an important contribution both for the analysis of experimental human data — to determine whether or not a subject is balanced, and if not, how off balance they are — and also for its potential to make human gait simulations more life-like. Although FPE appears to be extremely useful, it can only be applied to planar motion. This is a rather severe restriction because humans, in contrast to the FPE, walk in three dimensions (3D). The FPE theory must be extended to 3D before the potential clinical and simulation benefits of the FPE can be realized.

A 3D extension of Wight et al.'s planar foot placement estimator (FPE) [108] is a promising candidate to help understand the relationship between foot placement and 3D bipedal balance. The FPE calculates where a biped should place its swing foot in the sagittal plane *at that instant* to transition from an unstable state to a statically stable state in a single step without any additional control inputs (Fig. 7.1). The FPE assumes that mass, inertia, system energy and leg length are constant after contact; the foot sticks and does not slip; and that momentum is conserved during foot contact. Leg length is defined as the distance between the contact point 'p' (Fig. 7.1) and the pendulum's center

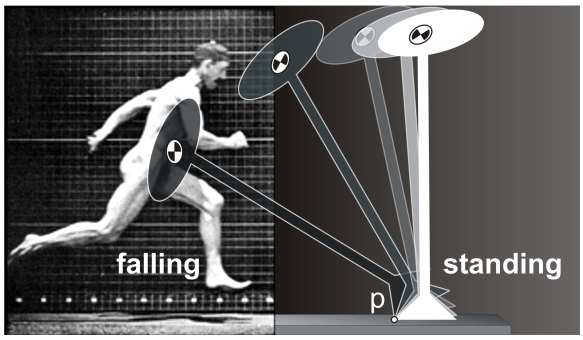

Figure 7.1: The 3DFPE calculates a location that will cause an unstable inverted pendulum (shown in black) to transition to a statically stable pose (shown in white). Human imagery courtesy of Dover [70]

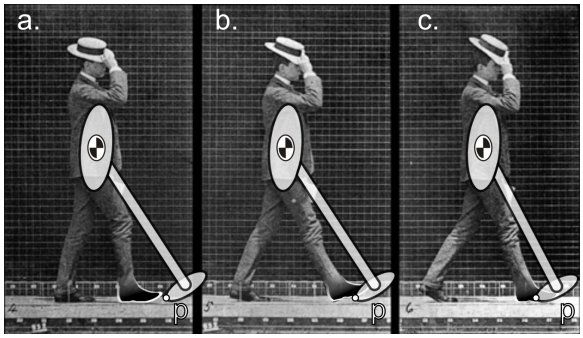

Figure 7.2: The 3DFPE is useful for determining when a biped needs to take a step (or some other action) to stabilize itself (a.) and when center of pressure manipulations (b. and c.) are sufficient to stay upright . Human imagery courtesy of Dover [70]

of mass. The 3DFPE relies on the assumptions of the planar FPE, which have been shown to be reasonable for human gait initiation, termination and walking [66].

The assumption that leg length is fixed may not always be reasonable as human legs have been observed [37], and modeled [26], to behave like compression springs during running and walking. The stiffness of human legs has been observed to vary widely depending on the task [21]. To address this varying compliance, both the rigid leg FPE, and another balance point, Pratt et al.'s capture point (CAP) [82] are considered. The CAP is the foot placement location that restores balance to a pendulum with a telescoping leg that maintains its COM at a constant height. The constant height pendulum is a convenient tool for analysis because it has linear dynamic equations, and so, was coined the 'linear-inverted-pendulum' [47]. Pratt et al. showed that the force the leg would have to generate to maintain the COM at a fixed height could be modeled by a precisely preloaded nonlinear spring. The stiffness of the spring used in the CAP model is more compliant than the apparent stiffness of human legs [26] during walking. It is assumed that the true human foot placement location is bounded by the CAP and FPE locations since human legs are stiffer than the nonlinear spring of the CAP, and more compliant than the rigid leg FPE.

The 3DFPE, the CAP, the center of pressure (COP), and the contact patch of the feet

of the biped can be used to determine when the biped is balanced. The contact point for both the linear and rigid leg inverted pendulums behaves like an instantaneous spherical joint in 3D. The COP beneath the foot of the biped is the closest physical analogy to the contact point of the pendulum, because moments of the GRF about the COP and the contact point of the pendulum sum to zero. If the 3DFPE and CAP locations are within the contact area of the feet of the biped, the biped is balanced because it can shift its center of pressure to match the 3DFPE or CAP, or some point in between depending on its leg stiffness. Conversely, if both the 3DFPE and CAP points are outside the convex hull (smallest single convex region that encloses the human-ground contact area) of the foot (or feet during double stance), the biped will fall unless a step (or some other action) is taken to capture the 3DFPE again.

It is not necessary to step within the 3DFPE and CAP region to prevent a fall, provided another step can be taken. The 3DFPE and CAP region may not always be physically reachable, especially during high velocity activities like running (Fig. 7.1). There are many other locations a biped could place its foot in order to maintain or change its velocity. Raibert identified the neutral step [85] that allowed a 3D inverted hopping robot to maintain a desired horizontal velocity. Assuming that a neutral step location can be identified for any biped, the biped should only need to step on the line connecting the neutral step and the 3DFPE-CAP points in order to slow down, yet maintain its heading. Provided that the foot sticks and does not slip, and that each step decreases the system energy of the biped, a series of steps between the neutral step and the 3DFPE-CAP points will eventually stop the biped.

Before the 3DFPE can be derived, it must be proven that an inverted pendulum has regions in its state space that can be stabilized using foot placement alone. An inverted pendulum model that has a finite foot contact area, similar to a person and most robots, is derived in Sec. 7.1. Lyapunov's direct method is used to establish the stability of the inverted pendulum in Sec. 7.2 along with regions of stability. Regions of validity are presented in Sec. 7.3. The 3DFPE is derived in Sec. 7.4. A preliminary experimental validation of the 3DFPE for use in analyzing human balance is presented in Sec. 7.5.

7.1 Stability of an Euler Pendulum

A simplified model is used to define the conditions under which a 3D monoped could transition from a dynamic state to a metastable pose using foot placement alone. Legged locomotion requires at least one limb, and this limb should have a foot with a non-zero contact area (in the case of a human) to ensure that a metastable standing pose exists. The simplified model resembles a monoped with a disk-shaped foot. A disk-shaped foot has been chosen in an effort to strike a balance between model complexity and fidelity: a disk-shaped foot yields equations of motion of a manageable size, yet will share regions of stability with its human counterpart, particularly when its geometry and inertia parameters are of human proportions. The simplified model is a useful tool for determining broadly what regions of the state space can be stabilized using a single foot placement, but it is not useful for gleaning the fine details of how the geometry of our feet, or our variable whole-body inertia, affect our balance.

The size of the equations-of-motion of the simplified model can be further reduced if the disk-shaped foot is perpendicular to the leg axis, and the inertia matrix has an axis of symmetry about the leg. The resulting model is referred to as an Euler pendulum due to its similarity to the Euler disk [59] (Fig. 7.3 and 7.4). The proposed model differs from an Euler disk by including rolling resistance and spin friction to make the model more realistic, and also to ensure that it is Lyapunov stable. In addition, rigid contact is modeled (using the conservation of angular momentum) to allow the pendulum to rock back and forth between opposing edges.

Of course, the simplified model is valid only when its assumptions are met. This model, and the 3DFPE, assumes that leg length, mass, and inertia are constant. In addition, it is assumed that the contact point sticks to the ground and does not slip. Finally, impacts between the contact ring and the ground are assumed to be plastic and momentum-conserving. These assumptions are very similar to Wight et al.'s planar FPE, shown to be reasonable when used to analyze human walking [66], and are expected to hold when 3D human gait is analyzed. Before the validity of the assumptions of the model are examined, the equations of motion of the Euler pendulum must be derived. The Euler pendulum can interact with the ground at a single point, by rolling without slipping, or it can interact with the ground at multiple points if the contact ring flattens on the ground when the pendulum is rocking from side to side.

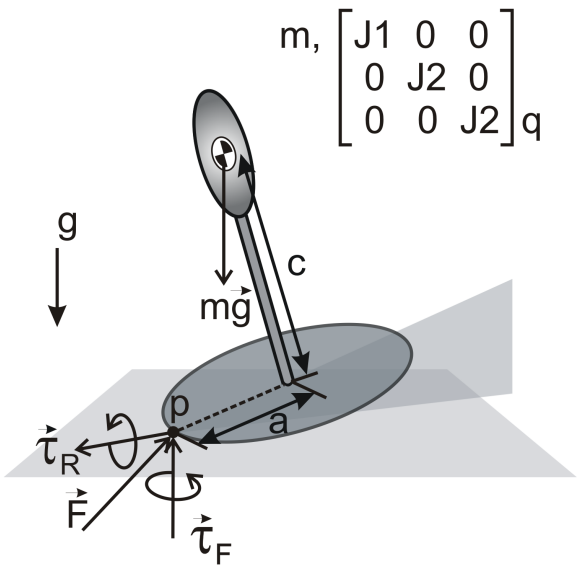

Figure 7.3: Inverted pendulum parameters. A body with mass and inertia is held up by a massless rigid leg and disc-shaped foot. The ring is always touching the ground. Note that $\vec{F}$ is caused by contact and frictional forces while $\vec{\tau_R}$ and $\vec{\tau_F}$ are due to rolling resistance and spin friction, respectively.

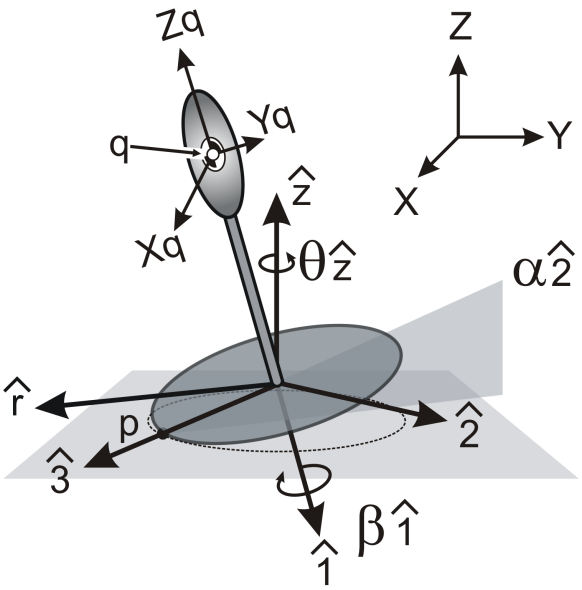

Figure 7.4: The 3DOF Euler pendulum has a disc-shaped foot that is tilted relative to the plane at an angle of α about the $\hat{\mathbf{2}}$ axis. The vector $\vec{r}_{p/q}$ rotates with angular velocity $\dot{\beta}$ about the $\hat{\mathbf{1}}$ axis. Note that frame q is a body-fixed frame centered on the COM of the pendulum

7.1.1 Rolling without Slipping ($\alpha \neq 0$)

The 3D equations of motion (rotating about axis $\hat{\mathbf{1}}$, $\hat{\mathbf{2}}$ and $\hat{\mathbf{3}}$) of an Euler pendulum with rolling resistance and spin friction when it is rolling without slipping are shown in Eqns. 7.1, 7.2 and 7.3. This motion may be similar to real world bipedal locomotion when the COP is moving around the edge of the foot — as it might during corner turning. While the pendulum is rolling without slipping it is assumed that the contact ring touches the

ground only at a single point. The accelerations $\ddot{\beta}$, $\ddot{\alpha}$ are aligned with the $\hat{\mathbf{1}}$ and $\hat{\mathbf{2}}$ axes. The reference frame is oriented such that the $\hat{\mathbf{1}}$ axis intersects the COM and is perpendicular to the disc, while the $\hat{\mathbf{3}}$ axis passes through the point of contact. The $\hat{\mathbf{2}}$ axis can be found by crossing the $\hat{\mathbf{3}}$ axis with the $\hat{\mathbf{1}}$ axis.

Means of energy dissipation through rolling resistance and spin friction have been included in the model to ensure that it is stable in the sense of Lyapunov [49]. Details of the Euler pendulum equations of motion, the rolling resistance, and spin friction models can be found in Appendix C.

$$\ddot{\beta} = \dot{\alpha}\frac{cam(J_1+J_2)\dot{\beta} + amJ_2(c\cos(\alpha) - a\sin(\alpha))\dot{\theta}}{J_1J_2 + m(J_2a^2 + J_1c^2)} + \mathcal{L}_\beta \tag{7.1}$$

$$\begin{aligned}\ddot{\alpha} &= \dot{\theta}^2\frac{(cam(1-\cos^2\alpha) + (mc^2+2J_2)\sin\alpha\cos\alpha)}{m(a^2+c^2)+J_2} \\ &\quad +\dot{\theta}\dot{\beta}\frac{(ma^2+J_1+J_2)\sin\alpha + cam\cos\alpha}{m(a^2+c^2)+J_2} \\ &\quad +\frac{mg(c\sin\alpha - a\cos\alpha)}{m(a^2+c^2)+J_2} + \mathcal{L}_\alpha\end{aligned} \tag{7.2}$$

$$\begin{aligned}\ddot{\theta} &= -\dot{\alpha}\frac{\dot{\theta}\left((3J_1J_2 + 3J_2ma^2 + 2c^2mJ_1)\cos\alpha + cmaJ_1\sin\alpha\right)}{(J_1J_2 + J_2ma^2 + c^2mJ_1)\sin\alpha} \\ &\quad -\dot{\alpha}\frac{\dot{\beta}\left(J_1J_2 + ma^2(J_1+J_2) + J_1^2\right)}{(J_1J_2 + J_2ma^2 + c^2mJ_1)\sin\alpha} + \mathcal{L}_\theta\end{aligned} \tag{7.3}$$

Parameters c and a are the height of the pendulum, and radius of the contact ring respectively (Fig. 7.3). The pendulum has mass m, and a diagonal inertia matrix with scalar entries J_1 and J_2 (Fig. 7.3). This simplified inertia matrix has been chosen to keep the size of the equations small enough to print, though the analysis that follows has been tested on a general inertia matrix. Rolling resistance and spin friction terms are expressed in Eqns. 7.1, 7.2 and 7.3 as $\mathcal{L}_\beta$, $\mathcal{L}_\alpha$ and $\mathcal{L}_\theta$ for brevity.

The equations of motion of Wight et al.'s 2D model is embedded in the Euler pendulum equations presented above. Wight et al.'s model equations can be found by projecting the

above model onto the $\hat{\mathbf{X}}$ $\hat{\mathbf{Z}}$ plane. This is achieved easily by setting $\theta = \beta = 0$ which makes the $\hat{\mathbf{2}}$ axis parallel to the $\hat{\mathbf{Y}}$ axis. The projected term is shown below, with the rolling resistance torque set to zero.

$$\ddot{\alpha} = \ddot{\theta}_W = \frac{mg(c\sin\alpha - a\cos\alpha)}{m(a^2+c^2)+J_2} + \cancelto{0}{\mathcal{L}_\alpha} \tag{7.4}$$

$$= \frac{mgL\sin(\theta_W - \frac{1}{2}\beta_W)}{I_{com}+mL^2} \tag{7.5}$$

Wight et al.'s L is the length of the hypotenuse between the perpendicular vectors $\vec{a}$ and $\vec{c}$ of the Euler pendulum. Also Wight et al.'s I_{com} is equivalent to J_2. Wight et al.'s $\beta_W/2$ is the angle between the leg of the pendulum and the contact ring ($\tan(\frac{\beta_W}{2}) = \frac{a}{c}$) of the Euler pendulum. The simple trigonometric substitution $\sin(\alpha \pm \beta) = \sin\alpha\cos\beta \pm \cos\alpha\sin\beta$ can be used to show that the 2D projection of the Euler pendulum equations and Wight et al.'s 2D model are identical.

7.1.2 Rocking ($\alpha = 0$)

In the special case where the pendulum is in pure rotation about the $\hat{\mathbf{2}}$ axis and $\alpha = 0$, Eqns. 7.1, 7.2, and 7.3 are invalid when the ring flattens on the ground, thereby touching multiple ground points. This motion may be similar to real world bipedal locomotion when the COP begins at one edge of the foot and transitions rapidly across the foot to the opposing edge of the foot — as is the case during normal walking and gait termination. It should be noted that α approaches zero only if $\dot{\beta} = \dot{\theta} = 0$, else Eqn. 7.3 computes a very high value for $\ddot{\theta}$, quickly increasing $\dot{\theta}$, and forcing $\ddot{\alpha}$ in Eqn. 7.2 positive with a large centripetal acceleration. The state of the pendulum after contact can be calculated by assuming that the impact is perfectly plastic and momentum-conserving; momentum is represented by the vector $\vec{H}p$, taken about point p (the point of contact) at the time 1 prior to contact, and the time 2 just after contact.

$$\vec{H}p_1 = \vec{H}p_2 \tag{7.6}$$

Since $\dot{\beta} = \dot{\theta} = 0$, when the contact ring flattens on the ground, it is assumed that the new

contact point is located opposite the current one, that is located at $c\ \hat{\mathbf{1}}\ -a\ \hat{\mathbf{3}}$ from the COM.

$$\begin{aligned} \vec{Hp}_1 &= [J]\cdot\vec{\omega}_1 + \vec{r}_{q/p}\times m(\vec{\omega}_1\times\vec{r}_{q/p}) \\ &= [J]\,\vec{\omega}_1 + (-c\ \hat{\mathbf{1}}\ -a\ \hat{\mathbf{3}}\ )\times m(\vec{\omega}_1\times(c\ \hat{\mathbf{1}}\ -a\ \hat{\mathbf{3}}\ )) \end{aligned} \tag{7.7}$$

Before $\vec{Hp}_1$ is calculated, however, $\vec{\omega}_1$ must be expressed in the post-contact reference frame. The post-contact reference frame is rotated π radians about the $\hat{\mathbf{1}}$ axis so that the $\hat{\mathbf{3}}$ axis passes through the new contact point, changing the signs of the $\hat{\mathbf{2}}$ and $\hat{\mathbf{3}}$ components.

$$\vec{\omega}_1 = \left\{\dot{\beta}_1\ \hat{\mathbf{1}}\ -\dot{\alpha}_1\ \hat{\mathbf{2}}\ +\dot{\theta}_1\cancelto{0}{\sin\alpha_1}\ \hat{\mathbf{3}}\ \right\} \tag{7.8}$$

The angular momentum of the pendulum prior to contact, expressed in the post-contact reference frame can now be computed.

$$\begin{aligned} \vec{Hp}_1 &= \left((J_1-ma^2)\dot{\beta}_1 - (mca)\cancelto{0}{\sin\alpha}\dot{\theta}_1\right)\ \hat{\mathbf{1}} \\ &\quad + \left((m(a^2-mc^2)-J_2)\dot{\alpha}_1\right)\ \hat{\mathbf{2}} \\ &\quad + \left((J_2+c^2m)\cancelto{0}{\sin\alpha}\dot{\theta}_1 - (mca)\dot{\beta}_1\right)\ \hat{\mathbf{3}} \end{aligned} \tag{7.9}$$

After contact, the pendulum has an angular velocity of $\vec{\omega}_2$,

$$\vec{\omega}_2 = \left\{\dot{\beta}_2\ \hat{\mathbf{1}}\ +\dot{\alpha}_2\ \hat{\mathbf{2}}\ -\dot{\theta}_2\cancelto{0}{\sin\alpha_2}\ \hat{\mathbf{3}}\ \right\} \tag{7.10}$$

and angular momentum about its new contact point that is nearly identical to Eqn. 7.7.

$$\vec{Hp}_2 = [J]\cdot\vec{\omega}_2 + \vec{r}_{q/p}\times m(\vec{\omega}_2\times\vec{r}_{q/p}) \tag{7.11}$$

$$= [J]\,\vec{\omega}_2 + (-c\ \hat{\mathbf{1}}\ -a\ \hat{\mathbf{3}}\ )\times m(\vec{\omega}_2\times(-c\ \hat{\mathbf{1}}\ -a\ \hat{\mathbf{3}}\ )) \tag{7.12}$$

The angular velocity of the pendulum about the new contact point can be found by substituting Eqns. 7.9 and 7.12 into Eqn. 7.6 and solving for $\dot{\beta}_2$, $\dot{\alpha}_2$ and $\dot{\theta}_2$.

$$\vec{\omega}_2 = -\dot{\alpha}_1 \left(\frac{J_2 + m(c^2 - a^2)}{J_2 + m(a^2 + c^2)} \right) \hat{\mathbf{2}} \tag{7.13}$$

Equation 7.13 can be converted into Wight et al.'s Eqn. 7 using the cosine law.

By using the equations of motion associated with rolling detailed in Sec. 7.1.1 and 7.1.2, the movements of the pendulum can be predicted using integration when the COP is on the edge of the foot, or is moving from edge to edge through the contact patch of the foot.

7.2 Defining Stable Regions

The definitions for stable regions are very similar to those that Wight et al. [108] defined:

Definition: The Euler pendulum has fallen if $\dot{\alpha} = 0$ and any point other than the set of points that make up the circular contact area is touching the ground.

Definition: The Euler pendulum is stable if $\dot{\alpha} = 0$ and it has not fallen.

Definition: The Euler pendulum is balanced if, for a given set of initial conditions, and no further energy inputs to the system, it eventually becomes stable. Once stable, a small, impulsive, non-zero external disturbance should result in motion that converges to a stable state.

The model will first be shown to be stable in the sense of Lyapunov before the regions of stability are formally expressed. The candidate energy function of choice is simply the system energy, the sum of kinetic and potential energy.

$$\begin{aligned} U &= T + V & (7.14) \\ &= (\frac{1}{2} m \vec{v}_{cm}^T \vec{v}_{cm} + \frac{1}{2} \vec{\omega} \cdot [J] \vec{\omega}) \\ &\quad + mg(a \sin\alpha + c \cos\alpha) & (7.15) \end{aligned}$$

If $\dot{U} < 0$ for a ball centered in the state space about the equilibrium point of interest ($\alpha = \dot{\beta} = \dot{\alpha} = \dot{\theta} = 0$), then according to Lyapunov's Direct Method the equilibrium point is asymptotically stable.

$$\begin{aligned} \dot{U} &= m(\vec{v}_{cm}^{T}\dot{\vec{v}}_{cm}) + \frac{1}{2}\left(\dot{\vec{\omega}} \cdot [J]\vec{\omega} + \vec{\omega} \cdot [J]\dot{\vec{\omega}} + \vec{\omega} \cdot (\vec{\omega} \times ([J]\vec{\omega}))\right) \\ &\quad +\dot{\alpha}mg(a\cos\alpha - c\sin\alpha) \end{aligned} \tag{7.16}$$

After substituting in Eqns. 7.1, 7.2, 7.3, C.9, C.11, C.12, C.13, C.15, C.19, and C.25 and significant simplification (using Maple), an equation for $\dot{U}$ in terms of the state vector (β,α,θ,$\dot{\beta}$,$\dot{\alpha}$,$\dot{\theta}$) is yielded. Direction vectors of angular velocity vector normal ($\hat{\boldsymbol{\omega}}_N$) and tangential ($\hat{\boldsymbol{\omega}}_T$) to the horizontal plane are expressed using subscripts. The scalar quantity ω_{rel} is defined in App. C, Eqn. C.10. The positive scalar terms R and S are the magnitudes of the rolling resistance and friction torques defined in App. C, Eqns. C.19 and C.25).

$$\begin{aligned} \dot{U} &= (-R\hat{\boldsymbol{\omega}}_T \cdot \hat{\boldsymbol{\omega}}_T)\left(\omega_{rel}^2 \sin^2\alpha + \dot{\alpha}^2\right) \\ &\quad (-S\hat{\boldsymbol{\omega}}_N \cdot \hat{\boldsymbol{\omega}}_N)\left(\omega_{rel}\cos\alpha - \dot{\theta}\right)^2 \leq 0 \end{aligned} \tag{7.17}$$

Equation 7.17 is always less than or equal to zero provided that the contact ring is touching the ground ($\vec{F} \cdot \ \hat{\mathbf{z}} \ > 0$). The expression for $\dot{U}$ may be zero at a location other than the origin if the magnitude of the angular velocity, $|\vec{\omega}| = 0$, is zero (physically this corresponds to the Euler pendulum being balanced on its contact ring at a single point).

When the pendulum is rocking rather than rolling without slipping, a difference of U before contact (U_1) and after contact (U_2) are be used in the place of $\dot{U}$. Substituting in Eqns. 7.8 and 7.13, and simplifying to solve for U_2 and U_1 yields:

$$U_2 - U_1 = -2\frac{\dot{\alpha}^2 ma^2(J_2 + mc^2)}{J_2 + m(a^2 + c^2)} \tag{7.18}$$

Equation 7.18 is always negative (except at the origin); thus the Euler pendulum loses energy every time it flattens out on the ground.

We have now shown that $\dot{U} \leq 0$ everywhere in the state space. If the Lyapunov candidates are limited to the range of $\alpha < \arctan(a/c)$ then U is positive-definite. Using Barbashin's theorem [49], the origin is an asymptotically stable equilibrium point in the sense of Lyapunov. The Lyapunov stability proof and Barbashin's theorem also holds for the Euler pendulum with any arbitrary inertia matrix (tested using Maple), though the intermediate expressions are far larger.

A phase portrait for an Euler pendulum with low rolling resistance and spin friction ($\kappa = 0.001$, $\mu_S = 0.01$ for the rolling resistance and spin friction models, see App. C for details) of human-scale dimensions ($m = 75kg$, $J_1 = 12kg\,m^2, J_2 = 13kg\,m^2$, $c = 1.0m$, $a = 0.10m$) is shown in Fig. 7.5 for a variety of initial conditions over α and $\dot{\alpha}$ with $\dot{\theta} = 0$ and $\dot{\theta} = 5$. The greyed out regions indicate unstable trajectories while the white areas contain trajectories that terminate in an upright standing pose.

Although human feet and robotic feet do not resemble the contact ring of the Euler pendulum, the Euler pendulum is useful for understanding how foot placement affects 3D balance. The phase portraits (Fig. 7.5) show that there exists a set of initial conditions that allow an unstable inverted Euler pendulum to transition to a statically stable standing pose. In addition, a region of stability exists (the 3^{rd} region of stability, defined in Sec. 7.2.3) with the COM outside its base of support if the pendulum has negligible amounts of angular momentum about a vertical axis. As angular momentum about the $\hat{\mathbf{z}}\ (t)$ axis increases, the size of the region of stability outside of the foot's contact area decreases, and eventually disappears (Fig. 7.5). This makes intuitive sense: if angular momentum about the vertical is negligible, the 3D model behaves like Wight et al.'s [108] 2D model. In addition, all regions of stability increase in size as the rate of energy loss through rolling resistance or spin friction increases.

Foot contact can be used as a state change mechanism to allow the pendulum to transition from an unstable state to a statically stable standing pose. Provided that a human or robot being analyzed behaves like the model presented, there exists a family of initial conditions that can be stabilized using foot placement alone. The following sections describe the regions of stability of the Euler pendulum and the regions of state space where the model is valid.

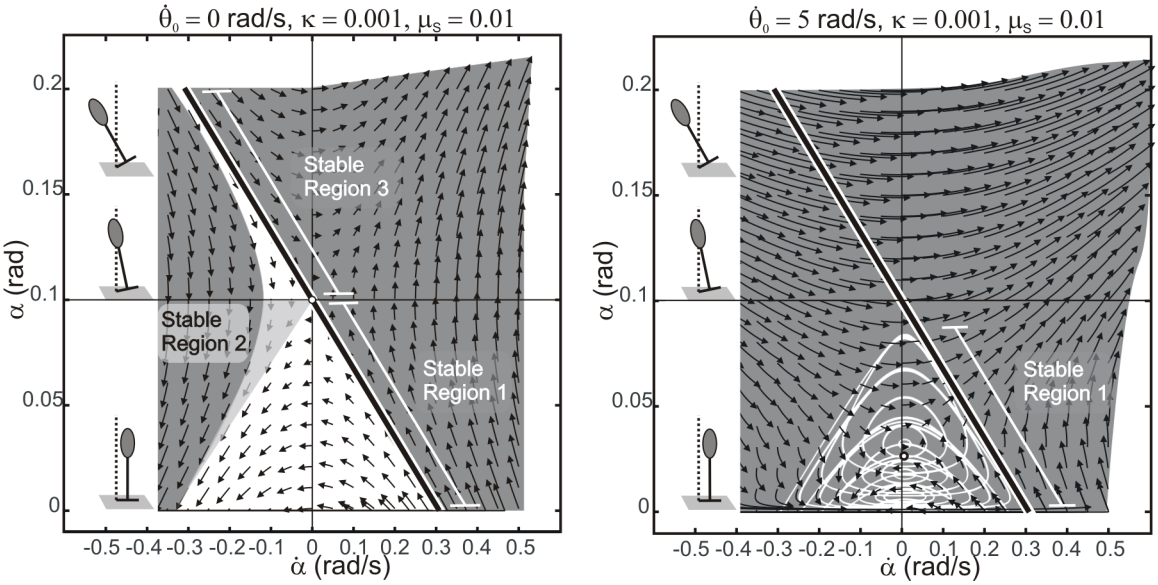

Figure 7.5: Phase portraits of a human-sized Euler pendulum (a=0.1m, c=1m, m=75kg) over α and $\dot{\alpha}$. Regions of stability are shown in white and light grey, while regions of instability are shown in dark gray. The regions of stability are defined in Sec. 7.2.1-7.2.3. The first, and to a lesser degree the second, region of stability (below $\alpha = 0.1$) are relatively large. The 3^{rd} region of stability (above $\alpha = 0.1$) shrinks as $\dot{\theta}$ increases, vanishing in this case before $\dot{\theta} = 0.125$. The regions of stability increase in size as rate of energy dissipation (due to rolling resistance and spin friction) increase. The solutions of the 3DFPE are illustrated with the diagonal black line (using the method presented in Sec. 7.4). Note that the contact location of the 3DFPE would balance the biped when $\dot{\theta} = 0$, but not when $\dot{\theta} = 5$

7.2.1 Stable Region 1

The system is stable if $\alpha < \arctan(a/c)$ and the total system energy $T + V$ is less than the peak potential energy. The pendulum has insufficient energy to escape the energy well created by the foot. All of the expressions for the various regions of stability are derived assuming that energy losses due to rolling resistance are insignificant.

$$
\begin{aligned}
mgh_{peak} &\geq U_0 = T_0 + V_0 && (7.19)\\
mg\sqrt{a^2+c^2} &\geq \left(\frac{1}{2}m\vec{v}_{cm,0}^{T}\vec{v}_{cm,0} + \frac{1}{2}\vec{\omega}_0^{T}\left(J\vec{\omega}_0\right)\right)\\
&\quad + mg(a\sin\alpha_0 + c\cos\alpha_0) && (7.20)
\end{aligned}
$$

Rearranging to isolate separate potential and kinetic energy terms:

$$
\begin{aligned}
2mg\left(\sqrt{a^2+c^2} - c\cos\alpha_0 - a\sin\alpha_0\right) &\geq \dot{\alpha}_0^2\left(m\left(a^2+c^2\right)+J_2\right) + \left(\dot{\theta}_0\,\sin\alpha\right)^2\left(m\,c^2+J_2\right)\\
&\quad + 2\dot{\beta}_0\dot{\theta}_0\,mca\,\sin\alpha_0 + \dot{\beta}_0^2\left(ma^2+J_1\right) && (7.21)
\end{aligned}
$$

Provided $\dot{\beta}_0, \dot{\alpha}_0$ and $\dot{\theta}_0$ lie in the ellipsoid specified in Eqn. 7.21, $\dot{\alpha}$ will have an orbit that decays towards the equilibrium point at $\alpha = 0$ and the pendulum will transition to a stable state. The simple trigonometric substitution $\cos(\alpha \pm \beta) = \cos\alpha\cos\beta \mp \sin\alpha\sin\beta$ can be used to show that the 2D projection of Eqn. 7.21 (achieved by setting $\dot{\theta} = \dot{\beta} = 0$) is identical to Wight et al.'s Eqn. 26.

7.2.2 Stable Region 2

If the energy losses during impacts are taken into account when the contact ring flattens on the ground ($\dot{\theta} = \dot{\beta} = 0$), a higher initial system energy is allowed than in stable region 1. As in stable region 1, rolling resistance losses are assumed to be insignificant.

$$
\begin{aligned}
mg\,\sqrt{a^2+c^2} &> T_2 + V_2 && (7.22)\\
mg\sqrt{a^2+c^2} &> \frac{1}{2}m\vec{v}_{cm,2}^{T}\vec{v}_{cm,2} + \frac{1}{2}\vec{\omega}_2^{T}\left([J]\vec{\omega}_2\right)\\
&\quad + mg(c\cos(\alpha) + a\sin(\alpha)) && (7.23)
\end{aligned}
$$

Substituting Eqn. 7.13 (the relationship between the pre- and post-contact angular velocity of the pendulum) into Eqn. 7.23 and solving for $\dot{\alpha}_1$ yields:

$$\dot{\alpha}_1^2 < 2mg(\sqrt{a^2+c^2}-c)\left(\frac{J_2+m(a^2+c^2)}{(J_2+m(c^2-a^2))^2}\right) \tag{7.24}$$

The system energy of the pendulum just prior to contact is given by

$$T_1 + V_1 = \frac{1}{2}(J_2 + m(a^2+c^2))\dot{\alpha}_1^2 + mgc \tag{7.25}$$

Provided the inequality of Eqn. 7.24 is satisfied, after contact the pendulum will not have enough kinetic energy to escape the stable region, and will approach the equilibrium point of $(\dot{\beta}, \dot{\alpha}, \dot{\theta}, \beta, \alpha, \theta) = 0$. Prior to contact, the pendulum may have any angular velocity $\alpha_0\ \hat{\mathbf{2}}$, provided that it is in the statically stable region ($\alpha < \arctan(a/c)$) and has a system energy $(T_0 + V_0)$ that does not exceed its maximum system energy just prior to contact given in Eqn. 7.25.

$$T_0 + V_0 \leq T_1 + V_1 \tag{7.26}$$

Substituting in Eqn. 7.24 and 7.25 into Eqn. 7.26 and solving for $\dot{\alpha}_0$ yields an inequality that must be satisfied for the pendulum to stay in the stable region.

$$\begin{aligned}\dot{\alpha}_0^2 \;<\; & 2mg(\sqrt{a^2+c^2}-c)\frac{J_2+m(a^2+c^2)}{(J_2+m(c^2-a^2))^2} \\ & -2mg\frac{a\sin\alpha_0 + c(\cos\alpha_0 - 1)}{m\,(a^2+c^2)+J_2}\end{aligned} \tag{7.27}$$

This region of stability is equivalent to Wight et al.'s Eqn. 37 denoting the second region of stability and can be verified using the cosine law and the addition and subtraction trigonometric identities. Note that Wight et al.'s Eqns. 38 and 39 have the incorrect sign associated with the $\cos\beta/2$ term.

7.2.3 Stable Region 3

The pendulum may transition into stable regions 1 and 2 even if it begins outside of them ($\alpha_0 > \arctan(a/c)$). This is possible only if the system loses energy once it enters the stable

region through rolling resistance or rocking. Since the foot, and thus the stable region, has a finite area there are many trajectories that enter the stable region. Many of these solutions would be curved by gravity, and cannot be found analytically. This is further complicated by the finite foot area: as the trajectory is curved by gravity, the contact point touching the ground changes. If, however, the pendulum rotates in a vertical plane

$$\vec{H}p_2 \cdot \vec{g} = \vec{H}p_1 \cdot \vec{g} = 0 \tag{7.28}$$

and perpendicular to the leg vector (Eqn. 7.28 and 7.29),

$$\vec{H}p_2 \cdot \vec{r}_{p/q} = \vec{H}p_1 \cdot \vec{r}_{p/q} = 0 \tag{7.29}$$

the trajectory of the COM will rotate in a plane — because the contact point will not move — that intersects the contact patch of the foot. As is shown in App. C.1, Eqns. C.29 and C.31 are satisfied if the there is no angular momentum about the vertical axis prior to contact ($\vec{\omega}_1 \cdot \vec{r}_{p/q} = 0$); the pre-contact angular velocity vector is perpendicular to the leg vector ($\vec{\omega}_1 \cdot \vec{r}_{p/q} = 0$); and the horizontal components of the linear velocity and the leg vector are parallel.

There are curved trajectories that do not satisfy Eqns. 7.28 and 7.29 yet lead the COM into a statically stable pose. The size of the family of curved trajectories that violate Eqns. 7.28 and 7.29 yet lead to the region of stability is related to the ratio of the diameter of the foot to the height of the pendulum. In one extreme the height of the pendulum is insignificant in comparison to its foot size and the system behaves like an Euler disk [59], with many curved trajectories that stabilize the pendulum and few that cause it to flip. In the other extreme, the foot shrinks to a point contact and there are no curved trajectories that lead to the region of stability, which has been reduced to an unstable saddle point. The family of curved trajectories that lead to a statically stable pose will be ignored for the remainder of the paper because they are dependent on system geometry and cannot be found without simulation.

The pendulum is in the 3^{rd} region of stability if Eqns. 7.28 and 7.29 are satisfied and the pendulum has enough kinetic energy to enter, but not escape, the metastable pose. The pendulum must have a system energy that is larger than the peak potential energy to enter the stable region.

$$
\begin{aligned}
mg\sqrt{a^2+c^2} &< T_2 + V_2 && (7.30)\\
mg\sqrt{a^2+c^2} &< \left(\frac{1}{2}m\vec{v}_{cm,2}^{T}\vec{v}_{cm,2} + \frac{1}{2}\vec{\omega}_2^{T}\left([J]\vec{\omega}_2\right)\right) \\
&\quad + mg(a\sin\alpha_2 + c\cos\alpha_2) && (7.31)
\end{aligned}
$$

Note that this is simply Eqn. 7.20 except the pendulum must have *at least* this system energy in order to enter the region of stability. An expression of the value for the minimum angular velocity, $\dot{\alpha}_{0,LB}$, to enter the stable region can be found using Eqn. 7.31 if Eqns. 7.28 and 7.29 are satisfied.

$$
\dot{\alpha}_0^2 > \frac{2mg\left(\sqrt{a^2+c^2} - c\cos\alpha_0 - a\sin\alpha_0\right)}{\left(m\left(a^2+c^2\right)+J_2\right)} \tag{7.32}
$$

The pendulum may enter the region of stability with more kinetic energy when purely rotating about the $\hat{\mathbf{2}}$ axis because it will rock, and lose energy (due to the plastic impact) every time the contact ring flattens out. The expression for this upper bound is identical to Eqn. 7.27 for the 2^{nd} region of stability except the pendulum may begin outside the region of stability.

$$
\begin{aligned}
\dot{\alpha}_0^2 &< 2mg(\sqrt{a^2+c^2} - c)\frac{J_2 + m(a^2+c^2)}{(J_2 + m(c^2-a^2))^2} \\
&\quad -2mg\frac{a\sin\alpha_0 + c(\cos\alpha_0 - 1)}{m\left(a^2+c^2\right)+J_2} && (7.33)
\end{aligned}
$$

This region of stability is equivalent to Wight et al.'s Eqn. 45 (with the sign error on the $\cos\beta/2$ term corrected) denoting the 3^{rd} region of stability.

7.3 Region of Validity

The model assumes that the foot sticks and does not slip, but these assumptions are not reasonable in all situations. When the magnitude of the horizontal contact force exceeds

the allowable force of friction or when the contact force goes below zero, the results of the model are invalid. Impulse-momentum equations can be used to calculate the average size and direction of the ground impulse during contact ($\vec{F}_C$). After contact, Euler pendulum equations can be used to determine if the contact point slips, or if the pendulum loses contact with the ground.

During contact the ground impulse is given by:

$$\begin{aligned} \vec{F}_C \Delta t &= m(\vec{v}_2 - \vec{v}_1) && (7.34) \\ &= m(\vec{\omega}_2 \times \vec{r}_{q/p} - \vec{v}_1) && (7.35) \end{aligned}$$

The post-contact COM velocity ($\vec{v}_2$ with $\vec{v}_1$ being the pre-contact COM velocity) can be found by assuming that the contact is momentum-conserving and that the pendulum is moving in a pure rotation about the contact point.

$$\begin{aligned} \vec{H}p_1 &= \vec{H}p_2 && (7.36) \\ [J]\,\vec{\omega}_1 + \vec{r}_{q/p} \times m\vec{v}_1 &= [J]\,\vec{\omega}_2 + \vec{r}_{q/p} \times m(\vec{\omega}_2 \times \vec{r}_{q/p}) && (7.37) \end{aligned}$$

In general, symbolic solutions for $\vec{\omega}_2$ in Eqn. 7.37 are quite complicated. The expression for ($\vec{F}_C$) becomes simple if cross product terms dominate the angular momentum of the pendulum (as is the case with human walking [38]). After setting the $[J]\omega$ terms to zero, assuming that $\vec{\omega}_2 \perp \vec{r}_{p/q}$ (consistent with our assumption for the 3^{rd} region of stability), and making use of the double vector product, the expression for the impulse becomes

$$\vec{F}_C \Delta t = -m \left(\frac{\vec{r}_{q/p} \cdot \vec{v}_1}{\vec{r}_{q/p} \cdot \vec{r}_{q/p}} \right) \vec{r}_{q/p} \qquad (7.38)$$

Since the direction of $\vec{F}_C$ in Eqn. 7.38 is identical to the direction vector of the leg, the foot will not slip provided the ratio of the horizontal to vertical component of the vector of the leg is less than the coefficient of friction ($\vec{r}_{q/p} \cdot \hat{\imath} / \vec{r}_{q/p} \cdot \hat{\jmath} \leq \mu_L$).

After contact, Eqn. C.16 can be rearranged to calculate the contact forces between the pendulum and the ground ($\vec{F}_R$) when it is rolling without slipping.

$$\vec{F} = m\frac{d^2\vec{r}_{q/p}}{dt^2} + mg\ \hat{\mathbf{z}} \tag{7.39}$$

The assumption that the pendulum remains in contact with the ground after contact can be found by examining the magnitude of the $\hat{\mathbf{z}}$ component of $\vec{F}$.

$$0 < \vec{F} \cdot\ \hat{\mathbf{z}} \tag{7.40}$$

$$0 < (a\cos\alpha - c\sin\alpha)m\ddot{\alpha} - (c\cos\alpha + a\sin\alpha)m\dot{\alpha}^2 + mg \tag{7.41}$$

The 2D projection of Eqn. 7.41 (achieved by setting $\ddot{\theta} = \dot{\theta} = \ddot{\beta} = \dot{\beta} = 0$) matches Wight et al.'s normal force equation (Eqn. 52) after minor corrections of Wight et al.'s Eqn. 50. The gravitational force mg term in Wight et al.'s Eqn. 50 should have not have been scaled by $\cos(\theta + \beta/2)$.

The assumption that the contact point sticks and does not slip after contact is only valid if the ratio of the horizontal to vertical ground reaction forces does not exceed the coefficient of friction (μ_L) when the Euler pendulum is rolling without slipping. Note that the $\hat{\mathbf{2}}$, and the $\hat{\mathbf{r}} = \hat{\mathbf{2}} \times \hat{\mathbf{z}}$ (Fig. 7.4) axes span the horizontal plane.

$$\frac{|\vec{F} \cdot (\ \hat{\mathbf{r}}\ +\ \hat{\mathbf{2}}\ )|}{\vec{F} \cdot\ \hat{\mathbf{z}}} < \mu_L \tag{7.42}$$

The expanded version of Eqn. 7.42 has been omitted for brevity, though it can be found by substituting in Eqns. 7.42, C.3, C.7 and C.16. The 2D projection of Eqn. 7.42 (achieved by setting $\ddot{\theta} = \dot{\theta} = \ddot{\beta} = \dot{\beta} = 0$) matches Wight et al.'s Eqn. 60.

7.4 Modeling Foot Placement

Now that it has been shown that foot placement can be used to stabilize a 3D inverted pendulum with a foot (in certain regions of its state space) we will concentrate on deriving a method to find a desirable foot placement location given the state of the pendulum.

The 3DFPE is an estimate of a good location to place a point contact foot to cause a 3D inverted pendulum with a rigid leg (Fig. 7.6) to transition from a dynamic state to a static standing pose. We assume that the plant to which the 3DFPE is being applied can maintain its balance once the ground projection of the COM is within the convex hull of its foot — as is the case for the Euler pendulum (Fig. 7.5). The assumptions of the 3DFPE are very similar to those of the Euler pendulum: mass, inertia and leg length are constant; the foot sticks and does not slip; and that the contact is momentum-conserving. In addition, the 3DFPE assumes that a foot placement location that satisfies Eqns. 7.28 and 7.29 can be found.

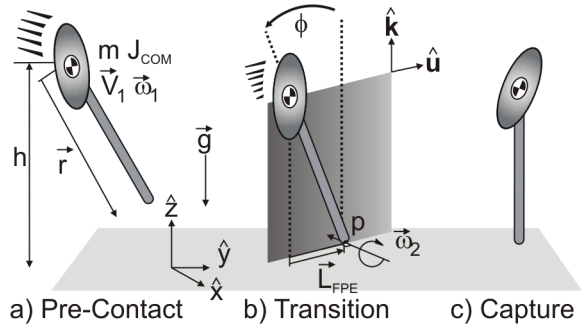

Figure 7.6: The 3D foot placement estimator searches for a foot placement location for an unstable body (Fig. a) that causes the body to enter the 3^{rd} region of stability (Fig. b) and not exit.

The pendulum will rotate in a plane that intersects with the foot location if $\vec{H}p_1$ and $\vec{H}p_2$ are perpendicular to a vertical plane containing $\vec{r}$, thereby satisfying Eqns. 7.28 and 7.29. If such a projection plane can be found, then there exists a location, along the line formed by the intersection of the projection plane and the ground, that will cause the pendulum to transition into the 3^{rd} region of stability detailed in Sec. 7.2.3. A candidate plane can be formed by using two vectors, one parallel to gravity and the other a horizontal direction vector $\hat{\mathbf{u}}$ that is perpendicular to the angular momentum vector of the body ($\vec{H}_{GP}$), taken about the COM ground projection location. Angular momentum is being taken about the COM ground projection $\vec{H}_{GP}$ to approximate the direction of $\vec{H}_{p1}$ after contact because the point $p1$, the 3DFPE location, has not yet been solved for. If the pendulum can enter the 3^{rd} region of stability, the direction of $\vec{H}_{GP}$ and $\vec{H}_{p1}$ will be parallel before and after contact, and have matching $\hat{\mathbf{u}}$ vectors.

$$\begin{pmatrix} u_x \\ u_y \\ 0 \end{pmatrix} = \frac{1}{|\vec{H}_{GP} \cdot (\hat{\boldsymbol{\imath}} + \hat{\boldsymbol{\jmath}})|} \begin{pmatrix} -\vec{H}_{GP} \cdot \hat{\boldsymbol{\jmath}} \\ \vec{H}_{GP} \cdot \hat{\boldsymbol{\imath}} \\ 0 \end{pmatrix} \tag{7.43}$$

If it is not possible to satisfy Eqns. 7.28 and 7.29 exactly, a measure of the error, ϵ, associated with a particular choice of u_x and u_y can be calculated by computing the normalized angular momentum component that is parallel to $\vec{g}$ and $\vec{r}$ (where $\vec{r}$ is the leg vector as in Fig. 7.6, and equivalent to $\vec{r}_{p/q}$ of the Euler pendulum).

$$\epsilon = 1 - \frac{\vec{H}_{p1}}{|\vec{H}_{p1}|} \cdot \begin{pmatrix} u_x \\ u_y \\ 0 \end{pmatrix} \tag{7.44}$$

As ϵ approaches zero the assumption that the plant rotates in a vertical plane after contact becomes better, making it possible to transition the biped into the 3^{rd} region of stability. Exactly how small ϵ needs to be for the 3DFPE to be accurate remains an open question. The answer will likely be system-dependent and highly influenced by the ratio of the length of the leg to the size of the foot.

We assume that steps taken along the line where the plane intersects the ground cause the pendulum to rotate in a vertical plane with a trajectory that leads the COM over the plant foot (satisfying Eqns. 7.28 and 7.29). All that remains is to choose the appropriate step length in order to stop the pendulum just as it becomes vertical. If the leg is well approximated as a rigid link that plastically impacts the ground, Wight et al.'s [108] FPE equation, shown below (with $s\phi$ and $c\phi$ representing $\sin\phi$ and $cos\phi$ for brevity), can be solved for ϕ (using a numerical method such as bisection) to yield the angle the swing limb should be held at just prior to contact.

$$0 = \frac{[mh(v_{1xy}^{||}\, c\phi + v_{1z}^{||}\, s\phi)c\phi + J_{com}\omega_1^{\perp}\, c^2\phi]^2}{mh^2 + J_{com}\, c^2\phi} + 2mgh\, c\phi(c\phi - 1)$$

Equation 7.45 uses the translational velocity components of the COM of the biped that are parallel ($\vec{v}_1^{||}$)

$$\vec{v}_{1xy}^{||} = (\vec{v}_1 \cdot \hat{\mathbf{u}}\ )\ \hat{\mathbf{u}} \tag{7.45}$$

$$\vec{v}_{1z}^{||} = (\vec{v}_1 \cdot \hat{\mathbf{k}}\ )\ \hat{\mathbf{k}} \tag{7.46}$$

$$\vec{v}_1^{||} = \vec{v}_{1xy}^{||} + \vec{v}_{1z}^{||} \tag{7.47}$$

and angular velocity components that are perpendicular ($\omega_1^{\perp}$) to the vertical projection plane.

$$\omega_1^{\perp} = \vec{\omega}_1 \cdot (\ \hat{\mathbf{u}} \ \times \ \hat{\mathbf{k}} \ ) \tag{7.48}$$

Trigonometry can be used to find $L_{FPE}(\phi)$, the location on the floor where the foot should be placed relative to the COM ground projection location.

$$L_{FPE}(\phi) = h \ \tan\phi \ \hat{\mathbf{u}} \tag{7.49}$$

If the leg is compliant, however, Wight et al.'s FPE [108] may not stop the biped in a single step. Leg compliance is particularly relevant for biomechanists, as human legs have been observed [37] and modeled [26] to behave like linear compression springs during walking and running. A foot placement method for a leg with a specific stiffness has been developed by Pratt et al. [82], who calculated the step length L_{CAP} (coined the capture point) required to balance Kajita et al.'s [47] linear inverted pendulum model (so named because its equation of motion are linear when the COM stays at a constant height h).

$$L_{CAP} = v_{1xy}^{\parallel} \sqrt{\frac{h}{g}} \ \hat{\mathbf{u}} \tag{7.50}$$

Pratt et al. showed that a linear inverted pendulum can be modeled as a point mass attached to the ground by a compliant leg with a spring of stiffness k_{CAP},

$$k_{CAP} = -\frac{mg}{h} \tag{7.51}$$

pre-loaded to a force of $f_{0,CAP} = (mg/h)\sqrt{L_{CAP}^2 + h^2}$. This is a non-standard compression spring in the sense that it exerts *less* force as it is compressed. A leg with this force-compression profile will exert a constant vertical force of mg on the body (and a varying horizontal force) as the COM of the biped rotates over the leg. If the biped has no vertical velocity at contact, and takes a step of length L_{CAP}, the biped will come to rest just as its body passes over its foot [82].

We conjecture that if both the CAP and the FPE can be covered with the landing foot, the biped can have any smoothly changing leg stiffness that is bounded from below by the

nonlinear spring associated with the CAP and from above by the FPE rigid leg assumption. Equivalently, the leg can have any smooth stiffness and damping characteristic provided the COM height does not decrease during step, the leg does not exceed its pre-contact length, and the foot can cover both the FPE and the CAP. This conjecture is important for biomechanists and roboticists alike: leg compliance influences balance, and both need to be controlled to prevent the biped from falling.

7.5 Experimental Methodology

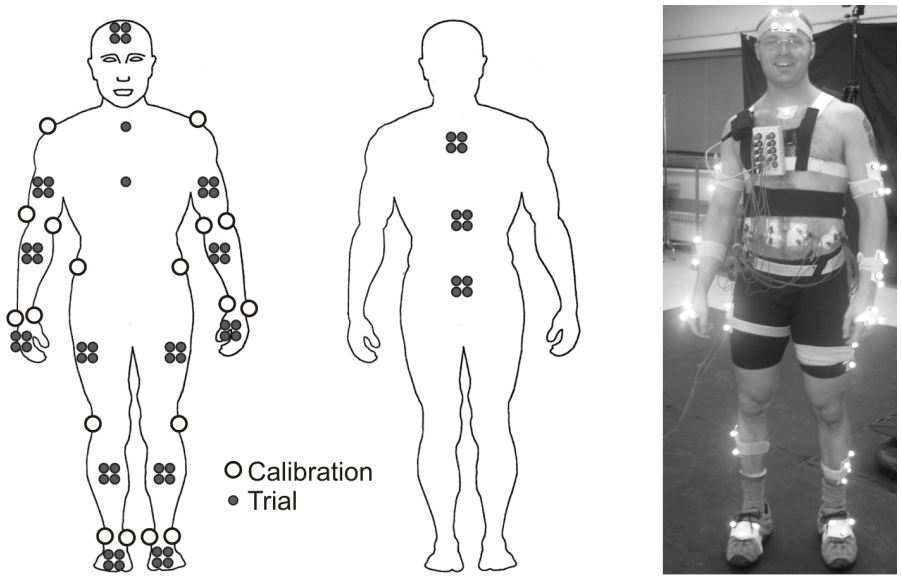

Figure 7.7: The panel on the left shows the calibration (markers on the joints) and rigid body marker sets (clusters of 4 markers). The panel on the right shows the author shortly after the data collection

A preliminary experimental validation of the 3DFPE was conducted to determine if the 3DFPE corresponded well with human foot placement and to see if the assumptions of the 3DFPE were reasonable during a range of activities (walking, gait termination and landing from a jump). Full body kinematics of one male subject of average height (1.75m) and mass (78kg), were tracked in 3D using Vicon marker arrays placed on the feet, shanks, legs, the torso, the head, the upper and lower arms, and hands. Inverse kinematics were used to make measurements of the position and orientation of each segment using Visual3D

[8]. Translational and angular segment velocities and accelerations were extracted from the position data after it was filtered using a dual-pass Butterworth filter with a 30 Hz cutoff frequency. The subject's movements were recorded (at 60 Hz) while they walked in a straight line, terminated gait, and performed a standing long jump. A force plate was also used to record (at 2400 Hz) the ground reaction forces during a single step of the walking experiment, and the final steps of the gait termination and jumping trials.

The state of an equivalent single body (see App. C.2 for details) was calculated at every time step using de Leva's anthropometric tables [14] and Eqns. C.32-C.36. The state vector of the single body representation was projected onto a plane that passed through the COM and was perpendicular to $\vec{H}_{COMGP}$ (as in Eqn. 7.43), the angular momentum vector of the body about the COM ground projection location. Equation 7.44 was used at contact onset to calculate ϵ, the amount of normalized momentum lost by projecting the state of the 3D biped onto a vertical plane.

Balance-restoring foot placement locations were calculated using the FPE (Eqn. 7.49) and CAP (Eqn. 7.50) algorithms, with steps taken along the intersection of the projection plane and the ground. At contact onset the distance between the subject's heel ($\vec{r}_{Heel}$) was compared to the 3DFPE ($\vec{L}_{FPE}(\phi)$) and CAP ($\vec{L}_{CAP}$) point locations ($D_{FPE,H}$, $D_{CAP,H}$).

$$D_{FPE,H} = |L_{FPE}(\phi) - \vec{r}_{Heel}| \tag{7.52}$$

$$D_{CAP,H} = |L_{CAP} - \vec{r}_{Heel}| \tag{7.53}$$

The time of foot contact was estimated to occur at the time of maximum heel acceleration using Hreljac et al.'s heel-strike and toe-off detection algorithm [41]. The time reported by Hreljac et al.'s algorithm was validated for the steps that fell on the force plate used in the study.

Since leg compliance affects foot placement location, apparent leg stiffness was estimated in order to interpret the subject's foot placement. The leg was assumed to behave like a linear spring [26] (with no preload) between the center-of-pressure ($\vec{r}_{COP}$) and the COM ($\vec{r}_{COM}$). The direction of the leg force ($\vec{r}_s$) was defined to take place between the COP (measured using a force plate) and the COM, with force components not in this direction ignored.

$$\vec{r}_s = \vec{r}_{COM} - \vec{r}_{COP} \tag{7.54}$$

The unloaded length of the leg spring (L_0) was estimated to be its maximum length during ground contact. The stiffness of the leg is given by the magnitude of the ground reaction force vector through the COM divided by the change in leg length.

$$k = \frac{\vec{F}_{GRF} \cdot \frac{\vec{r}_s}{|\vec{r}_s|}}{L_0 - |\vec{r}_s|} \tag{7.55}$$

The average and standard deviation of k beginning at single leg stance and ending at mid-stance — when the 3DFPE and CAP models come to rest — was calculated. Leg stiffness estimates were computed only for the steps that fell on the force plate used in the study.

The FPE and CAP algorithms make assumptions that are not met during human movement, degrading the accuracy of each algorithm. The error caused by violations of the assumptions of the FPE was estimated by multiplying observed changes in leg length (ΔL), moment of inertia about the COM (ΔJ_{COM}), system energy ($\Delta(T+V)$), and angular momentum magnitude about the contact point ($\Delta(\vec{H}_p \cdot (\hat{\boldsymbol{\imath}} + \hat{\boldsymbol{\jmath}}))$) by the corresponding numerically calculated partial derivative of the location of the FPE at the time of contact ($\frac{\partial L_{FPE}(\phi)}{\partial L}$, $\frac{\partial L_{FPE}(\phi)}{\partial J_{COM}}$, $\frac{\partial L_{FPE}(\phi)}{\partial (T+V)}$, $\frac{\partial L_{FPE}(\phi)}{\partial \vec{H}p}$) as in Millard et al. [66].

$$A_L = \frac{\partial L_{FPE}(\phi)}{\partial L}\Delta L \tag{7.56}$$

$$A_{J_{COM}} = \frac{\partial L_{FPE}(\phi)}{\partial J_{COM}}\Delta J_{COM} \tag{7.57}$$

$$A_{T+V} = \frac{\partial L_{FPE}(\phi)}{\partial (T+V)}\Delta (T+V) \tag{7.58}$$

$$A_{Hp} = \frac{\partial L_{FPE}(\phi)}{\partial (\vec{H}_p \cdot (\hat{\boldsymbol{\imath}} + \hat{\boldsymbol{\jmath}}))}\Delta (\vec{H}_p \cdot (\hat{\boldsymbol{\imath}} + \hat{\boldsymbol{\jmath}})) \tag{7.59}$$

The mean squared error of the assumptions of the FPE are reported for brevity.

$$A_{MSE} = \sqrt{A_L^2 + A_{J_{COM}}^2 A_{T+V}^2 A_{H_p}^2} \tag{7.60}$$

The CAP algorithm assumes that orbital energy E_{ORB} is a conserved quantity [82].

$$E_{ORB} = \frac{1}{2}\vec{v}_{1xy} \cdot \vec{v}_{1xy} - \frac{g}{2(\vec{r}_s \cdot \hat{\boldsymbol{\jmath}})}(\vec{r}_s \cdot \hat{\boldsymbol{\imath}})^2 \tag{7.61}$$

The percent change in orbital energy A_{ORB} from heel strike ($t1$) to mid-step ($t2$) was used to measure how well the assumptions of the CAP were being met.

$$A_{ORB} = \frac{E_{ORB,t2} - E_{ORB,t1}}{E_{ORB,t1}} \tag{7.62}$$

7.6 Experimental Results

The 3DFPE and CAP corresponded very well with human foot placement (HFP) choices (Fig. 7.8). The assumptions of the 3DFPE would have only affected the predicted location by 1-3 cm (column A_{MSE} in Tbl. 7.1) for each of the tasks. The assumption of the CAP that the biped conserves orbital energy was generally poor, though its predicted location corresponded well to the HFP location for every task except jumping. The assumption that the state vector of the subject could be well approximated by a 2D vertical projection was very accurate: the largest recorded value for ϵ — the percentage of the system's angular momentum vector not in the chosen vertical plane — was just a fraction of a percent.

The legs behaved like linear compression springs best during walking tasks, and exhibited nonlinearities during the gait termination and jumping tasks. The compliance of the legs depended on the task: the legs were stiffest during gait termination and most compliant when landing from a jump. The estimated leg stiffness was always bounded from above by a rigid leg and from below by the nonlinear spring of an equivalent linear inverted pendulum (k_{CAP} ranged from $-797N/m$ during walking to $-956N/m$ during the jump trial, calculated using Eqn. 7.51). Thus, it appears reasonable to assume that the true balance point for the subject is bounded by the 3DFPE and CAP locations. Although little experimental work has been done to measure leg stiffness during walking, the stiffness values found during the straight walking trials were close to one of the values reported in a simulation study by Geyer et al. [26]. The combined stiffness of *both* legs when landing from a jump was very close to the value reported for a single stance leg during running

[37]. Leg stiffness during gait termination has not been previously studied, and the values observed in this study were far higher than both continuous walking and jumping.

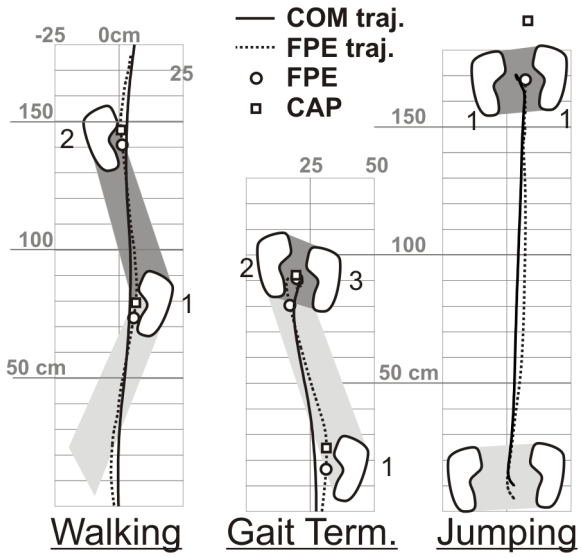

Figure 7.8: The subject's foot falls, COM and 3DFPE trajectories and the 3DFPE and CAP locations (at the time of contact) are shown for the walking, gait termination and jumping tasks. The position of each foot print was recorded by the Vicon marker cluster, while the size of the subject's foot print was measured after the trials with a ruler. The convex hull between the feet during double stance is shown in grey.

During the continuous walking trial, the HFP was close to both the 3DFPE and CAP locations (left pane of Fig. 7.8). Even though the subject did not step on the CAP nor 3DFPE locations, both of these points were within the convex hull formed by the striking heel and the rear foot during double stance. Thus, if the subject had wanted to stop, both the linear and rigid pendulum models predict that stopping would have been possible without taking an extra step. The subject placed their foot just to the outside of the 3DFPE and CAP points, presumably to maintain a characteristic sway in the medio-lateral plane. An increase in the subject's angular momentum about their foot during push-off caused the largest 3DFPE error — accounting for approximately 90% of the A_{MSE} — consistent with Millard et al.'s planar FPE results [66]. Orbital energy, a conserved quantity of the linear inverted pendulum, fluctuated by 32-40% of its value at heel strike during the stance phase.

Table 7.1: Data for each step of the subject's walking, gait termination, and jumping trials. The leg stiffness value (k) is reported after each step that landed on the force plate

Step	ϵ	$D_{FPE,H}$	A_{MSE}	$D_{CAP,H}$	A_{ORB}
Walk	%	cm	cm	cm	%
1	2.61e-3	7.15	2.12	12.7	40.8
2	1.13e-3	8.45	1.88	13.7	32.3
	k		19.6 ± 0.3 kN/m		
Stop	%	cm	cm	cm	%
1	1.35e-5	12.3	1.96	18.3	19.7
2	6.42e-3	5.81	0.99	5.30	-39.5
	k		43.9 ± 9.4 kN/m		
3	4.12e-2	16.4	2.41	17.4	-150
Jump	%	cm	cm	cm	%
1	1.91e-3	20.0	7.47	37.3	-102
	k		10.1 ± 3.2 kN/m		

During the gait termination trial, both the 3DFPE and the CAP points were enclosed by the contact area formed by the two feet (middle pane of Fig. 7.8) during steps 1-2 and 2-3. Both the linear and rigid pendulum models predict that the subject could have stopped without taking an extra step — which is what happened. The subject's leg stiffens during step 2, presumably as it straightens. Similar to the previous trials, the assumption that angular momentum is conserved during the contact is the worst of the five assumptions of the 3DFPE. Orbital energy increasingly varied as the subject slowed down. The assumption that the subject's state vector could be projected onto a vertical plane was the worst for step 3 of this trial. In the seconds after the 3^{rd} step, when the subject was standing quietly, the vertical angular momentum component (taken about the COM ground projection location) accounted for 4.2% of the subject's angular momentum. The increase of out-of-plane angular momentum suggests that the assumption of planar dynamics is worst during quiet standing, and best when the body is translating.

During the jumping trial the subject landed directly on the location predicted by the 3DFPE, and was nearly 10 cm short of the CAP (right pane of Fig. 7.8). It was expected the subject would land closer to the CAP location because the legs are at least twice as compliant during this task than any other, having a combined stiffness of only 10.1 ±

3.2 kN/m. The foot is physically large enough to cover both the 3DFPE and CAP locations, yet the subject favored the 3DFPE location. Nearly all of the assumptions of the 3DFPE were broken appreciably during this task, in contrast to the other trials. Examining the error values, it appears that many of them could cancel out if summed: A_L was 4.69 cm, $A_{J_{COM}}$ was -0.61 cm, A_{T+V} was -2.15 cm, and A_{H_P} was -5.36 cm which together sums to an error of -3.43 cm, half the value of A_{MSE}. The proximity of the subject's feet to the 3DFPE and the canceling of errors suggests that the subject compensated their foot placement location to accommodate for the anticipated loss of angular momentum, system energy and leg length caused by the landing.

7.7 Discussion

The 3DFPE and CAP together form a powerful tool to find a foot placement line that could restore balance to a human with compliant legs. The data suggest that the stiffness of human legs is bounded by a rigid leg and the nonlinear spring of the linear inverted pendulum and that the assumptions of the 3DFPE are reasonable for analyzing human motion. These models, however, have not been formulated to take into account momentum inputs and the compliance range that is characteristic of human legs. Also, despite having very compliant legs when landing from a jump, the subject favored the location predicted by the rigid pendulum model. It is possible that the subject was anticipating and accounting for future momentum inputs and assumption violations that neither the 3DFPE nor CAP locations currently account for. It is also possible that the observed differences were due to error in the anthropometric model. Both models require an accurate calculation of the COM location, which depends on body kinematics and an anthropometry model. As noted in Millard et al. [66], a plausible 10% error [50] in estimating the mass of the trunk would change the predicted location of the 3DFPE by 2-3cm forwards or backwards in the projection plane. The CAP is also affected by anthropometry errors because it requires the height of the COM. For the subject analyzed, a 1 cm error in the estimate of the COM height would result in an error of nearly 1 cm in the CAP location in any of the trials. Anthropometry likely affected the results, but it is unlikely that anthropometry errors were responsible for the large differences between the HFP, CAP and 3DFPE locations observed during the jumping task. The authors suggest that humans coordinate the placement of their feet, the stiffness of their legs, and anticipated future momentum inputs to change

the position and velocity of their body in a desirable manner.

7.8 Conclusions

An understanding of the mechanics of balance is highly important for its potential diagnostic and rehabilitation applications in humans, and in the design of advanced bipedal robots. Foot placement is a critical component of balance that humans exploit during locomotion. The work presented in this paper is unique because we have formally shown that an Euler pendulum, a simplified model of a biped, has regions of stability far outside its base of support, but only if its state vector can be projected onto a vertical plane without loss of information. Although this restriction seems severe, experimental data of human walking, stopping, and jumping suggests that this assumption is reasonable.

Foot placement is affected by not only a desired future state but also in response to the stiffness of the stance limb. Two planar methods, Wight et al.'s FPE [108] based on a rigid pendulum, and Pratt et al.'s CAP point [82] based on a compliant pendulum, were extended to provide 3D estimates by projecting the state vector of the human subject onto a vertical plane passing through the COM and perpendicular to the angular momentum vector of the body (taken about the COM ground projection). The human experiments showed that these two locations were often very close to each other, giving the subject the freedom to choose a leg stiffness bounded by the two models if they could cover both points with their plant foot. The jump trial illustrated that the predictions of each of the models sometimes differ substantially. These differences may be due to the human taking into account assumption violations that foot placement models currently ignore. These differences may also be due to inaccurate anthropometric data. The accuracy of the 3DFPE and CAP models are limited to a few centimeters until anthropometry can be estimated more accurately as indicated in column A_{MSE} in Tbl. 7.1, and in Millard et al. [66].

Chapter 8

Conclusions

It is ironic that the mechanics and control of the first steps Neil Armstrong took on the moon — or during any day of his life on earth — are more poorly understood than the means to actually travel to the moon. The intent of this thesis was to bridge some of the physical, and philosophical differences between how humans walk, and how we simulate walking. The present time, however, finds us still with many basic problems that prevent both the modeling and control of humanoid bipedal gait from matching human performance faithfully. Peasgood et al.'s gait model was one of the first attempts at developing a predictive human gait simulation using a controls-based approach. The poor ground reaction force profiles and fragile sense of balance of Peasgood et al.'s formulation are endemic in current forward dynamic simulations.

The work presented in this thesis is an attempt to address these two problems. Since the ground reaction force profile is intimately linked to the foot model, an improved foot contact model was formulated and developed. Since the stance limb controller simultaneously affects both the ground reaction force profiles, and the balance of the model, some effort was spent investigating candidate algorithms for how humans might control the torques in their legs during stance. A partitioned approach was used to control the stance limb of a series of models of increasing likeness to the human form. A simple SLIP model was used to compute a target torso COM trajectory, while an input-output feedback linearization controller was used to allow the anthropomorphic model to track the desired trajectory. While this approach appears to be a good one, it will not overcome the limitations of the SLIP model. In particular, the SLIP can walk only at a fixed pace and cannot stop. The

relationship between foot placement and balance was studied in order to give the simple model (of the partitioned approach) more control over its movements. Kinesiologists have long recognized that foot placement location is very important to restoring human balance. This topic has received little theoretical attention, and so a theoretical and experimental treatment of the subject was presented. Each of these topics has been investigated using simplified models that assume the state of the model can be measured perfectly, that nerves have no transmission delays, and that torque sources do an adequate job of representing muscles. In real life, the human sensory system is noisy, nerves have significant transmission delays and the musculature of the body is far more complicated than a torque source. Clearly there is still much work to be done.

8.1 Contributions

There are four major contributions in this thesis, and each relate to either improving the modelling or balance control of human gait simulation. The first major contribution is related to the development and preliminary experimental validation of a novel two segment foot model as presented in Ch. 4. This model differs from several in the literature because it includes flexibility at the midfoot. The validation method was novel because it was completed in the context of walking and took into consideration the compression of the heel and metatarsal foot pads.

The second contribution of this thesis is the partitioned approach to simulating human gait, and the torso-centric stance control systems presented in Ch. 5. Whereas the vast majority of bipedal control systems in the robotics and kinesiology literature focus on controlling the periodic motions of the legs during walking, the proposed control systems use the legs to control the state of the torso. Using this new formulation, the periodic movements of the legs are merely a side effect of having legs of finite length. This approach has the benefit of ensuring the stability of the trajectory of the torso, and imparting the human-like gaits of simpler models onto more useful anthropomorphic models. In addition, this formulation should simplify the task of searching for gaits as kinematic torso profiles of human gait are far simpler in form than any of the joint angle profiles of the leg.

The third and final contributions of this thesis are the experimental validation of Wight et al.'s planar foot placement algorithm, and the extension of this algorithm to the spatial

domain. Humans adeptly vary their foot placement location when walking, and particularly when stopping. Humans prevent falls and restore balance by using well-executed compensatory steps. Prior to the work presented in Chs. 6 and 7 there was no theoretically grounded foot placement algorithm that had been experimentally validated. As the experimental data in Chs. 6 and 7 shows, the assumptions of the FPE models are compatible with human legged locomotion, and the predicted foot placement location corresponds well with human foot placement, even when the assumptions of the model are violated. These foot placement algorithms are useful because they can improve the capabilities of the simple model — used in the partitioned approach to simulating human gait — by giving it the capability to stop in a human-like manner. These foot placement algorithms are also important because they also suggest candidate metrics to quantify how off-balance a subject is, and importantly, a means to quantify their balance performance. These metrics may be of clinical use for diagnosing balance problems in the future.

8.2 Future Work

While a few aspects of foot contact modeling and human balance have been investigated, there is still much to do. Improved methods need to be developed to validate foot contact models *in vivo*. The spatial foot placement algorithm need further experimental validation with a greater number of subjects. Although the FPE algorithms can compute a good location to place the swing leg, these algorithms do not offer any hints about how to execute such a move in a human-like way. Control of the swing phase deserves further investigation. Finally, while the control formulation presented in Ch. 5 was successfully applied to the multibody model during single stance, the performance of this controller could be improved. Finally, it will eventually be necessary to improve the control system formulation to take into account the imprecise nature of human sensory data, the transmission delays associated with nerves, and the neuromuscular dynamics. These general problems are important areas for future work related to this thesis. The following sections present these problems and some possible research approaches to solving them.

8.2.1 Volumetric Foot Contact Model

Validating a foot contact model convincingly has proven to be more difficult than formulating a foot contact model. In this thesis, the foot contact model was validated by driving the simulated foot through an experimentally collected kinematic path, and then judging the quality of the model based on how well the foot pad compressions matched those reported in the literature, and how well the simulated ground reaction force profiles matched the experimental profiles. By design, this validation method is sensitive to any errors present in the experimentally collected kinematic foot paths. Unfortunately the skin on the foot can move up to 1 cm relative to the bones. This amount of error is unacceptable for the purposes of validation because it is nearly equal to the amount of compression that the heel and metatarsal pads [10] undergo during stance.

The validation process used in this thesis can be improved by making better measurements of the kinematics of the foot bones, and foot pad strains during stance. Videofluoroscopy [100] offers the exciting capability of being able to make cinematic recordings of the bones of the foot *in vivo* during stance. By employing two or more such cameras, it should be possible to make 3D measurements of the kinematics of the foot bones during stance. Other means of measuring foot kinematics are desirable since videofluoroscopy cameras are quite expensive, somewhat scarce, and expose the subject to radiation. One alternative would be to track features of the foot that are invariant to skin movement. The shape of the bony areas of the foot (medial and lateral malleolus, top of the metatarsals), and thus the shadows cast on those areas, should not change as the skin of the foot moves over them during stance. It may be possible to track the kinematics of the bony parts of the foot by tracking the shadows cast by a known lighting source across those parts of the foot that have invariant geometry. Although tracking the kinematics of the foot bones is somewhat difficult, measuring foot pad strains *in vivo* is not as difficult. An ultrasound scanner which is embedded into a force plate [10] can provide some of the kinematic and kinetic data required to validate the contact model. It may also be possible to use the recorded ultrasound images to measure foot pad shear, a quantity that has not yet been recorded. Since most ultrasound scanners would not be large enough to scan the entire foot, but rather a small area, it is not likely that this approach would be able to yield the kinematics of all of the foot pads simultaneously.

Alternate validation methodologies should also be pursued because of the difficulty of

accurately measuring the kinematics of the foot bones during stance. One alternative method is to compare the experimental and simulated roll-over-shape (ROS) of the foot [35]. The ROS is the shape traced out by the COP during stance as measured in a reference frame attached to the leg. Using a ROS approach, the foot model would be attached to a model of the leg. The modelled leg would be driven through the same kinematic path as the experimentally measured leg. The quality of the foot model would then be assessed by comparing the ROS of the simulated foot to the experimental foot. In addition, if the data are clean enough, it may also be possible to compare the simulated and experimental ground reaction forces and foot pad compressions. This method may be a better form of validation than the previously described method because the computed angles of the shank will be less sensitive to skin artifact — because markers between the knee and ankle are physically farther apart than markers at the ankle and calcaneus — than the computed angles of the foot. The main draw back of using ROS as a means of validation is that the ankle torque now needs to be included in the simulation. The ankle torque could be estimated using inverse dynamics from the experiment, or the simulated ankle could have a spring-damper included in the model [22].

8.2.2 Stance Phase Control

The multibody gait simulation presented in Ch. 5 can be improved by updating the control system to require less feedback gain, by indexing of both the stance and swing kinematics, and by smoothly integrating these two phases together. The stance limb controller presented in Ch. 5 requires relatively high feedback gain to function. There is no experimental data to suggest that these gains ($10\frac{N}{mm}$ and of linear position error, and $175\frac{Nm}{^\circ}$ of orientation error) are unreasonable for stance legs; however experimental and simulation work done on the motor control of the upper limb [6] suggests that humans have to use low gain feedback control to prevent controller instability from arising due to the transmission delays associated with the nervous system. Improving the control system to function with lower feedback gain is desirable for future models, even if they are not including neural transmission delays. Lower gain feedback will likely be possible if the current control model of the foot is improved. Presently the foot is approximated as a rigid link that begins at the ankle and terminates with a revolute joint attached to a horizontal prismatic joint located at the COP of the foot (Fig. 5.8). Updating the foot abstraction to a ROS representation

[35] as in [96] would be a good start.

The torso and swing limb target kinematics of the multibody gait models presented in Ch. 5 are functions of time. The stability of the model, and the tractability of it to analysis can be improved if the target kinematics of the model are functions of a time-invariant quantity such as body lean angle [105]. Referencing the stance and swing limb kinematics with respect to body lean angle is common in the simulation of bipedal robots [105] and has recently been applied to a simplified human gait model [96]. Improvements can be made to the existing lean-angle referenced formulations to make them more human-like. Whereas humans take larger steps when perturbed, models being controlled using lean angle referenced trajectories do not. Instead, many steps will be taken until the orbit of the gait of the model converges to its reference orbit. A more human-like control formulation might instead reference the swing limb with respect to the lean angle and velocity, allowing the model to take one large step to catch its balance when the model perturbed, rather than many shorter steps.

Incorporating a body-angle and velocity-referenced leg kinematics in a multibody gait model similar to the one in Ch. 5 will not be easy. To date, these control methods have been applied to models and robots that have rigid feet, with model switching being used to avoid simulating contact [96], and particularly to avoid defining lean angle during double stance. Thus, difficulties will likely be encountered when applying the aforementioned control techniques to a model with continuous foot contact that has a double stance phase. In addition, care will have to be taken when switching between stance limb, and swing limb kinematic references to avoid the high control torques that were observed in the model presented in Ch. 5. These notions are just the beginnings of a human-like feedback control law that may allow a model to guide its swing limb as adeptly as a human.

The capabilities of the simple models (which are used as guides for anthropomorphic models in the partitioned gait simulation approach) also need to improve in order to simulate movements other than steady state walking. The SLIP was used as the simple model in Ch. 5, but it is limited because it can walk in a human-like way only at a fixed velocity. This restriction suggests that the likeness of the SLIP gait to human walking is perhaps a coincidence. Srinivasan [95] recently presented a low-dimensional model that had an energy-optimal gait that was very similar to both human and SLIP walking. The force actuators used for this model were not linear springs (as are used in the SLIP), but rather developed force such that both the first and second derivatives had finite limits (similar

to a 2^{nd} order low pass filter). The resemblance of these force actuators to a crude muscle model [110] is likely not a coincidence. Srinivasan's simple model suggests that the bandwidth limitations of human muscle are the dominating phenomenon that give human gait its characteristic COM and GRF profiles [109]. Planar and spatial simple models that incorporate bandwidth limited telescoping leg actuators, and movable contact points [7] should be developed and experimentally validated for transient movements such as gait initiation, gait termination, and compensatory stepping.

Although a feedback control approach could be used to make a model walk in a human-like manner, adapting such a control system to a new model (such as one with a prosthesis), or a new movement, will likely prove difficult. An approach that easily accommodates different models (ranging from dinosaurs to people) and motions (walking, stone stepping and jumping in 3D) has been developed by a group of computer animation researchers [67] for a bipedal human model with flat feet. Mordatch et al. used the partitioned approach mentioned in Ch. 5 (developed in parallel to the work in this thesis) but they use optimization to give their simple model greater capabilities than the SLIP, and their anthropomorphic model the ability to move smoothly. They are able to achieve a wide range of life-like 3D motions using a low-dimensional model (an approximate linear version of the SLIP) to plan all of the COM and COP profiles for 2 physical steps in the future at every integration time step. Torques are applied to the multibody model so that it tracks the path the low dimensional path planner has computed. A specialized optimization routine is used in both the low dimensional path planner and in the control of the multibody model [36], giving the system the flexibility to be used on different models and motions. Although it is not clear that it will be possible to expand this idea to a high fidelity human model — particularly one with muscles — the capabilities of the system to generate life-like animations of many motions make it worthy of further exploration.

8.2.3 Balance Corrections using Foot Placement

The FPE theory may prove to be a powerful tool in improving simple gait models and analyzing human balance because it is valid for both small and large perturbations and is not accompanied by restrictive assumptions. The FPE can be used to improve gait simulations by computing the target foot placement location rather than using optimization to solve for this parameter. This may be an important step to reducing the computational

demands of solving for energy optimal walking trajectories, which are high, even for the simple models that Srinivasan proposes [95]. The most important practical applications of the FPE research lie in improving balance assessment and rehabilitation. Metrics for bipedal instability and balance performance based on the 3DFPE theory may allow a patient's balance to be assessed accurately, allowing both the patient and the health care professional to take preventative action before the patient becomes prone to falling. The distance between the foot contact area of the biped and the 3DFPE is a good candidate for a measure of bipedal instability. Normalizing this distance with respect to leg length should produce a dimensionless measure of bipedal instability. Alternately, the angle between a vector passing through the COM and the FPE and the vertical could be used to quantify bipedal instability.

Experimental and theoretical work needs to be completed to realize the aforementioned diagnostic and rehabilitation applications of the 3DFPE. Compensatory stepping experiments with 3D perturbations need to be completed to compare the instability measures of the 3DFPE to existing measures. Perturbation experiments using different population groups will need to be completed to determine if these new measures would be useful diagnostic tools. The details of how best to formulate instability and balance performance metrics using the FPE requires experimental validation and potentially further theoretical development. Another key application of this research is in balance rehabilitation. The 3DFPE point could be projected on the floor to act as a target for the swing limb. The foot placement target, shown to a person while they are walking, could be used as a rehabilitation aid to help people guide their swing foot to an appropriate location.

References

[1] M Ackermann and W Schiehlen. Dynamic analysis of human gait disorder and metabolic cost estimation. *Archive of Applied Mechanics*, 75:569–594, 2006.

[2] M Ackermann and AJ van den Bogert. Optimality priciples for model-based prediction of human gait. *Journal of Biomechanics*, 43:1055–1060, April 2010.

[3] P Aerts, RF Kerr, D de Clercq, DW Ilsley, and R.McN. Alexander. The mechanical properties of the human heel pad: a paradox resolved. *Journal of Biomechanics*, 28:1299–1308, 1995.

[4] F Anderson and M Pandy. Static and dynamic optimization solutions for gait are practically equivalent. *Journal of Biomechanics*, 34:153–161, 1999.

[5] F Anderson and M Pandy. Dynamic optimization of human walking. *Journal of Biomechanical Engineering*, 123:381–390, 2001.

[6] N Bhushan and R Shadmehr. Computational nature of human adaptive control during learning of reaching movements in force fields. *Biological Cybernetics*, 81:39–60, 1999.

[7] SR Bullimore and JF Burn. Consequences of forward translation of the point of force application for the mechanics of running. *Journal of Theoretical Biology*, 238:211–219, 2006.

[8] C-Motion.Inc. Visual3d online documentation. http://www.c-motion.com/help/.

[9] MC Carson, ME Harrington, N Thompson, JJ O'Connor, and TN Theologis. Kinematic analysis of a multi-segment foot model for research and clinical applications: a repeatability analysis. *Journal of Biomechanics*, 34:1299–1307, 2001.

[10] P Cavanagh. Plantar soft tissue thickness during ground contact in walking. *Journal of Biomechanics*, 32:623–628, 1999.

[11] AW Crook. A study of some impacts between metal bodies by a piezo-electric method. *Proceedings of the Royal Society of London, Series A*, 212:377–390, 1952.

[12] R Crowinshield and RA Brand. A physiologically based criterion of muscle force prediction in locomotion. *Journal of Biomechanics*, 14(11):793–801, 1981.

[13] MA Cyr and C Smeesters. Instructions limiting the number of steps do not affect the kinetics of the threshold of balance recovery in younger adults. *Journal of Biomechanics*, 40:2857–2864, 2007.

[14] P de Leva. Adjustments to zatsiorsky-seluyanov's segment inertia parameters. *Journal of Biomechanics*, 29:1223–1230, 1996.

[15] JB Dingwell and HG Kang. Differences between local and orbital dynamic stability during human walking. *ASME Journal of Biomechanical Engineering*, 129:586–593, August 2007.

[16] J Donelan, R Kram, and A Kuo. Simultaneous positive and negative external mechanical work in human walking. *Journal of Biomechanics*, 35:117–124, 2002.

[17] D.Wang. Damping breaks an assumption of input-output feedback linearization, 2010. Personal communication.

[18] H Edgell. Ultrasound scan of mmillard's unloaded foot pads, 2007. Personal communication.

[19] JJ Eng, DA Winter, and AE Patla. Strategies for recovery from a trip in early and late swing during human walking. *Experimental Brain Research*, 102:339–349, 1994.

[20] H Essen. Average angular velocity. *European Journal of Physics*, 14:440–445, 1993.

[21] D P Ferris, M Louie, and C T Farley. Running in the real world: adjusting leg stiffness for different surfaces. *The Royal Society B*, 265:989–994, 1998.

[22] T Fukunaga, K Kubo, Y Kawakami, S Fukashiro, H Kanehisa, and CN Maganaris. In vivo behaviour of human muscle tendon during walking. *Proceedings of the Royal Society B*, 268:229–233, 2001.

[23] A Gefen, M Megido-Ravid, and Y Itzchak. In vivo biomechanical behavior of the human heel pad during the stance phase of gait. *Journal of Biomechanics*, 34:1661–1665, 2001.

[24] KGM Gerritsen, AV Bogert, and BM Nigg. Direct dynamics simulation of the impact phase in heel-toe running. *Journal of Biomechanics*, 28:661–668, 1995.

[25] H Geyer and H Herr. A muscle reflex model that encodes principles of legged mechanics produces human walking dynamics and muscle activities. *IEEE Transactions on Neural Systems and Rehabilitation Engineering*, 18:263–273, 2010.

[26] H Geyer, A Seyfarth, and R Blickhan. Compliant leg behaviour explains basic dynamics of walking and running. *Proeedings of The Royal Society B*, 276:2861–2867, 2006.

[27] L Gilchrist and D Winter. A two-part viscoelastic foot model for use in gait simulations. *Journal of Biomechanics*, 29(6):795–798, 1996.

[28] L Gilchrist and D Winter. A multisegment computer simulation of normal human gait. *IEEE Transactions on Rehabilitation Engineering*, 5(4):290–299, 1997.

[29] W Goldsmith. *Impact: The Theory and Physical Behavior of Contacting Solids*. Edward Arnold, London, U.K., 1960.

[30] Y Gonthier. *Contact Dynamics Modelling for Robotic Task Simulation*. PhD thesis, The University of Waterloo, August 2007.

[31] Y Gonthier, J McPhee, C Lange, and JC Piedboeuf. A contact modeling method based on volumetric properties. In *Proceedings of the 5th International Conference on Multibody Systems, Nonlinear Dynamics and Control*, pages 477–486, September 2005.

[32] J Grizzle, G Abba, and F Plestan. Asymptotically stable walking for biped robots: Analysis via systems with impulse effects. *IEEE Transactions on Automatic Control*, 46(1):51–64, 2001.

[33] JP Halloran, M Ackermann, A Erdemir, and AJ van den Bogert. Concurrent musculoskeletal dynamics and finite element analysis predicts altered gait patterns to reduce foot tissue loading. *Journal of Biomechanics*, 43:2810–2815, October 2010.

[34] AJ Hamel, NA Sharkey, FL Buczek, and J Michelson. Relative motions of the tibia, talus, and calcaneus during the stance phase of gait: a cadaver study. *Gait and Posture*, 20:147–153, 2004.

[35] AH Hansen, DS Childress, and EH Knox. Roll-over shapes of human locomotor systems: Effects of walking speed. *Journal of Clinical Biomehcanics*, 19:407–414, 2004.

[36] N Hansen. The cma evolution strategy: A comparing review. In Jose Lozano, Pedro Larrañaga, Iñaki Inza, and Endika Bengoetxea, editors, *Towards a New Evolutionary Computation*, volume 192 of *Studies in Fuzziness and Soft Computing*, pages 75–102. Springer Berlin / Heidelberg, 2006.

[37] J He, R Kram, and T A McMahon. Mechanics of running under simulated low gravity. *Journal of Applied Physiology*, 71:863–870, 1991.

[38] H Herr and M Popovic. Angular momentum in human walking. *Journal of Experimental Biology*, 211:467–481, 2008.

[39] K. Hirai, M. Hirose, Y. Haikawa, and T. Takenaka. The development of honda humanoid robot. In *Robotics and Automation, 1998. Proceedings. 1998 IEEE International Conference on*, volume 2, pages 1321 –1326 vol.2, May 1998.

[40] N Hogan. The mechanics of multi-joint posture and movement control. *Biological Cybernetics*, 52:315–331, 1985.

[41] A Hreljac and R Marshall. Algorithms to determine event timing during normal walking using kinematic data. *Journal of Biomechanics*, 33:783–786, 2000.

[42] K Hunt and F Crossley. Coefficient of restitution interpreted as damping in vibroimpact. *Transactions of the ASME Journal of Applied Mechanics*, 42(E):440445, 1975.

[43] B Husemann, F Muller, C Krewer, S Heller, and E Koenig. Effects of locomotion training with assistance of a robot-driven gait orthosis in hemiparetic patients after stroke. *Stroke*, 38(2), 2007.

[44] A Isidori. *Nonlinear Control Systems Systems*. Springer, New Jersey, 3 edition, 1995.

[45] S Jezernik, G Colombo, T Keller, H Frueh, and M Morari. Robotic orthosis lokomat: A rehabilitation and research tool. *International Neuromodulation Society*, 6(2):108–115, 2003.

[46] J Juang. Fuzzy neural network approaches for robotic gait synthesis. *IEEE Transactions on Systems, Man and Cybernetics, Part B*, 30(4):594–601, 2000.

[47] S Kajita, F Kanehiro, K Kaneko, K Yok, and H Hirukawa. The 3d linear inverted pendulum mode: A simple modeling for a biped walking pattern generation. In *Proceedings of the 2001 IEEE/RSJ*, pages 239–246, 2001.

[48] T Karčnik. Using motion analysis data for foot-floor contact detection. *Medical & Biological Engineering & Computing*, 41:509–512, 2003.

[49] HK Khallil. *Nonlinear Systems*. Prentice Hall, New Jersey, 3 edition, 2001.

[50] I Kingma, HM Toussaint, MP De Looze, and JH Van Dieen. Segment inertial parameter evaluation in two anthropomorphic models by application of a dynamic linked segment model. *Journal of Biomechanics*, 29:693–704, 1996.

[51] H Kinoshita, PR Francis, T Murase, S Kawai, and T Ogawa. The mechanical properties of the heel pad in elderly adults. *European Journal of Applied Physiology*, 73:404–409, 1996.

[52] E Kubica, D Wang, and D Winter. Feedforward and deterministic fuzzy control of balance and posture during human gait. In *Proceedings of the 2001 IEEE International Conference on Robotics and Automation*, pages 372–380, May 2001. Seoul, Korea.

[53] A Kuo. Stabilization of lateral motion in passive dynamic walking. *International Journal of Robotics Research*, 9, September 1999.

[54] A Kuo. A simple model of bipedal walking predicts the preferred speed-step length relationship. *Journal of Biomechanical Engineering*, 123, June 2001.

[55] A Kuo. Energetics of actively powered locomotion using the simplest walking model. *Journal of Biomechanical Engineering*, 124:113–120, 2002.

[56] DN Lee, JR Lishman, and JA Thomson. Regulation of gait in long jumping. *J Exp Phychol Hum Percept Perform*, 8:448–459, 1982.

[57] R Lewis and V Torczon. Pattern search algorithms for bound constrained minimization. *SIAM Journal on Optimization*, 9:264–269, 1999.

[58] PS Lum, CG Burgar, PC Shor, M Majmundar, and M van der Loos. Robot-assisted movement training compared with conventional therapy techniques for the rehabilitation of upper limb motor function following stroke. *Arch. Phys. Med. Rehabil.*, 83:952–959, 2002.

[59] AJ MacDonald and KT MacDonald. The rolling motion of a disk on a horizontal plane. *Physics*, 2001. id:0008227v3.

[60] MapleSoft. Maplesim online documentation. http://www.maplesoft.com.

[61] MathWorks. Matlab online documentation. http://www.mathworks.com.

[62] T McGeer. Passive dynamic walking. *International Journal of Robotics Research*, 9(2):62–82, 1990.

[63] T McGeer. Dynamics and control of bipedal locomotion. *Journal of Theoretical Biology*, 163:277–314, 1993.

[64] M Millard, E Kubica, and J McPhee. Mapping spring forces onto anthropomorphic legs. In *Proceedings of the* 1^{st} *Joint International Conference on Multibody System Dynamics*, May 2010. Lappeenranta, Finland.

[65] M Millard, J McPhee, and E Kubica. Multi-step forward dynamic gait simulation. In CL Bottasso, editor, *Multibody Dynamics: Computational Methods and Applications*, pages 25–43. Springer, 2009.

[66] M Millard, D Wight, J McPhee, E Kubica, and D Wang. Human foot placement and balance in the sagittal plane. *Journal of Biomechanical Engineering*, 131(12), 2009.

[67] I Mordatch, M de Lasa, and A Hertzmann. Robust Physics-Based Locomotion Using Low-Dimensional Planning. *ACM Transactions on Graphics*, 29(3), 2010.

[68] MSC.Adams. Adams online documentation. http://www.mscsoftware.com.

[69] FA Mussa-Ivaldi, N Hogan, and E Bizzi. Neural, mechanical, and geometric factors subserving arm posture in humans. *The Journal of Neuroscience*, 10:2732–2743, Oct 1985.

[70] EJ Muybridge. *Muybridge's Human Figure in Motion*. Dover Publications Inc, 2007.

[71] AE Patla. Strategies for dynamic stability during adaptive human locomotion. *IEEE Engineering in Medicine and Biology Magazine*, pages 48–52, March/April 2003.

[72] AE Patla, SD Prentice, S Reitdyk, F Allard, and C Martin. What guides the selection of alternate foot placement during locomotion in humans. *Experimental Brain Research*, 128:441–450, 1999.

[73] AE Patla and JN Vickers. How far ahead do we look when required to step on specific locations in the travel path during locomotion. *Experimental Brain Research*, 148:133–138, 2003.

[74] AE Patla, N Wijneberg, and SWD Hill. Control of com by cop explains the response reversal observed during medio-lateral perturbations applied during human locomotion. *Gait and Posture*, 9, 1999.

[75] M Peasgood. Energetics of prosthetic gait. Master's thesis, University of Waterloo, 2002.

[76] M Peasgood, E Kubica, and J McPhee. Stabilization and energy optimization of a dynamic walking gait simulation. *ASME Journal of Computational and Nonlinear Dynamics*, 2:65–72, January 2007.

[77] M Peshkin, DA Brown, JJ Santos-Munne, A Makhlin, E Lewis, JE Colgate, J Patton, and D Schwandt. Kineassist: A robotic overground gait and balance training device. In *Proceedings of the 2005 IEEE* 9^{th} *International Conference on Rehabilitation Robotics*, pages 241–246, June 2005.

[78] I Poulakakis. *Stabilizing Monopedal Robot Running: Reduction-by-Feedback and Compliant Hybrid Zero Dynamics*. PhD thesis, The University of Michigan, December 2009.

[79] I Poulakakis and JW Grizzle. Formal embedding of the spring loaded interved pendulum in an asymmetric hopper. In *Proc. of the European Control Conference*, pages 1–8, September 2007. Kos, Greece.

[80] I Poulakakis and JW Grizzle. Monopedal running control: Slip embedding and virtual constraint controllers. In *Proc. of the IEEE/RSJ International Conference of Intelligent Robots and Systems*, pages 323–330, October 2007. San Diego, California.

[81] J Pratt. *Exploiting Inherent Robustness and Natural Dynamics in the Control of Bipedal Walking Robots*. PhD thesis, Massachusetts Institute of Technology, June 2000.

[82] J Pratt, J Carff, S Drakunov, and A Goswami. Capture point: A step toward humanoid push recovery. In *Proceedings of the IEEE-RAS International Conference on Humanoid Robots*, December 2006. Genoa, Italy.

[83] J Pratt and G Pratt. Exploiting natural dynamics in the control of a 3d bipedal walking simulation. In *International Conference on Climbing and Walking Robots (CLAWAR99)*, September 1999. Portsmouth, UK.

[84] JE Pratt and GA Pratt. Exploiting natural dynamics in the control of a 3d bipedal walking simulation. In *International Conference on Climbing and Walking Robots*, September 1999. Portsmouth,UK.

[85] MH Raibert. *Legged Robots That Balance*. The MIT Press, Cambridge, Massachusetts, first edition, 1986.

[86] AV Rao, DA Benson, C Darby, MA Patterson, C Francolin, I Sanders, and GT Huntington. Algorithm 902: GPOPS, a matlab software for solving multiple-phase optimal control problems using the gauss pseudospectral method. *ACM Trans. Math. Softw.*, 37(2):1–39, 2010.

[87] MS Redfern and T Schumann. A model of foot placement during gait. *J Biomech*, 27:1339–1346, 1994.

[88] DJ Reinkensmeyer, D Aoyagi, JL Emken, JA Galvez, W Ichinose, G Kerdanyan, S Maneekobkunwong, K Minakata, JA Nessler, R Weber, RR Roy, R de Leon,

JE Bobrow, SJ Harkema, and VR Edgerton. Tools for understanding and optimizing robotic gait training. *Journal of Rehabilitation Research and Development*, 43:657–670, 2006.

[89] DJ Reinkensmeyer, JL Emken, and SC Cramer. Robotics, motor learning, and neurologic recovery. *Annual Review of Biomedical Engineering*, 6:497–525, 2004.

[90] RH Riffenburgh. *Statistics in Medicine*. Elsevier, Burlington, Massachusetts, second edition, 2006.

[91] T Ryschon, M Fowler, R Wysong, A Anthony, and S Balaban. Efficiency of human skeletal muscle in vivo: comparison of isometric, concentric, and eccentric muscle action. *Journal of Applied Physiology*, 83:867–874, 1997.

[92] J Schmitt and J Clark. Modeling posture-dependent leg actuation in sagittal plane locomotion. *Bioinspiration and Biomimetics*, 4(4):1–17, 2009.

[93] S Scott and DA Winter. Biomechanical model of the human foot: kinematics and kinetics during the stance phase of walking. *Journal of Biomechanics*, 26:1091–1104, 1998.

[94] MW Spong and M Vidyasagar. *Robot Dynamics and Control*. John Wiley and Sons, 1989.

[95] M Srinivasan. Fifteen observations on the structure of energy-minimizing gaits in many simple biped models. *Journal of The Royal Society Interface*, 2010.

[96] S Srinivasan, IA Raptis, and ER Westervelt. Low-dimensional sagittal plane model of normal human walking. *ASME Journal of Biomechanical Engineering*, 130:051017–1 — 051017–11, October 2008.

[97] G Taga. A model of the neuro-musculo-skeletal system for human locomotion. *Biological Cybernetics*, 73:97–111, 1995.

[98] G Taga, Y Yamaguchi, and H Shimizu. Self-organized control of bipedal locomotion by neural oscillators in unpredictable environment. *Biological Cybernetics*, 65:147–159, 1991.

[99] D Thelen and F Anderson. Using computed muscle control to generate forward dynamic simulations of human walking from experimental data. *Journal of Biomechanics*, 39:1107–1115, 2006.

[100] T.Jenkins. Videofluoroscopy of the human foot during walking, 2008. Personal communication.

[101] MA Townsend and A Seireg. The synthesis of bipedal locomotion. *Journal of Biomechanics*, 5:71–83, 1972.

[102] BR Umberger, KGM Gerritsen, and PE Martin. A model of human muscle energy expenditure. *Computer Methods in Biomechanics & Biomedical Engineering*, 6:99–111, 2003.

[103] G Valiant. *A determination of the mechancial characteristics of the human heel pad in vivo*. PhD thesis, The Pennsylvania State University, 1984.

[104] M Vukobratovic and B Barovac. Zero-moment point - thirty five years of its life. *International Journal of Humanoid Robotics*, 1(1):157–173, 2004.

[105] ER Westervelt, JW Grizzle, C Chevallereau, JH Choi, and B Morris. *Feedback Control of Dynamic Bipedal Robot Locomotion*. CRC Press, 2007.

[106] KP Westlake and C Patten. Pilot study of lokomat versus manual-assisted treadmill training for locomotor recovery post-stroke. *Journal of Neuro Engineering and Rehabilitation*, 6, 2009.

[107] SN Whittlesey, REA Van Emmerik, and J Hamill. The swing phase of human walking is not a passive movement. *Motor Control*, 4:273–292, 2000.

[108] D Wight, E Kubica, and D Wang. Introduction of the foot placement estimator: A dynamic measure of balance for bipedal robotics. *J. Comput. Nonlinear Dynam.*, 3:11009, 2008.

[109] D Winter. *Biomechanics and Motor Control of Human Gait: Normal, Elderly and Pathological*. University of Waterloo Press, 2^{nd} edition, 1991.

[110] D Winter. *Biomechanics and Motor Control of Human Movement*. John Wiley and Sons, Hoboken, NJ, 3^{rd} edition, 2005.

[111] M Wisse, DGE Hobbelen, and AL Schwab. Adding an upper body to passive dynamic walking robots by means of a bisecting hip mechanism. *IEEE Transactions on Robotics*, 23:112–123, 2007.

[112] M Wojtyra. Multibody simulation model of human walking. *Mechanics Based Design of Structures and Machines*, 31(3):357–377, 2003.

[113] MY Zarrugh, FN Todd, and HJ Ralston. Optimization of energy expenditure during level walking. *European Journal of Applied Physiology*, 33:293–306, 1974.

Appendix A

Chapter 3 Model Parameters

The anthropometric parameters used in Ch.3 and in Peasgood et al.'s model are listed in Tbl. A.1. The anthropometric values from Peasgood et al.'s work originate from a gait model produced by LifeMod. These parameters are compared to the equivalent parameters calculated using the methods presented by Winter [110] in Tbl. A.1.

The relative difference between the two parameter sets was calculated by dividing the absolute difference by the average value of the two parameters in question. The comparison showed that the relative difference between the parameter lists was on the range of 10-20% which is acceptable given that the data sets came from different studies. However, the values for the moment of inertia of the HAT and the mass of the foot were grossly different. Peasgood et al.'s parameters were used in Ch.3 for the purposes of model validation, while more conventional values [110] were used for the final simulations.

Gross LifeMod Model Parameters				
	Mass (M) in kg	Length (L) in m		
Body (B)	64.740	1.696		
HAT (H)	37.810	0.347*	*HL: vertical distance between	
Thigh (T)	7.876	0.440	the greater trochanter and the	
Shin (S)	3.537	0.376	glenohumeral joint.	
Foot (F)	2.052	0.220		
LifeMod vs. conventional anthropometric data				
	LifeMod values	**Relative Difference** (%)	**Conventional values**	**Conventional formula [110]**
Hat				
mH	37.810	14.9	43.893	0.678 BM
Jzz_H	2.190	**64.5**	1.122	HM (HL 0.496)^2
dHr	0.279	19.7	0.229	0.66 HL
Right Thigh				
mTr	7.876	19.5	6.474	0.100 BM
Jzz_Tr	0.149	6.8	0.159	TM (TL 0.323)^2
pTr	0.205	7.3	0.191	0.433 TL
dTr	0.235	6.0	0.250	0.567 TL
Right Shin				
mSr	3.537	16.1	3.010	0.0465 BM
Jzz_Sr	0.040	14.0	0.046	SM (SL 0.302)^2
pSr	0.166	2.1	0.163	0.433 SL
dSr	0.210	1.7	0.213	0.567 SL
Right Foot				
mFr	2.052	**74.5**	0.939	0.0145 BM
Jzz_Fr	0.010	4.4	0.01	FM (FL 0.690)^2
†pFr	0.1	4.9	0.110	0.5 FL
†dFr	0.1	4.7	0.110	0.5 FL
†Not actually a model parameter, just included for comparison				

Table A.1: A comparison between LifeMod's model parameters and conventional anthropometric data. The geometry of the foot is not present because there is no conventional anthropometric data on feet of which the author is aware.

All of the parameters associated with foot contact model used in Ch.3 are listed in Tbl. A.2. The foot is modeled using a Hunt-Crossley contact model of Eqn. 3.1 and a Coulomb friction model of Eqn. 3.2. The coefficient of damping, and the coefficient of friction are interpolated using cubic splines (Fig. 3.2). The contact parameters listed below are identical to the ones used in Peasgood et al.'s work [75].

Foot Contact Parameters			
Name	Units	Value	Description
k_L	N/m	800000	Linear foot tissue stiffness factor
p		2.2	Exponential stiffness factor
y_1	m	0.01	Distance of maximum dampening
c_{max}	$\frac{Ns}{m}$	1000	Damping factor
μ_S		0.8	Coefficient of static friction
μ_d		0.2	Coefficient of dynamic friction
v_s	$\frac{m}{s}$	0.05	Stiction velocity
v_d	$\frac{m}{s}$	2	Dynamic friction velocity

Table A.2: Contact and friction model parameters.

All of the control parameters used in the model are shown in Tbl. A.3.1. The joint controller coefficients were taken directly from Peasgood's thesis [75]. The pitch controller and velocity controller coefficients had to be found for the nominal gait. These coefficients were found using a brute force grid search that tested every combination of pitch controller coefficient within a given grid size. The best performing pair was chosen, and then the grid size was reduced by a factor of two. This process was continued until the grid size was $\frac{1}{1024}^{th}$ of its initial size. Note that no velocity controller values actually reduced the velocity error of the model for the nominal gait until simulation times were extended beyond 20 seconds.

Joint Controller Coefficients from [75]			
Joint stiffness ($\frac{Nm}{rad}$)		Joint dampening ($\frac{Ns}{m}$)	
K_{ankle}	1996	Kd_{ankle}	27.5
K_{hip}	2625	Kd_{hip}	19.4
K_{knee}	1984	Kd_{knee}	12.5
Optimal Balance Controller Coefficients for the Nominal Gait			
Pitch Controller		Velocity Controller	
Ki ($\frac{s}{rad}$)	3.0012	0.16389	
Kp ($\frac{1}{rad}$)	0.1592	0.87827	

Table A.3: Control parameters for the joint controllers, the balance controller and the velocity controller. Note that no velocity controller was found to improve the velocity error of the new implementation of the 2D gait model until the simulation time was extended beyond 20 seconds

Appendix B

Chapter 4 Model Parameters

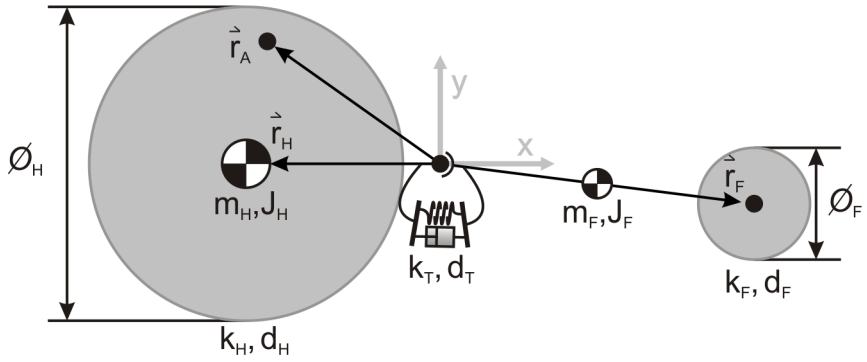

Figure B.1: The geometry, contact and inertial foot model parameters

All of the parameters associated with foot contact model used in Ch. 4 are listed in Tbl. B.1. The foot pads are modeled using Gonthier et al.'s volumetric contact model [31] with spherical contact elements. Coulomb friction of Eqn. 3.2 is used to model tangential forces with the coefficient of friction being interpolated using cubic splines (Fig. 3.2). The geometry of the foot, foot pad contact properties, and the stiffness and damping of the revolute joint at the metatarsal were all found using optimization as described in Ch. 4. The the geometry of the foot is reported with the tarsal joint relaxed. The mass and inertia

properties of the entire foot were found using conventional anthropomorphic tables [110], and equally split between the hind and forefoot segments.

Foot Contact Parameters			
Name	Units	Value	Description
m_H	0.500	kg	Mass of the hind foot
J_H	5.50×10^{-3}	$kg\ m^2$	Inertia of the hind foot
$\vec{r}_A$	(-5.08, 3.59)	(cm, cm)	Ankle location w.r.t. tarsal joint
$\vec{r}_H$	(-5.74,0)	(cm, cm)	Heel location w.r.t. tarsal joint
$\emptyset_H$	9.18	cm	Heel contact sphere diameter
k_H	3.72×10^7	N/m^3	Heel contact sphere stiffness
d_H	0.0648		Heel contact sphere dimensionless damping
m_F	0.500	kg	Mass of the forefoot located at the center of $\vec{r}_F$
J_F	5.50×10^{-3}	$kg\ m^2$	Inertia of the forefoot
$\vec{r}_F$	(9.28,-1.18)	(cm, cm)	Distal metatarsal head location w.r.t. tarsal joint
$\emptyset_F$	3.30	cm	Forefoot contact sphere diameter
k_F	4.06×10^8	N/m^3	Forefoot contact sphere stiffness
d_F	4.12×10^{-3}		Forefoot contact sphere dimensionless damping
k_T	343	Nm/rad	Tarsal joint stiffness
d_T	1.03	$Nm\ s/rad$	Tarsal joint damping
μ_d	0.5		Coefficient of dynamic friction
μ_s	0.6		Coefficient of static friction
v_d	0.01	m/s	Dynamic friction velocity
v_s	0.005	m/s	Static friction velocity

Table B.1: Two-segment, volumetric foot model parameters

Appendix C

Euler Pendulum Equations of Motion

The equations of motion for rolling without slipping for the Euler pendulum (Fig. 7.3 and 7.4) are found by taking moments about the contact point to eliminate reaction forces. First equations for the linear and angular acceleration of the COM are kinematically derived, then substituted into into the dynamic equation for angular acceleration. The dynamic equations for the COM linear acceleration are used to eliminate the unknown contact force $\vec{F}$.

To begin, the total angular velocity of the pendulum is composed of two components: that of a moving reference frame ($\vec{\omega}_{123}$), and that of the pendulum relative to the reference frame ($\dot{\beta}$):

$$\vec{\omega} = \vec{\omega}_{123} + \omega_{rel}\ \hat{\mathbf{1}} \tag{C.1}$$

As shown in Fig. 7.4 the frame $\hat{\mathbf{1}}\ \ \hat{\mathbf{2}}\ \ \hat{\mathbf{3}}$ rotates at $\dot{\theta}\ \hat{\mathbf{z}}\ + \dot{\alpha}\ \hat{\mathbf{2}}$:

$$\vec{\omega}_{123} = \dot{\theta}\ \hat{\mathbf{z}}\ + \dot{\alpha}\ \hat{\mathbf{2}}\ = -\dot{\theta}\cos\alpha\ \hat{\mathbf{1}}\ + \dot{\alpha}\ \hat{\mathbf{2}}\ - \dot{\theta}\sin\alpha\ \hat{\mathbf{3}} \tag{C.2}$$

Noting that

$$\hat{\mathbf{z}}\ = -\cos\alpha\ \hat{\mathbf{1}}\ - \sin\alpha\ \hat{\mathbf{3}} \tag{C.3}$$

The time derivatives of the local axes are:

$$\frac{d\ \hat{\mathbf{1}}}{dt} = \vec{\omega}_{123} \times\ \hat{\mathbf{1}} = -\dot{\theta}\sin\alpha\ \hat{\mathbf{2}}\ -\dot{\alpha}\ \hat{\mathbf{3}} \tag{C.4}$$

$$\frac{d\ \hat{\mathbf{2}}}{dt} = \vec{\omega}_{123} \times\ \hat{\mathbf{2}} = \dot{\theta}\sin\alpha\ \hat{\mathbf{1}}\ -\dot{\theta}\cos\alpha\ \hat{\mathbf{3}}\ = -\dot{\theta}\ \hat{\mathbf{r}} \tag{C.5}$$

$$\frac{d\ \hat{\mathbf{3}}}{dt} = \vec{\omega}_{123} \times\ \hat{\mathbf{3}} = \dot{\alpha}\ \hat{\mathbf{1}}\ +\dot{\theta}\cos\alpha\ \hat{\mathbf{2}} \tag{C.6}$$

Where the second horizontal unit vector $\hat{\mathbf{r}}$ (the first being $\hat{\mathbf{2}}$) is defined by:

$$\hat{\mathbf{r}}\ =\ \hat{\mathbf{2}}\ \times\ \hat{\mathbf{z}}\ = -\sin\alpha\ \hat{\mathbf{1}}\ +\cos\alpha\ \hat{\mathbf{3}} \tag{C.7}$$

Thus,

$$\frac{d\ \hat{\mathbf{r}}}{dt} = \dot{\theta}\ \hat{\mathbf{2}} \tag{C.8}$$

Combining Eqns. C.1 and C.2 total angular velocity is given by:

$$\vec{\omega} = \dot{\beta}\ \hat{\mathbf{1}}\ +\dot{\alpha}\ \hat{\mathbf{2}}\ -\dot{\theta}\sin\alpha\ \hat{\mathbf{3}} \tag{C.9}$$

where

$$\dot{\beta} = \omega_{rel} - \dot{\theta}\cos\alpha \tag{C.10}$$

The angular acceleration can be found by taking a time derivative of Eqn. C.9, substituting in Eqns. C.4, C.5, C.6, and collecting $\hat{\mathbf{1}}\ \ \hat{\mathbf{2}}\ \ \hat{\mathbf{3}}$ components:

$$\dot{\omega} = \left\{ \begin{array}{c} \ddot{\beta} \\ \ddot{\alpha} - \dot{\beta}\dot{\theta}\sin\alpha - \dot{\theta}^2\sin\alpha\cos\alpha \\ -\ddot{\theta}\sin\alpha - 2\dot{\alpha}\dot{\theta}\cos\alpha - \dot{\beta}\dot{\alpha} \end{array} \right\} \tag{C.11}$$

The velocity of the center of mass of the disk contact is calculated using the nonholonomic constraint that the disk rolls without slipping:

$$\vec{v}_p = \vec{v}_q + \vec{\omega} \times (a\ \hat{\mathbf{3}}\ + c\ \hat{\mathbf{1}}\ ) = 0 \tag{C.12}$$

The acceleration of the center of mass of the Euler pendulum can be found by taking the derivative of Eqn. C.12 and substituting in expressions for $\dot{\hat{\mathbf{1}}}$, $\dot{\hat{\mathbf{2}}}$ and $\dot{\hat{\mathbf{3}}}$ from Eqns. C.4, C.5 and C.6.

$$\frac{d^2\vec{r}_q}{dt^2} = \left\{ \begin{array}{c} -a\ddot{\alpha} + (a\dot{\beta} + c\dot{\theta}\sin\alpha)\dot{\theta}\sin\alpha + \dot{\alpha}^2 c \\ a\ddot{\beta} + c\ddot{\theta}\sin\alpha + 2c\dot{\theta}\dot{\alpha}\cos\alpha + a\dot{\alpha}\dot{\theta}\sin\alpha \\ \ddot{\alpha}c + a\dot{\alpha}^2 - (a\dot{\beta} + c\dot{\theta}\sin\alpha)(\dot{\theta}\cos\alpha) \end{array} \right\} \tag{C.13}$$

Expressions for the translational and angular acceleration of the COM (located at point q) of the Euler pendulum in the $\hat{\mathbf{1}}$ $\hat{\mathbf{2}}$ $\hat{\mathbf{3}}$ frame can be calculated by taking time derivatives of angular momentum ($\vec{L}_p$ about the contact point p) and combining it with Eqn. C.13.

$$\vec{L}_p = [J]\,\vec{\omega} \tag{C.14}$$

$$\frac{d\vec{L}_p}{dt} = [J]\,\dot{\vec{\omega}} + \vec{\omega}_{123} \times \vec{L}_p \tag{C.15}$$

The size of expression for $d\vec{L}_p/dt$ can be greatly reduced if $[J]$ is allowed to be symmetrical about the $\hat{\mathbf{1}}$ axis. For the purposes of this analysis it is assumed that the inertia matrix has an axis of symmetry about the $\hat{\mathbf{1}}$ axis (as Fig. 7.3 suggests).

The equations of motion can now be found by examining the dynamics of the Euler pendulum. The only forces and torques acting on the inverted pendulum are due to gravity $-mg\hat{z}$, contact forces $\vec{F}$, rolling resistance torque $\vec{\tau}_R$, and spin friction torque $\vec{\tau}_F$.

$$m\frac{d^2\vec{r}_q}{dt^2} = \vec{F} - mg\ \hat{\mathbf{z}} \tag{C.16}$$

The angular acceleration equations are also quite similar to an those of an Euler disk [59] with the addition of τ_R, a rolling resistance term, and τ_F, a spinning friction term:

$$\frac{d\vec{L}_p}{dt} = (c\ \hat{\mathbf{1}}\ + a\ \hat{\mathbf{3}}\ ) \times \vec{F} + \tau_R\ \hat{\omega}_{\ t} + \tau_F\ \hat{\omega}_{\ n} \tag{C.17}$$

The unknown contact force $\vec{F}$ can be eliminated using Eqn. C.16 and by taking moments about point p.

$$\begin{aligned} \frac{d\vec{L}_p}{dt} &= (c\ \hat{\mathbf{1}}\ + a\ \hat{\mathbf{3}}\ ) \times (m\frac{d^2\vec{r}_q}{dt^2} + mg\ \hat{\mathbf{z}}\ ) \\ &\quad +\tau_R\ \hat{\omega}_{\ t} + \tau_F\ \hat{\omega}_{\ n} \end{aligned} \tag{C.18}$$

The rolling resistance torque $\vec{\tau}_R$ is assumed to be of positive magnitude R in the direction opposite the tangential angular velocity vector $\hat{\boldsymbol{\omega}}_T$.

$$\vec{\tau}_R = -R\hat{\boldsymbol{\omega}}_T \tag{C.19}$$

$$\vec{\omega}_T = (\vec{\omega}_q \cdot\ \hat{\mathbf{r}}\ )\ \hat{\mathbf{r}}\ + (\vec{\omega}_q \cdot\ \hat{\mathbf{2}}\ )\ \hat{\mathbf{2}} \tag{C.20}$$

$$= \omega_{rel} \sin^2\alpha\ \hat{\mathbf{1}}\ + \dot{\alpha}\ \hat{\mathbf{2}}\ - \omega_{rel} \sin\alpha \cos\alpha\ \hat{\mathbf{3}} \tag{C.21}$$

$$\hat{\omega}_{\ T} = \frac{\vec{\omega}_T}{|\vec{\omega}_T| + \delta} \tag{C.22}$$

For the purposes of simulation, the rolling resistance torque is assumed to be proportional to the product of the normal force and the horizontal angular speed of the contact ring; (κ is a positive coefficient of rolling resistance).

$$\vec{\tau}_R = -\kappa\vec{F} \cdot\ \hat{\mathbf{z}}\ (\vec{\omega}_T \cdot \vec{\omega}_T)\ \hat{\omega}_{\ T} \tag{C.23}$$

$$\tag{C.24}$$

The spin friction torque, $\vec{\tau}_F$, is assumed to be of positive magnitude S in the direction opposite to the normal angular velocity vector $\hat{\boldsymbol{\omega}}_N$.

$$\vec{\tau}_F = -S\hat{\boldsymbol{\omega}}_N \tag{C.25}$$

For the purposes of simulation, the spin friction torque is assumed to be proportional to the product of the contact force and the rate the contact point is spinning normal to the surface; (μ_S is a positive coefficient of spinning friction).

$$\vec{\tau}_F = -\mu_S(\vec{F} \cdot \ \hat{\mathbf{z}}\ )(\vec{\omega} \cdot \ \hat{\mathbf{z}}\ )\ \hat{\mathbf{z}} \tag{C.26}$$

The equations of motion can be found by substituting Eqns. C.15, C.13, C.19, and C.25 into Eqn. C.18 and solving for $\ddot{\beta}$, $\ddot{\alpha}$, and $\ddot{\theta}$. Note that for Eqns. 7.1, 7.2, and 7.3 all of the terms associated with rolling resistance torques and spinning friction torques in Eqns. C.19, and C.25 are lumped into the $\mathcal{L}_\beta$, $\mathcal{L}_\alpha$ and $\mathcal{L}_\theta$ terms.

C.1 3DFPE Conditions

Equations 7.28 and 7.29 must be satisfied for a 3DFPE point, a single-step balance point, to exist. These constraints can only be satisfied in a few specific cases, which are described mathematically in the following text. Prior to contact, the angular momentum of the pendulum — with mass m, inertia $[J]$, the leg vector $\vec{r}_{p/q}$ and initial conditions $\vec{v}_1$ and $\vec{\omega}_1$ (the translational and angular velocity of the COM prior to contact)— is given by:

$$\vec{H}p_1 = [J]\vec{\omega}_1 + \vec{r}_{p/q} \times m\vec{v}_1 \tag{C.27}$$

After contact, angular momentum can be calculated by assuming that the pendulum is purely rotating about its contact point.

$$\vec{H}p_2 = [J]\vec{\omega}_2 + \vec{r}_{p/q} \times m(\vec{\omega}_2 \times \vec{r}_{p/q}) \tag{C.28}$$

If angular momentum is assumed to be conserved ($\vec{H}_{p1} = \vec{H}_{p2}$), the post-contact angular velocity of the pendulum can be expressed in terms of the pre-contact linear velocity, angular velocity and leg length. Equations 7.28 and 7.29 can be evaluated symbolically to determine if these conditions are satisfied. If the inertia matrix $[J]$ is diagonal, and all

entries are equal in magnitude (to keep the size of the expressions to a manageable size), Eqns. 7.28 and 7.29 become:

$$
\begin{aligned}
0 &= \vec{H}p_2 \cdot \vec{r}_{p/q} = \omega_{1x} r_x + \omega_{1y} r_y + \omega_{1z} r_z && \text{(C.29)} \\
0 &= \vec{H}p_2 \cdot \vec{g} && \text{(C.30)} \\
&= \frac{J_1 \omega_{1z} + m r_z \left(\omega_{1x} r_x + \omega_{1y} r_y + \omega_{1z} r_z\right)}{m(r_x^2 + r_y^2 + r_z^2) + J_1} \\
&\quad + \frac{m \left(v_{1,y} r_x - v_{1,x} r_y\right)}{m(r_x^2 + r_y^2 + r_z^2) + J_1} && \text{(C.31)}
\end{aligned}
$$

Where subscripts $x, y,$ z are used to denote the components of the vector quantities $\vec{r}_{p/q}$, $\vec{\omega}_1$ and $\vec{v}_1$. Equations C.29 and C.31 are satisfied if there is no angular momentum about the vertical axis prior to contact ($\vec{\omega}_1 \cdot \vec{r}_{p/q} = 0$); the pre-contact angular velocity vector is perpendicular to the leg vector ($\vec{\omega}_1 \cdot \vec{r}_{p/q} = 0$); and the horizontal components of the linear velocity and the leg vector are parallel.

C.2 Applying the 3DFPE to Multibody Systems

The utility of the 3DFPE lies in analyzing the balance of humans and as a part of the balance control system of a bipedal robot. Both of these applications involve articulated actuated mechanisms that are more complicated than an inverted pendulum, and do not necessarily meet the underlying assumptions of the 3DFPE. The 3DFPE can be applied at an instant in time to an equivalent inverted pendulum representation of these more complicated mechanisms. The mass of the equivalent inverted pendulum (m_e) is simply the sum of the segment masses (m_i),

$$
m = \sum_i^n m_i \qquad \text{(C.32)}
$$

while the center of mass location $\vec{r}_{cm}$ and average velocity $\vec{v}_{cm}$ are calculated using weighted sums.

$$\vec{r}_{cm} = \frac{1}{m}\sum_{i}^{n} m_i \vec{r}_i \tag{C.33}$$

$$\vec{v}_{cm} = \frac{1}{m}\sum_{i}^{n} m_i \vec{v}_i \tag{C.34}$$

The moment of inertia $[J]$ is calculated relative to the center of mass location using the parallel axis theorem.

$$[J] = \sum_{i}^{n} ([R_{0,i}][J_i] + m_i((\vec{r}_i - \vec{r}_{cm}) \cdot (\vec{r}_i - \vec{r}_{cm}))[I]) \tag{C.35}$$

Where $[R_{0,i}]$, $[J_i]$, and $\vec{r}_i$ is the rotation matrix, inertia matrix, and COM location of the i^{th} body respectively. The matrix $[I]$ is used to designate the identity matrix. Finally, the whole-body angular momentum about the COM, $[J]\vec{\omega}_{cm}$, can be calculated as

$$[J]\vec{\omega}_{cm} = \left(\sum_{i}^{n}[R_{0,i}][J_i]\vec{\omega}_i + (r_i - r_{cm}) \times m_i(\vec{v}_i - \vec{v}_{cm})\right) \tag{C.36}$$

The single body equivalent parameters and states can be projected onto a plane using Eqn. 7.43 prior to using the FPE or the CAP to calculate the location of a stabilizing step. The quality of the estimate of the FPE or the CAP is dictated by how closely the complicated mechanism meets the assumptions of either of the methods. The effect of assumption violations on foot placement location can be calculated using a numerical sensitivity analysis as in Millard et al. [66]. For walking movements the FPE is highly insensitive to changes in leg length, moment of inertia and system energy. The FPE is sensitive to changes in whole body angular momentum about the contact point ($\vec{H}p$).